OUTCROP TO SUBSURFACE RESERVOIR CHARACTERIZATION OF THE LOWER MESAVERDE GROUP, RED WASH FIELD, UINTA BASIN AND DOUGLAS CREEK ARCH, UTAH AND COLORADO

by

Chelsea A. Fenn

B.S., University of Florida, 2012

A thesis submitted to the

Faculty of the Graduate School of the

University of Colorado in partial fulfillment

Of the requirement for the degree of

Master of Science

Department of Geological Sciences

2014

This thesis entitled:

Outcrop to Subsurface Reservoir Characterization of the Lower Mesaverde Group, Red Wash Field, Uinta Basin and Douglas Creek Arch, Utah and Colorado

written by Chelsea A. Fenn

has been approved for the Department of Geological Sciences

_____

Matthew J. Pranter

_____

Edmund R. Gustason III

_____

Rex D. Cole

Date _____

The final copy of this thesis has been examined by the signatories, and we find that both the content and the form meet acceptable presentation standards of scholarly work in the above mentioned discipline.

ABSTRACT

Chelsea A. Fenn (M.S., Geology [Department of Geological Sciences])

Outcrop to Subsurface Reservoir Characterization of the Lower Mesaverde Group, Red Wash Field, Uinta Basin and Douglas Creek Arch, Utah and Colorado

Thesis directed by Professor Matthew J. Pranter

The Mesaverde Group (Late Cretaceous) at Red Wash Field within the Uinta Basin produces oil and natural gas from low-permeability, fluvial sandstone reservoirs that were deposited in a predominantly freshwater, low-energy setting with minor brackish-water influence. Four main architectural elements present in core and nearby outcrops include fluvial bars, crevasse splays, floodplain deposits, and coal. Depositional trends reflect an overall decrease in energy toward the northwest, where subsurface deposits are located on the periphery of the main channel belt, while contemporaneous outcrop deposits record more extensive brackish-water influence.

Static reservoir connectivity (total and constrained), assessed using 3-D reservoir models of the fluvial deposits at Red Wash Field, varies as a function of well density, sandstone-body geometry, and net-to-gross ratio (sandstone-body abundance). Results suggest that sandstone geometry produces a minor (6%) increase in total connectivity; however, the abundance of crevasse splays is a major contributor to total connectivity and should be considered as an important factor in reservoir development. Stratigraphic zones with < 40% net-to-gross ratio

exhibit greater total connectivity (up to 81.8%) with higher well density. Above 40% net-to-gross ratio, only a minor increase (10-15%) in connectivity resulted. For porous sandstones (porosity > 6%), connectivity is, on average, 26% lower than total sandstone connectivity and is more sensitive to well density and net-to-gross ratio.

DEDICATION

This thesis is dedicated to my parents, Amanda Wolfert and Robert Fenn. Thank you for teaching me the importance of hard work, independence, and gratitude. Your love and encouragement has helped me undertake the most difficult challenges and achieve more than I ever thought possible.

ACKNOWLEDGEMENTS

I would like to thank my advisor, Matt Pranter, and my committee members, Gus Gustason and Rex Cole, for their direction and encouragement during my research. I would like to acknowledge Gus Gustason for his enthusiasm and invaluable feedback, whether in the field or the core lab. I would also like to thank Mark Longman, Russell Griffin, and John Stills at QEP for their assistance in providing me the core access and data necessary to complete this research.

I would like to thank my fellow graduate students for their friendship: Connor Burt, John McFadden, Jason Fredericks, Wes Ball, and Stephen Heron. A huge thanks to my field assistants, Kevin Toeneboehn, Dan King, and Chris Beliveau for their hard work. I would like to specifically thank Bryan McDowell for his help in the field and sharing his enthusiasm, expansive knowledge, and sense of humor with me.

I owe a debt of gratitude for the support and companionship of Julian Michaels and Jon Lyon, who continually encouraged me through the most difficult times of this wild journey.

This research was funded by the AAPG Grants-in-Aid Program, the Society of Petrophysicists and Well Log Analysts (SPWLA), and the sponsors of the Williams Fork Consortium (Phase VI): Anadarko Petroleum Corporation, Chevron, ExxonMobil, iReservoir, Occidental Petroleum Corporation (OXY), Suncor Energy, QEP Resources, Inc., WPX Energy, Schlumberger, Jason, and IHS. Schlumberger provided Petrel® 3-D modeling software, IHS provided Petra® well-database software, and Jason provided PowerLog® well-log normalization software. I greatly appreciate all of the sponsor's support and input during this project.

CONTENTS

PAGE

ABSTRACT…….....iii

DEDICATION…….....v

ACKNOWLEDGEMENTS……vi

CONTENTS…….....vii

LIST OF TABLES……..ix

LIST OF FIGURES…….x

INTRODUCTION……...1

TECTONIC AND STRATIGRAPHIC SETTING……..8

LITHOFACIES ASSOCIATIONS AND ARCHITECTURAL ELEMENTS……..……13

THREE-DIMENSIONAL MODELS OF FLUVIAL DEPOSITS……25

Model Framework……..26

Training Images…….28

SNESIM Algorithm……...31

Fluvial Architectural-Element Models……..…34

STATIC CONNECTIVITY OF FLUVIAL DEPOSITS AT RED WASH FIELD……..39

“Reservoir-quality” Sandstone vs. Total Sandstone……..40

Static Sandstone Connectivity Analysis……42

CONCLUSIONS……...51

REFERENCES……..53

APPENDIX……59

APPENDIX……59

A. Core Descriptions and Lithofacies Photos……...…59

B. Outcrop Photos, Measured Section Descriptions, and Fieldwork Data……..…….89

C. MPS Training Images……112

D. Static Connectivity Tables and Supplemental Material…….122

E. Gamma-Ray Log Normalization: Well Groups……..…129

F. Stratigraphic Zonation……...…132

LIST OF TABLES

1. Lithofacies summary……..14

2. Model framework zone statistics……...29

3. MPS model inputs……..32

4. Model architectural-element proportions……...37

5. Zone static connectivity statistics……..…48

LIST OF FIGURES

1. Study area location……...2

2. Stratigraphic framework……..5

3. Location of wells and measured sections…….6

4. Paleogeographic setting……...9

5. Type log…….12

6. Core-to-log comparison (RW 12D4-25B, 10195’ – 10230’)…….16

7. Core-to-log comparison (RW 12D4-25B, 10230’ – 10265’)…….17

8. Cross-section of measured sections……...20

9. Model framework……...27

10. Channel- vs. crescent-shape fluvial bar preservation……..…30

11. MPS models……..…36

12. Architectural-element and net-to-gross ratio histograms……..…38

13. Well-spacing patterns and static connectivity……..….41

14. Static connectivity histograms…….44

15. Static connectivity graphs……45

16. Zone static connectivity and net-to-gross……47

17. Connectivity vs. net-to-gross ratio……...50

INTRODUCTION

The low-permeability fluvial sandstones of the Late Cretaceous Mesaverde Group form important oil and gas reservoirs within the Uinta Basin of northeastern Utah and primarily gas reservoirs in the Piceance basin of northwestern Colorado. The lower Mesaverde Group reservoirs examined in this study are made up of lenticular, discrete sandstones interbedded with carbonaceous mudstones and coals that were deposited in alluvial and coastal-plain settings. Current development strategies at Red Wash Field within the northeastern Uinta Basin (Figure 1) involve drilling vertical wells to target hydrocarbon-charged sandstone bodies within the lower Mesaverde Group. However, fluvial sandstone bodies are inherently heterogeneous at different scales, thus predicting their architecture, reservoir properties, and connectivity in the subsurface based solely on well-log suites can be challenging. Analysis of outcrop analogs provides data that cannot be obtained from subsurface data alone. Furthermore, combining sedimentological characteristics derived from outcrop analogs with subsurface data can be an integral step when constructing high-quality reservoir models with the goal of optimizing well placement and spacing efficiency to maximize hydrocarbon recovery.

Prior studies have documented basin-scale sedimentology and stratigraphy of the lower Mesaverde Group and equivalent strata of the Williams Fork Formation (Piceance Basin) (Tyler and Mcmurry, 1995; Hettinger and Kirschbaum, 2002; Kirschbaum and Hettinger, 2004; Foster, 2010; Leibovitz, 2010; Hlava, 2011). Each of these studies has relied on outcrop, core, well data, or a combination of these to reconstruct depositional histories in order to predict the occurrence of reservoir-quality sandstones within a sequence-stratigraphic framework. Other authors have investigated field-scale fluvial architecture of Mesaverde Group outcrops, which include detailed descriptions and classification of observed sandstone-body types, dimensional statistics (e.g.,

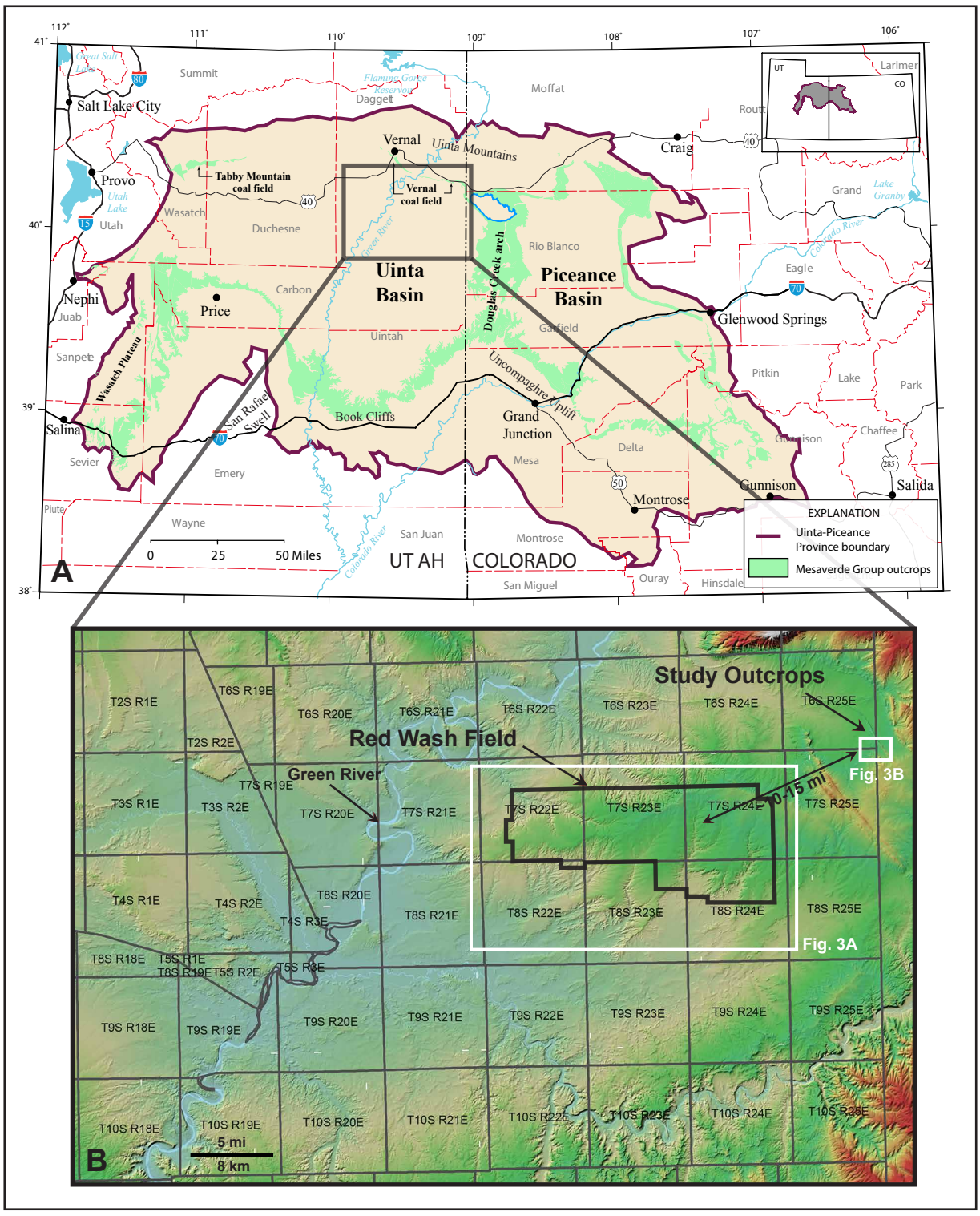

Figure 1. A: The study area is located in the northeastern Uinta Basin just west of Dinosaur, CO, and southeast of Vernal, UT. Modified from Johnson and Roberts (2003). B: Shaded relief map showing the study outcrops and location of Red Wash Field. The outcrops are approximately 10-15 miles from the nearest wells in Red Wash Field. Detailed maps of the white boxed areas can be found in Figure 3A and 3B. Shaded relief map was constructed in ArcGIS using a 10-meter DEM sourced from the USGS.

width, thickness, and width-to-thickness ratio), and paleocurrent-indicator data to gain further insight on subsurface reservoir heterogeneities and stacking patterns in the Uinta and Piceance basins (Ellison, 2004; Anderson, 2005; Cole and Cumella, 2005; German, 2006; Panjaitan, 2006; Pranter et al., 2007, 2009; Cole, 2008; White et al., 2008; Shaak, 2010; Harper, 2011). Because fluvial sandstone bodies of the Mesaverde Group are discontinuous and difficult to correlate in the subsurface even at high well densities (e.g., 10-ac, 660 ft [201 m] spacing), numerous studies have examined fluvial architecture in three dimensions at the outcrop scale to address static sandstone connectivity (Pranter et al., 2007, 2008, 2009, 2014; Sommer, 2007; Hewlett, 2010; Pranter and Sommer, 2011).

Static sandstone connectivity is defined in this study by Pranter and Sommer (2011) as "a percentage that is calculated as the volume of sandstone bodies connected to a particular pattern of wells (directly or indirectly) divided by the total sandstone volume". A series of studies conducted in the Piceance Basin by Sommer (2007), Pranter et al. (2009), and Pranter and Sommer (2011) applied different net-to-gross ratio and well-spacing scenarios to synthetic reservoir models generated using detailed statistics of fluvial sandstone-body characteristics (e.g., dimensions, orientations, shape, and stratigraphic distribution) from Coal Canyon, Colorado. Net-to-gross ratio is herein defined by the total sandstone volume divided by the total volume of the zone or interval. Their results were used to quantitatively evaluate the effect of these parameters (e.g., net-to-gross ratio, well spacing) on static sandstone connectivity.

While extensive research has been conducted on the Mesaverde Group (Williams Fork Formation) in the Piceance Basin, only a few studies have addressed the trends of equivalent strata in the Uinta Basin (Cole, 2008; Stancel et al., 2008; White et al., 2008). This study examines the fluvial architecture and static sandstone connectivity of the lower Mesaverde

Group in the Uinta Basin through integration of outcrop analysis, detailed core descriptions, and subsurface 3-D reservoir modeling. In order to determine primary controls on reservoir characteristics, static connectivity, and optimal well spacing for future production at Red Wash Field, the following research objectives are addressed: 1) identify key facies and facies associations present at outcrop locations and in the subsurface, 2) determine the diagnostic wireline-log response and petrophysical properties for fluvial architectural elements and the parameters needed to define these architectural elements in non-cored wells, 3) investigate the spatial variability of reservoir properties (e.g., lithology, architectural elements, porosity and permeability), and 4) examine how static connectivity varies with well spacing, net-to-gross ratio, and sandstone-body type.

The stratigraphic interval of interest is approximately 500 ft (152 m) thick and extends from the top of the Sego Sandstone to the top of the Neslen Formation (Figure 2). It crops out along the Douglas Creek Arch on the northeastern flank of the Uinta Basin about 10-15 miles (16-24 km) from Red Wash Field (Figure 1 and Figure 3B). Due to extensive erosion of the outcrop area, the ability to collect accurate sandstone-body dimensions and geometry directly was limited; therefore, subsurface 3-D modeling of fluvial deposits in Red Wash Field rely partially on data constraints from previous studies conducted along the Douglas Creek Arch and southwest Piceance Basin (Cole and Cumella, 2005; Panjaitan, 2006; Cole, 2008; Pranter et al., 2009; Hlava, 2011). The subsurface data set includes wireline logs for 70 wells in the Red Wash Field area that penetrate the lower Mesaverde Group, as well as two recently drilled cores totaling 773 ft (235 m) in length (Figure 3A). In contrast to Pranter and Sommer (2011), this study utilizes well logs and core data from an actual field during the initial stages of development to condition the 3-D reservoir models, and multiple well placement scenarios are subsequently

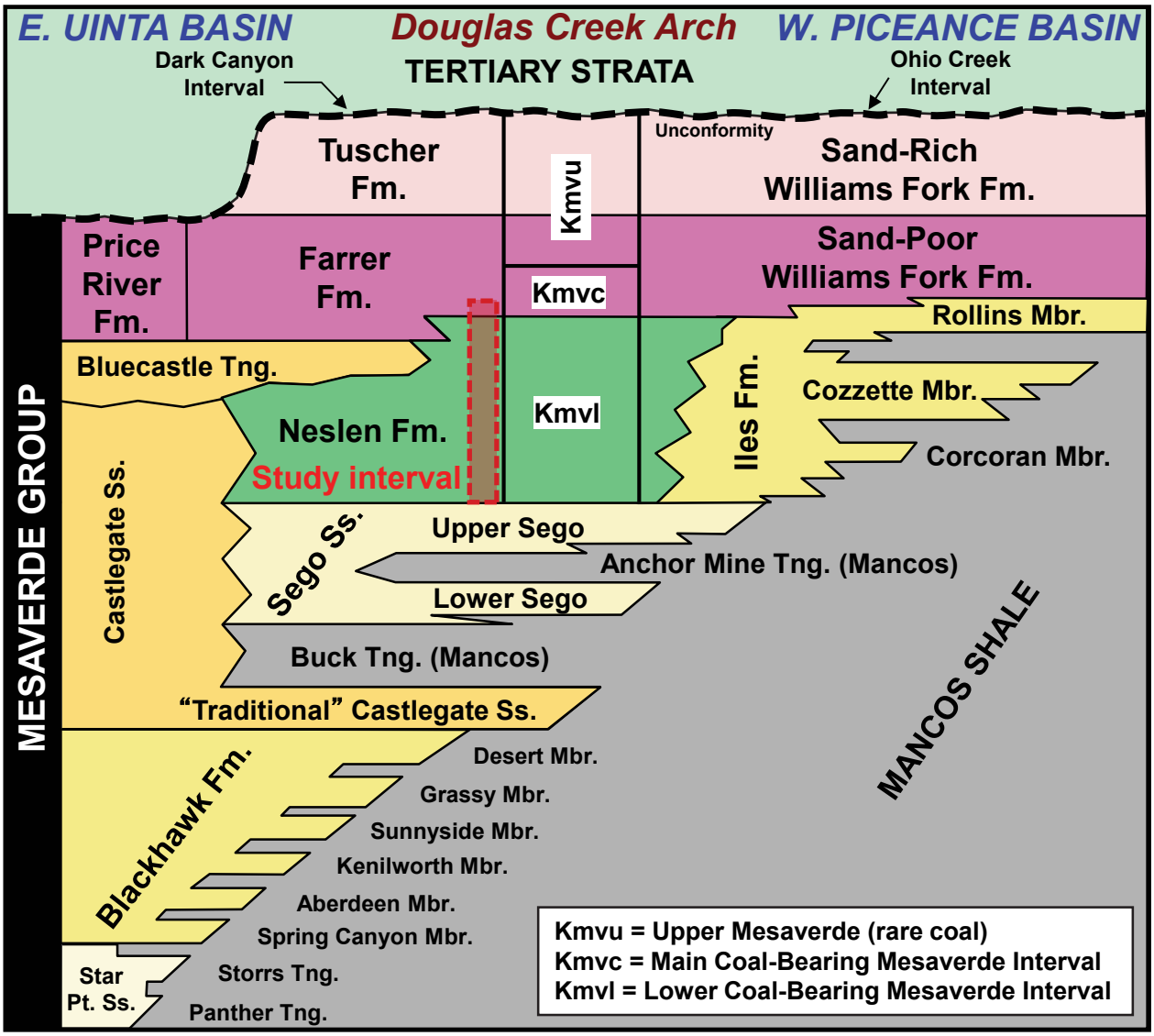

Figure 2. Generalized stratigraphic framework and terminology of the Mesaverde Group. The study interval is outline by the red box and extends from the top of the Sego Sandstone, up through the Neslen Formation, and includes the lowermost portion of the Farrer Formation. Modified from Hettinger and Kirschbaum (2003) and Cole (2010).

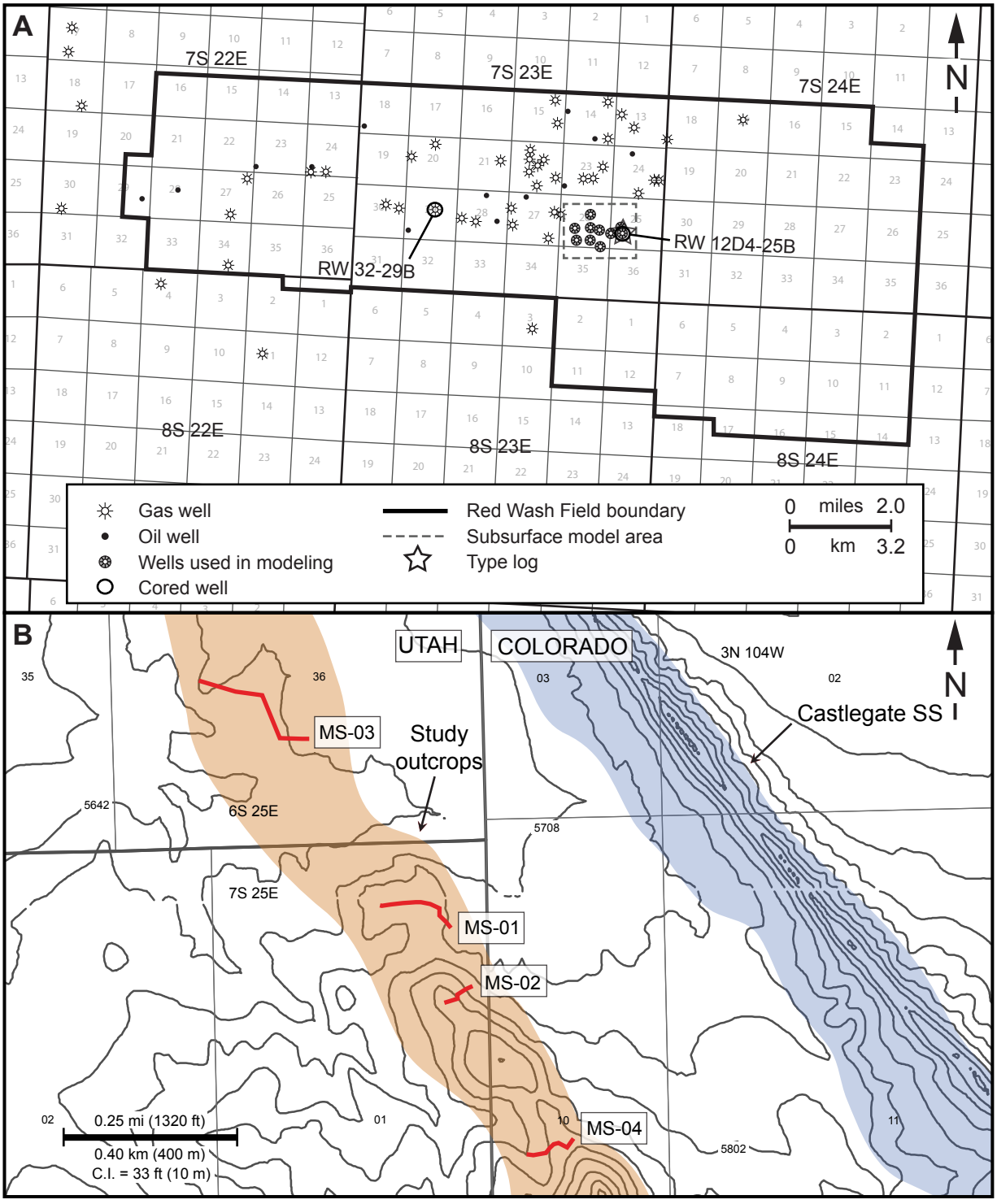

Figure 3. Detailed map showing the subsurface study area in Red Wash Field. Cored wells are located in section 25 and 29 of T7S R23E. Subsurface modeling in Petrel is confined to a smaller area outlined by the dashed box that contains 10 wells. B: Contour map showing the study outcrops (shaded orange; approximate strike/dip = 177°/12°) and locations of 4 measured sections. The Castlegate Sandstone hogback (shaded blue) is the basal unit of the Mesaverde Group in the outcrop study area. See Fig. 1 for locations of A and B.

emplaced to address the variation in sandstone-body connectivity. An outcrop-to-subsurface characterization of the lower Mesaverde Group fluvial deposits provides crucial information on reservoir heterogeneities that are necessary to reducing uncertainty in recovery estimates and developing cost-effective completion strategies.

TECTONIC AND STRATIGRAPHIC SETTING

The Uinta Basin is located in central and northeastern Utah and is approximately 9,300 mi^2 (24,000 km^2) in areal extent. It is asymmetrical in shape with a gently dipping southern flank and a steeply dipping northern flank associated with movement along a deep, high-angle reverse fault along the Uinta Uplift. The Uinta Basin is bound by the Wasatch Plateau and Mountains to the west, the Uinta Mountains to the north, the Book Cliffs to the south, the San Rafael Swell to the southwest, and the Uncompaghre Uplift to the southeast (Osmond, 1964) (Figure 1). The Douglas Creek Arch borders the eastern margin of the Uinta Basin and separates it from the Piceance Basin. Red Wash Field is located in the northeastern portion of the basin and is characterized by a low-relief, anticlinal nose plunging to the west at 1-2° (Chatfield, 1972; Kelley and Castle, 1975).

Beginning in the Early Cretaceous, active subduction along the western margin of the North American continent formed the Sevier thrust belt. The contractional stress regime of the Sevier orogeny, accompanied by flexural processes relating to convergent plate movement, formed the Rocky Mountain Foreland Basin, where the initial stages of Uinta Basin development began (DeCelles and Currie, 1996). The Laramide orogeny, beginning in the Late Cretaceous time, segmented the larger foreland basin into smaller, discrete basins through basement-involved reverse faulting and uplift (DeCelles and Currie, 1996; Hettinger and Kirschbaum, 2002, 2003; Johnson, 2003; DeCelles, 2004).

During the Late Cretaceous (95 – 66 Ma), an epicontinental sea, known as the Cretaceous Interior Seaway, encroached upon the western interior from the north, allowing sediments to be shed via fluvial systems from the Sevier highlands into the Rocky Mountain Foreland province to the east through a combination of marine and continental settings (Hettinger and Kirschbaum, 2002, 2003; DeCelles, 2004) (Figure 4A). The seaway reached maximum extent during the

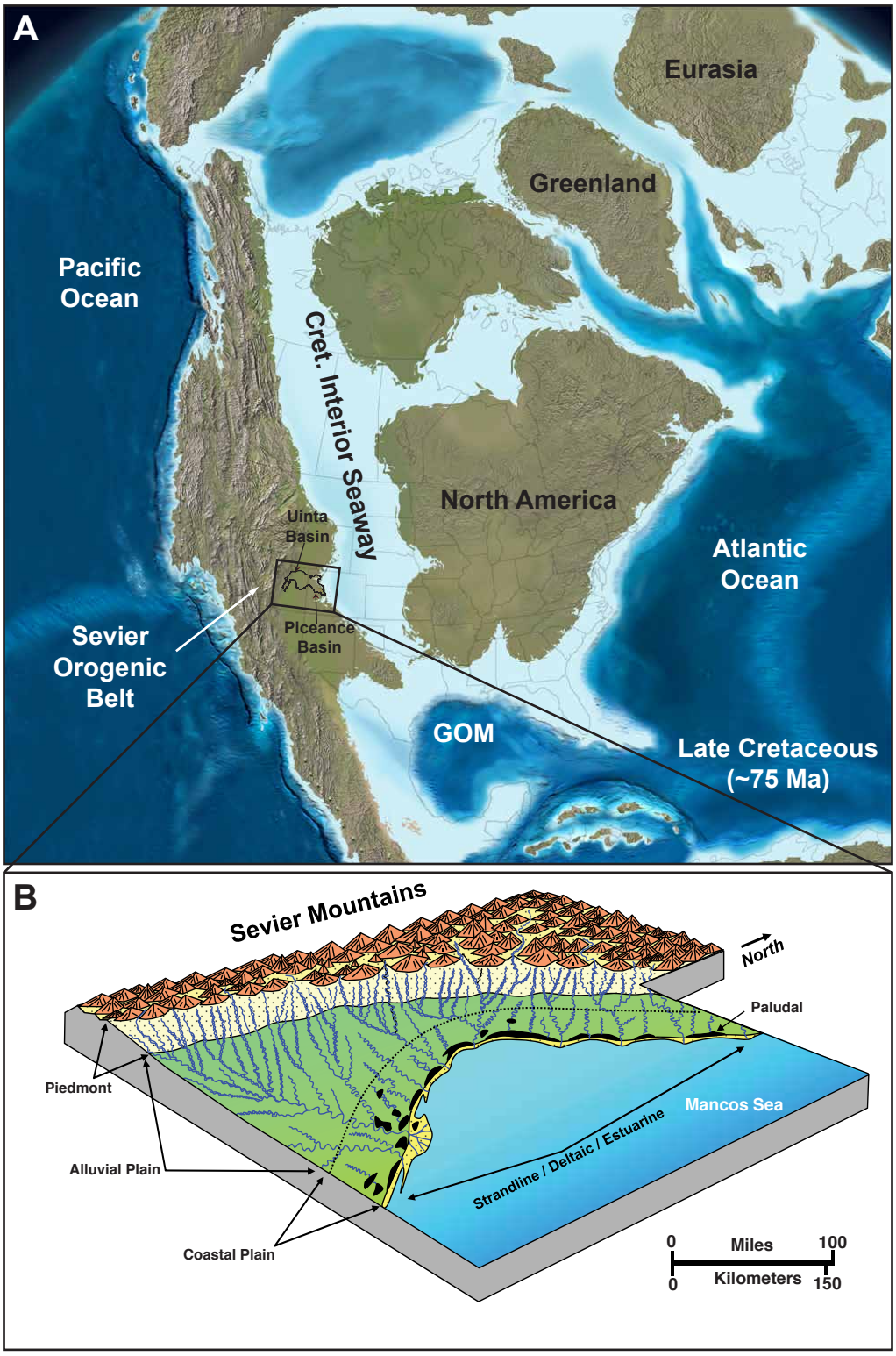

Figure 4. A: Paleogeographic reconstruction of North America during the Campanian (Late Cretaceous; ~75 Ma) showing the location of the Cretaceous Interior Seaway in relation to the present-day Uinta and Piceance basins. Modified from Blakey (2008). B: Schematic diagram showing the types of depositional environments of the Mesaverde Group. Modified from Ryer and McPhillips (1983) and Cole and Cumella (2003).

Turonian (93.9 – 89.9 Ma) and permanently retreated from the area during the Maastrichtian (72.1 – 66.0 Ma) (Hettinger and Kirschbaum, 2002, 2003). During the initial stages of seaway regression, the area now occupied by the Uinta Basin was proximal to the western shoreline of the Cretaceous Interior Seaway. Variations in sea level and sediment supply allowed the position of the ancient shoreline to fluctuate, causing a complex depositional configuration of alluvial-plain, deltaic, estuarine, coastal-plain, and marine environments (Hettinger and Kirschbaum, 2002, 2003; Cole, 2008) (Figure 4B).

Deposition of the Mesaverde Group occurred mostly during the Campanian (83.6 – 72.1 Ma) and is comprised of fluvial and near-shore marine sediments that shoal upward stratigraphically, reflecting the overall basinward movement of the shoreline as the Cretaceous Interior Seaway regressed (Osmond, 2003). Stratigraphic nomenclature referred to in this study follows Franczyk and others (1990) and Hettinger and Kirschbaum (2002, 2003), where the main body of the Mesaverde Group rests conformably on top of the Mancos marine shale and unconformably below the Tertiary strata of the Wasatch Formation (Figure 2). The Mesaverde Group in the eastern Uinta Basin is made up of the Blackhawk Formation, Castlegate Sandstone, Sego Sandstone, Neslen Formation, Farrer Formation, and Tuscher Formation. However, inconsistencies in the characteristics and extent of each of these units arise from local variability in depositional controls, as well as ambiguities that exist within the nomenclature.

The Blackhawk Formation is considered the basal unit of the Mesaverde Group in the subsurface study area. However, it pinches out near the Utah-Colorado state line and is not present in the outcrop location (Hettinger and Kirschbaum, 2002, 2003; Johnson, 2003). The Castlegate Sandstone forms a prominent hogback within the outcrop study area and was deposited in a braided fluvial environment (Lawton, 1986; Hettinger and Kirschbaum, 2002, 2003). The last incursion of

the seaway is represented by a thin unit of offshore marine mudrock known as the Buck Tongue of the Mancos Shale, which separates the Castlegate and Sego sandstones before grading into the Mancos Shale east of the Utah-Colorado border (Franczyk et al., 1990; Hettinger and Kirschbaum, 2002, 2003; Johnson, 2003). The Sego Sandstone lies conformably and unconformably above the Buck Tongue, and was deposited in a marginal-marine environment dominated by tidal and fluvio-deltaic processes (Van Wagoner et al., 1990; Painter et al., 2013). Conformably above the Sego Sandstone is the Neslen Formation, which makes up the study interval. It consists of very-fine- to medium-grained sandstones, siltstones, carbonaceous mudstones, and coals that were deposited in lower alluvial-plain and coastal-plain settings (Lawton, 1986; Franczyk et al., 1990; Hettinger and Kirschbaum, 2002, 2003; Cole, 2008). Franzczyk and others (1990) describe the Neslen Formation as being comprised of tidally influenced meandering river deposits, while McLaurin and Steel (2000) and Yoshida and others (1996) interpret the Neslen equivalent strata west of Green River as principally interdistributary, fluvial, and overbank deposits. These studies demonstrate that this geologic unit can exhibit characteristics from a wide array of depositional environments within the same basin. For the subsurface 3-D modeling, the study interval was divided into six zones based on coal occurrence, net-to-gross ratio, and facies changes (Figure 5; Appendix F). The distinct carbonaceous mudrock of the Neslen Formation transitions sharply into the non-coal bearing, non-carbonaceous mudrock, and fluvial sandstones of the Farrer Formation, which grades upward into the thick, laterally discontinuous sandstones of the Tuscher Formation. The Tuscher Formation is distinguished from the Farrer Formation by having a higher sandstone content (Hettinger and Kirschbaum, 2002, 2003; Cole, 2008). However, this distinction can be unclear, and therefore the thickness of the Farrer and Tuscher formations can differ dramatically (White et al., 2008).

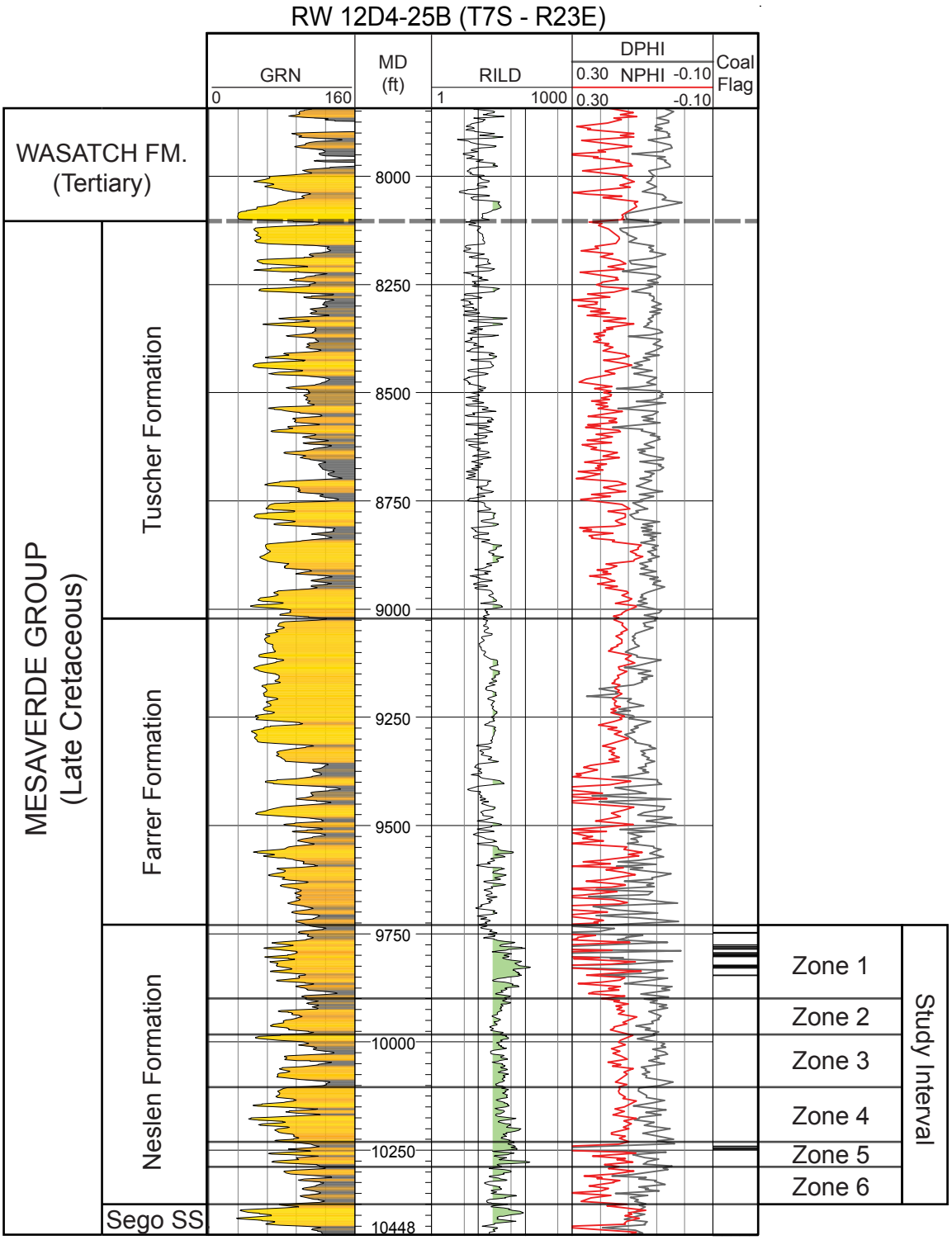

Figure 5. Type log for the Mesaverde Group in Red Wash Field (RW 12D4-25B, API - 43047519050000; see Figure 3A for location). A regional unconformity separates the Cretaceous-age Mesaverde Group from the Tertiary Wasatch Formation. Deep resistivity (RILD) values greater than 20 ohm-m are shaded green. The study interval was divided into six zones for the subsurface 3-D modeling.

LITHOFACIES ASSOCIATIONS AND ARCHITECTURAL ELEMENTS

Component lithofacies of the lower Mesaverde Group were carefully examined through a combination of core descriptions, core-to-log comparisons, and outcrop observations to reconstruct local depositional characteristics. Two cores (773 ft, 235 m) from Red Wash Field (RW 12D4-25B and RW 32-29B; Figure 3A) and four measured sections (650 ft, 195 m) along the Douglas Creek Arch (Figure 3B) were described in terms of lithology, grain size, physical and biological structures, and organic content to produce twelve distinct lithofacies commonly found within the study interval. Lithofacies descriptions are summarized in Table 1 and include: (A) planar-laminated sandstone and mudrock, (B) wavy-laminated sandstone and mudrock, (C) structureless mudrock, (D) coal, (E) high-angle trough cross-stratified sandstone, (F) low-angle trough cross-stratified to horizontal-planar-laminated sandstone, (G) structureless sandstone, (H) mudstone-clast conglomeratic sandstone, (I) carbonaceous siltstone, (J) ripple-cross-laminated sandstone, (K) contorted sandstone and mudrock, and (L) finely laminated sandstone and mudrock (see Appendix A for photos). The RW 12D4-25B core description starts at the top of the Sego Sandstone and spans the largest proportion of the study interval, while the RW 32-29B core extends from the upper part of the study interval into the overlying Farrer Formation (see Appendix A, Figure A1). Porosity and permeability measurements (ambient and confined) from core plugs were available for the RW 12D4-25B core, as well as a well-log suite including gamma ray (GRN), deep resistivity (RILD), bulk density (RHOB), density porosity (DPHI), and neutron porosity (NPHI). Gamma ray (GRN) was available for the RW 32-29B core. The locations of outcrop-measured sections (Figure 3A) are about 10 – 15 mi (16 – 24 km) northeast of the closest wells in Red Wash Field. Spectral gamma-ray measurements were recorded along each measured section in 1 ft (0.3 m) increments using an RS-125 Super Spec hand-held

Code	Facies Name	Description	Interpretation
A	Planar-laminated sandstone/mudrock	**Texture/color:** interlaminated dark grey mudrock (80%) and fine sand (20%) **Structures:** planar laminations; mud lamina: 0.25-1.0 in (0.6-2.5 cm), sand lamina: < 0.25 in (0.6 cm) **Comments:** contains coal stringers and carbonaceous debris; P*lanolites* and T*halassinoides* burrows; only found in lowest part of 12D4-25B core	brackish water, low energy setting
B	Wavy-laminated sandstone/mudrock	**Texture/color:** interlaminated sand (60-80%) and grey mudrock (20-40%) **Structures:** wavy to lenticular, irregular laminations **Comments:** contains mineralized, broken natural fractures; cemented; only present in 12D4-25 B core (max 6.5 ft [2 m]thick)	low-energy channels, brackish water influence
C	Structureless mudrock	**Texture/color:** Dark grey mudrock **Structures:** structureless **Comments:** organic rich, contains disseminated plant material; exhibits dessication cracks in core; 1-12 ft [0.3-3.6 m] thick	overbank, back-swamp, or abandoned channel deposits; low energy
D	Coal	**Texture/color:** Dark grey to black, dull to glossy bituminous coal **Structures:** fissile to crumbly **Comments:** generally sharp contacts with facies above and below; sometimes gradational contacts with Facies C (Structureless mudrock); 0.5-3 ft [0.2-1 m] thick	swamp/marsh deposits
E	High-angle cross-bedded sandstone	**Texture/color:** light grey, shaley fine- to medium-grained sandstone **Structures:** high-angle trough crossbeds, contorted bedding **Comments:** commonly contains mud rip-up clasts; 1-3 ft [0.3-1 m] thick	accretionary macroforms, high flow regime; dewatering structures from rapid deposition
F	Low-angle cross-bedded to horizontal-planar-laminated sandstone	**Texture/color:** light grey, fine- to medium-grained sandstone **Structures:** low-angle trough crossbeds; horizontal planar to ripple laminations **Comments:** common fining-upward grain size trends; 1-11 ft [0.3-3.3 m] thick	scour fill, accretionary macroforms, transitional dune form
G	Structureless sandstone	**Texture/color:** light grey to beige medium-grained sandstone **Structures:** structureless **Comments:** contains sparse mud rip-up clasts; structures may have been destroyed by cryptic bioturbation	rapid sediment deposition; high energy
H	Mudstone-clast conglomeratic sandstone	**Texture/color:** light grey, fine- to medium-grained sandstone **Structures:** structureless **Comments:** contains chaotic concentrations of large mud rip-up clasts; 0.5-3 ft [0.2-1 m] thick	high energy transport of rip-up clasts, erosional lag deposits; scour and fill
I	Carbonaceous siltstone	**Texture/color:** light- to brown-grey sandy siltstone **Structures:** structureless **Comments:** organic rich with abundant root traces; 2.5-18 ft [0.8-5.4 m] thick	back-swamp, overbank, or abandoned channel deposits; incipient soil development; low energy
J	Ripple-cross-laminated sandstone	**Texture/color:** light grey, very fine- to medium-grained sandstone **Structures:** high density of ripple laminations (climbing ripples) **Comments:** laminae containing shale and organic material separate ripple packages; 0.75-5 ft [0.2-1.5 m] thick	steady unidirection current (asymmetric ripples), low flow regime
K	Contorted sandstone/mudrock	**Texture/color:** dark grey to bluish grey, shaley siltstone or medium-grained sandstone **Structures:** highly contorted/convoluted bedding **Comments:** 1-12 ft [0.5-3.6 m] thick, contorted sandstone common in outcrop	rapid deposition, dewatering structures from sediment load
L	Finely laminated sandstone/mudrock	**Texture/color:** finely laminated fine-grained sandstone (> 80%) and siltstone/mudrock **Structures:** thin planar laminations **Comments:** lamina very thin (< 0.2 in [1 mm]), can be slightly wavy; may contain small burrows between lamina; 1-6 ft [0.5-1.8 m] thick	unidirectional flow, upper flow-regime plane-bed lamination

Table 1. Lithofacies of the lower Mesaverde Group from core descriptions and outcrop observations.

spectrometer to create outcrop gamma-ray log profiles that display total counts per second (cps) and the concentrations of potassium (K, %), thorium (Th, ppm), and uranium (U, ppm) (Appendix B).

The twelve lithofacies were analyzed collectively to identify four "facies associations": fluvial channels, brackish-water environment, overbank environment, and swamp/mire setting. Four architectural elements were interpreted based on the facies associations, which include fluvial bars, crevasse splays, floodplain deposits, and coal. Architectural elements differ from facies associations in that they have a distinct geometry and spatial distribution. They were initially defined by Allen (1983), and later formally defined by Miall (1985) as "components of a depositional system equivalent in size to, or smaller than a channel fill, and larger than an individual lithofacies unit, characterized by a distinct facies assemblage, internal geometry, external form and vertical profile".

The fluvial channel environment is dominated by sandstone fluvial bars that consist of facies E, F, G, and H, and less commonly contains facies J, K, and L. The term "fluvial bars" includes undifferentiated point bars and other channel bars (e.g., mid-channel bars) because this study does not distinguish the specific type of channel bar (Bridge and Tye, 2000; Holbrook, 2001; Bridge, 2006; Patterson et al., 2012). Fluvial bars commonly have a sharp, erosive base that is represented in core by a mudstone-clast conglomerate (facies H) or an abrupt grain-size change in sandstone lithologies, where a younger fluvial bar erodes into an older one below (Figures 6 and 7). A common facies succession includes mudstone-clast conglomeratic sandstone (H) at the base, followed by structureless sandstone (G), high-angle trough cross-stratified sandstone (E), or low-angle trough cross-stratified to horizontal-planar-laminated sandstone (F). Ripple-cross-laminated sandstone (J), convolute sandstone/mudrock (K), and finely horizontal

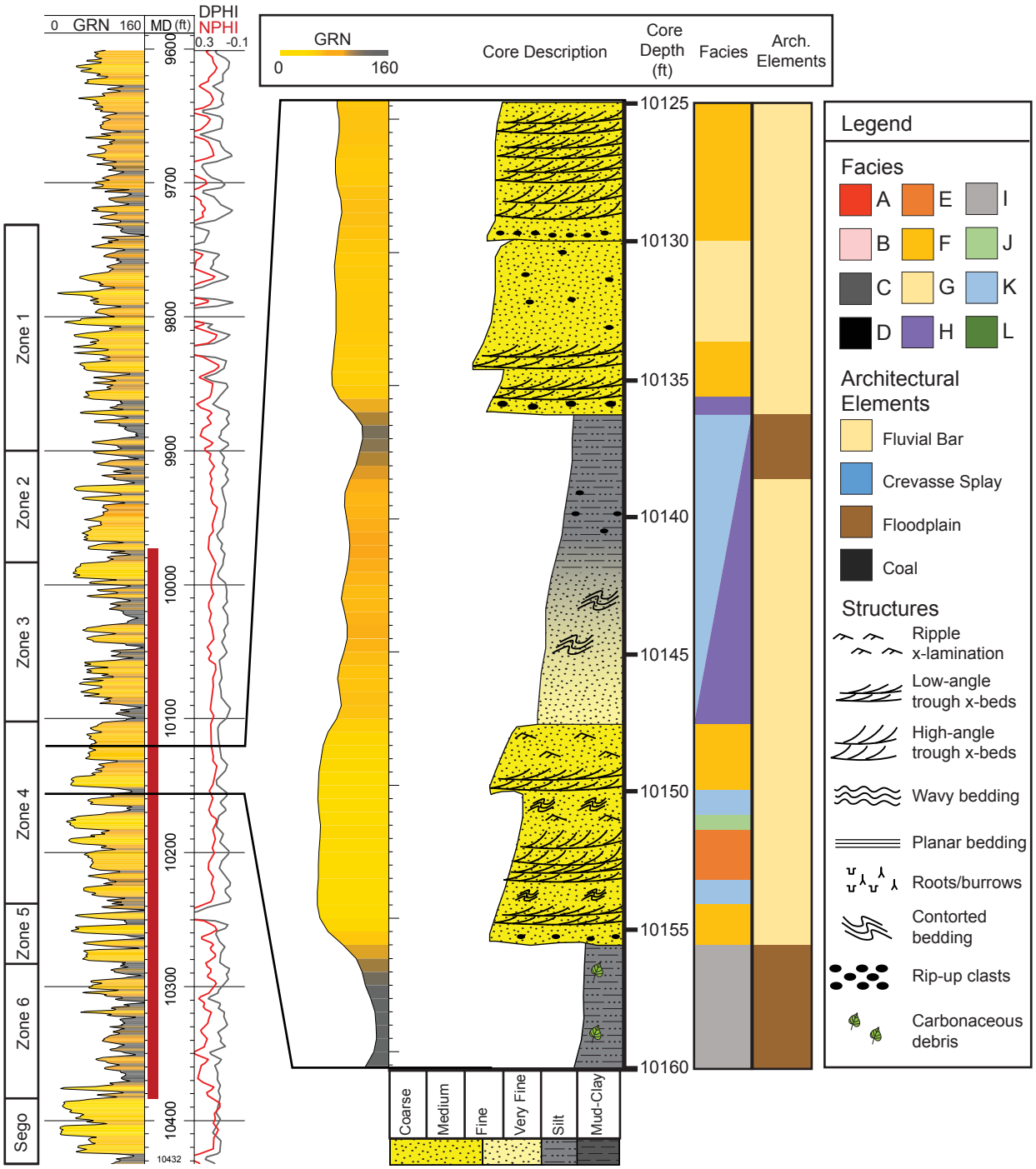

Figure 6. Core-to-log comparison of a high net-to-gross interval in RW 12D4-25B. The red bar represents the cored interval (log depth = core depth - 5'). Fluvial bar elements (GRN < 96 API) are generally sharp based, display a fining upward log character, and exhibit evidence of stacking and reworking. Floodplain was interpreted in gamma-ray intervals greater than 96 API.

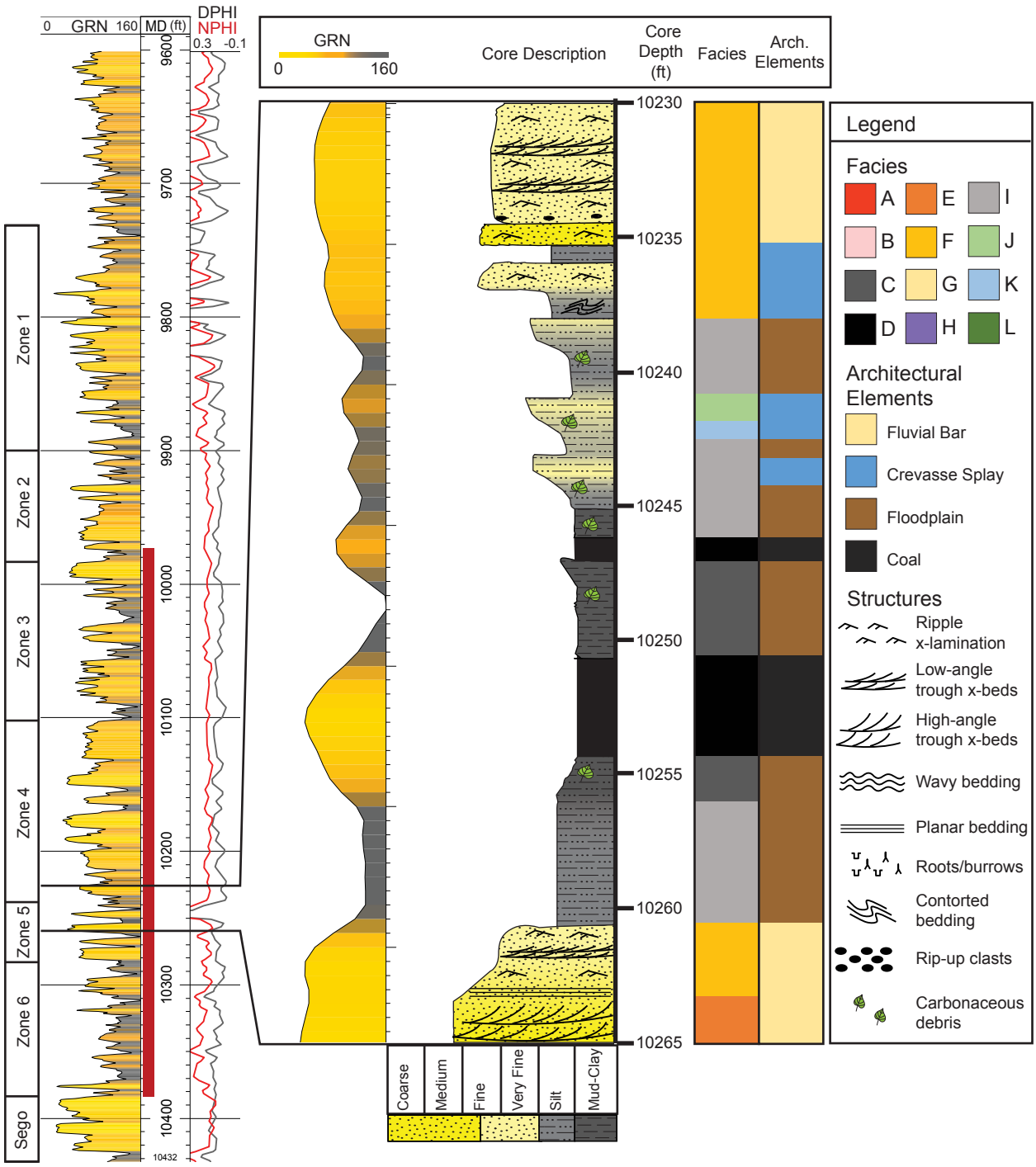

Figure 7. Core-to-log comparison of a coaly, low net-to-gross interval in RW 12D4-25B. The red bar represents the cored interval. Sandstone fluvial bars and crevasse splays can be directly stacked or separated by a thin bed of mudrock, which is represented by a slight inflection in the gamma-ray log (10235 ft). Coal was picked in intervals where GRN < 96 API and DPHI > 0.25.

laminated sandstone/mudrock (L) can occur at the top of channel elements, but are rare most likely because they are prone to scouring during the deposition of a younger channel element. Fluvial bars can be bounded above or below by floodplain deposits, crevasse splays, or other stacked fluvial bars. The cored interval is comprised of 34.2% and 25.8% fluvial bar architectural elements in RW 12D4-25B and RW 32-29B, respectively, and range from 2.5 – 20 ft (0.75 – 6.0 m) in thickness. For comparison, fluvial bar thickness measurements (N = 24) from an outcrop study conducted approximately 30 miles away from Red Wash Field along the Douglas Creek Arch range from 1.0 – 30.0 ft (0.3 – 9.0 m) (Hlava, 2011).

Planar-laminated sandstone/mudrock and wavy-laminated sandstone/mudrock (facies A and B) are common in outcrop, but are present only in the lowermost part of the RW 12D4-25B core near the contact with the Sego Sandstone (Appendix A). Facies A and B are interpreted to reflect a brackish-water environment, where freshwater derived from fluvial systems mixes with open-marine seawater in tidal-fluvial channels and estuaries. The presence of bioturbated, planar- and wavy-laminations (>80% mudrock, facies A) indicate that sand and mud from a mixed source was alternating between bedload and suspension deposition within the low-energy estuarine central basin. Trace fossils include a low-abundance and low-diversity assemblage of *Thalassinoides* and *Planolites* burrows, indicative of a brackish-water setting. In the RW 12D4-25B core, bioturbation becomes sparse or absent around 10,350’ ft, marking the transition of brackish-water, paralic deposits into continental deposits. Brackish-water influence on fluvial channels is represented by higher sandstone content in heterolithic strata and minor bioturbation forming as a result of intermittent tidal inundation. Tidal-fluvial channels are dominated by structureless sandstone (G), mudstone-clast conglomeratic sandstone (H), interbedded wavy- to planar-laminated sandstone (60 – 80% sandstone, facies B), contorted sandstone/mudrock (K),

carbonaceous mudrock (I), structureless mudrock (C), and coal laminae. Within the outcrop area, heterolithic strata of facies A and B are associated with carbonaceous mudrock and coals overlain by sharp-based sandstone bodies interpreted as tidal-fluvial channels or other brackish-water elements (e.g., tidal barform). The thickest sandstone units (up to 10 ft, 3.0 m) in MS-04, possibly of bayhead-delta origin, are trough cross-bedded, bidirectional-ripple cross-laminated toward the top, and display a high degree of contorted bedding and escape structures, and lie sharply on carbonaceous mudrock or coal. These sandstone bodies represent the highest energy setting within the study area (Figure 8; Appendix B, Figure B1). Sandstone units in MS-01 and MS-02 are thinner (2.0 – 6.0 ft, 0.6 – 1.8 m) and are dominated by bidirectional-ripple cross-laminations, heterolithic strata, and carbonaceous mudrock (Appendix B, Figure B2), which are interpreted as tidal-fluvial channels. MS-03 contains the least amount of sandstone and thickest carbonaceous mudrock successions, which are indicative of the lowest energy setting observed within the field area, likely within the central basin of an estuary. This trend suggests that energy of the depositional system was decreasing toward the northwest and moving farther away from the main channel axis. The lack of well-developed lateral-accretion deposits and presence of bidirectional-ripple laminations within sandstone bodies further suggests deposits within the outcrop area display a brackish-water influence. However, poor outcrop preservation and exposure make identification difficult. Therefore, it should be noted that even though the majority of fluvial deposits observed within the outcrop belt were interpreted to reflect a tidal influence, it is possible that there were aspects of purely freshwater, fluvial elements present, but not observable. However, tidally influenced fluvial bars do not display distinct differences in spectral-gamma ray character and are grouped with the fluvial bar architectural element.

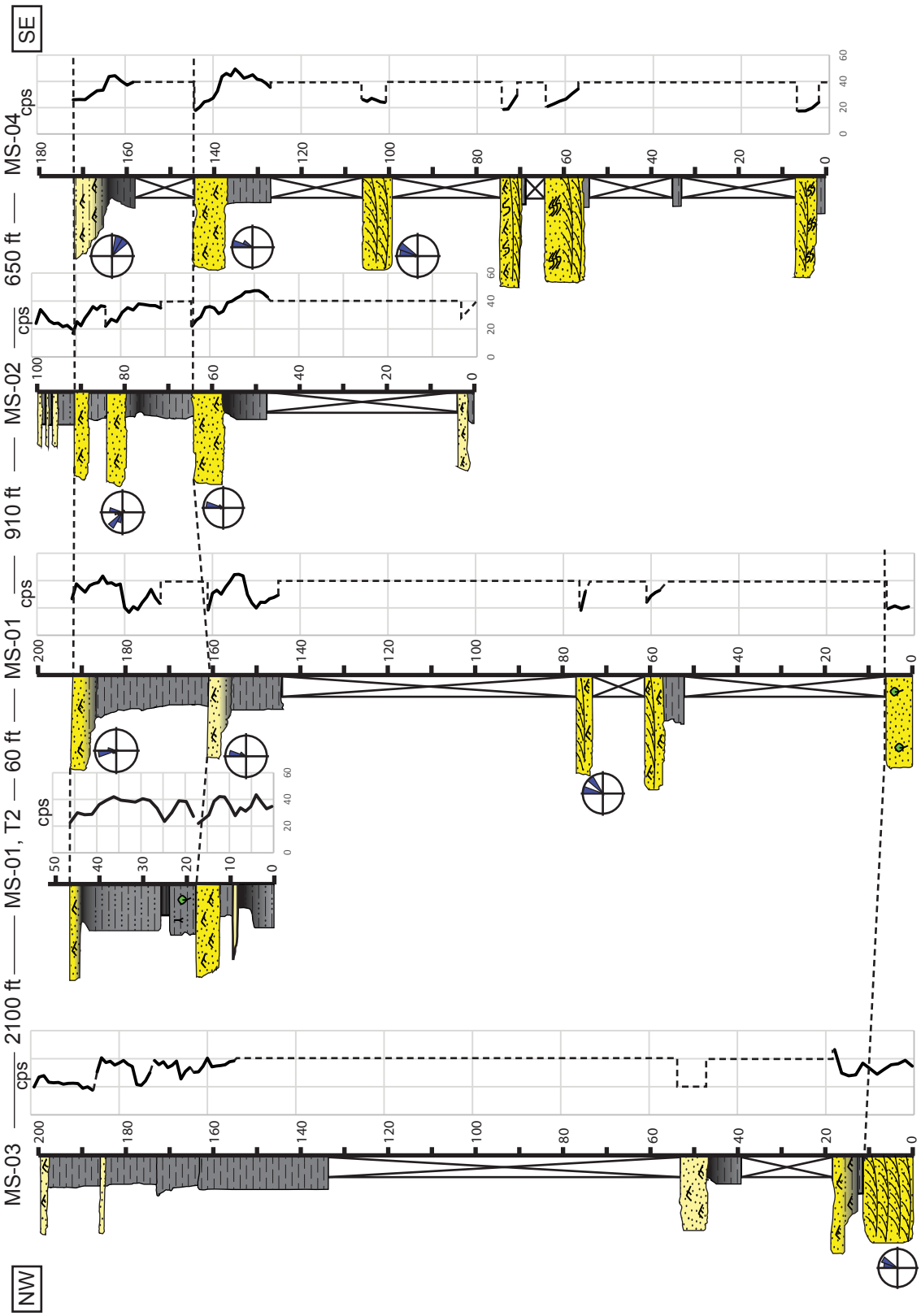

Figure 8. Northwest to southeast cross section of measured sections. Correlations were made (dotted lines) by walking the contacts between units. Rose diagrams of structurally uncorrected paleocurrent measurements are next to the unit they represent (bedding strike/dip = 177°/12°).

The overbank environment consists of mixed sandstone and mudstone crevasse splays and mudstone-dominated floodplain deposits. Crevasse splays are broadly lenticular or fan-shaped, very fine-grained sandstone bodies that form when the channel margins are breached during high-flow events. They are fed by ribbon-like channels that divert from the main channel and prograde out onto the floodplain (Miall, 1996, 2006). In core (Figures 6 and 7), crevasse splays range from 1.0 – 5.0 ft (0.3 – 1.5 m) thick. For comparison, crevasse splay thickness measurements (N = 6) from an outcrop study conducted approximately 30 miles away from Red Wash Field along the Douglas Creek Arch range from 1.0 – 4.5 ft (0.3 – 1.4 m) (Hlava, 2011). They commonly occur as discrete ripple-cross-laminated or contorted, upward-coarsening shaley sandstones (facies J and K) bound by rooted and carbonaceous mudstones on the floodplain (facies C and I). Mudstone-clast conglomeratic sandstone (H) and low-angle trough cross-stratified sandstone (F) is also present, but rare. Contorted mudrock and siltstone reflect soft-sediment deformation occurring during rapid deposition of suspended fine-grained sediments in shallow water on the floodplain. Crevasse splays can have gradational upper and lower contacts with floodplain deposits reflecting decreasing energy levels during flood retreat. The crevasse splay architectural element makes up 16.9% and 8.8% of the cored interval in RW 12D4-25B and RW 32-29B, respectively. The floodplain element is made up of structureless mudrock and carbonaceous siltstone (facies C and I), and was deposited by overbank sheet flow and suspension settling of fine-grained sediments. Root traces present in the mudrock and sandstone splays indicate there were areas on the interfluve fit for soil and vegetation development. Carbonaceous mudrock was likely derived from silt and mud mixing with plant material on the floodplain. The fine-grained floodplain matrix makes up 45.9% and 57.8% of the cored interval in RW 12D4-25B and RW 32-29B, respectively. In outcrop, prograding crevasse splays form the

tops of coarsening upward successions that grade from structureless mudrock and organic rich mudrock (floodplain facies C and I) into tabular, ripple-laminated sandstones deposited by unconfined flows (Appendix B, Figure B1). Floodplain successions are typically slope forming and contain disseminated plant debris, localized coal stringers, thin interbedded siltstones and sandstones, and dinosaur tracks (Appendix B, Figure B1).

The presence of coal beds (facies D) demonstrates that peat accumulation was occurring within swamps and mires proximal to the main channel system. The preservation of peat occurs close to the water table, which is controlled by sea level in paralic settings, thus implying the channel system must have been proximal to the shoreline (Bohacs and Suter, 1997). Coals are generally associated with floodplain deposits (facies C and I) and contacts can be sharp or gradational. Coal fragments and organic matter are documented in (C) structureless mudrock, where mud and peat became intermixed during swamp inundation on the floodplain. Coal makes up approximately 1.3% of the cored interval in RW 12D4-25B and 7.6% in RW 32-29B, and can be up to 4.5 ft (1.3 m) thick.

The ultimate purpose of the facies analysis conducted in this study is to predict the occurrence of facies associations and architectural elements in non-cored wells by comparing the core descriptions to their respective wireline logs. Gamma-ray logs were normalized using a 2-point histogram normalization process to remove variability in each well caused by different wireline logging tools (Shier, 2004) (see Appendix E for summary). Architectural elements were then manually interpreted in each non-cored well using criteria derived from core-to-log comparisons (Figures 6 and 7). Lithology logs were calculated using normalized gamma-ray (GRN) logs and density-porosity (DPHI) logs to distinguish between sandstone, mudrock, and coal. Sandstone was calculated using a gamma-ray cutoff of less than 96 API units, mudrock was

calculated using a gamma-ray cutoff greater than or equal to 96 API units, and coal was calculated with gamma-ray values less than 96 API units and density-porosity values greater than 0.25. Fluvial bars were interpreted within sandstone lithologies. They are generally sharp based, and express a fining upward or blocky grain size trend. The presence of mudstone-clast conglomerates at the base of some fluvial bars causes the gamma-ray signature to appear gradational, when in reality the contacts are sharp in nature. Crevasse splays were also interpreted in sandstone lithologies, but are distinguished from fluvial bars in that they are thinner, have a more shaley gamma-ray response, and commonly display a coarsening upward signature (i.e., decreasing gamma-ray). Fine-grained floodplain matrix was defined in mudrock lithologies greater than 96 API units. Although uncommon, it should also be noted that mudrock-dominated sections within the lowest intervals (i.e., immediately above the Sego sandstone) can exhibit lower gamma-ray values due to carbonate cements, making them appear as clean, blocky sandstones. These intervals were classified as "undefined".

To summarize the findings from core and outcrop observations, the deposits of lower Mesaverde Group within the study area accumulated in predominantly freshwater settings on the lower coastal plain, adjacent to the paleoshoreline. The lack of well-defined, lateral-accretion sets, overall low net-to-gross ratio, presence of terrestrial dinosaur tracks, and high percentage of mudrock in both the field site and core suggest deposition likely occurred off axis from the main fluvial system in low-energy channels. Although accurately correlating outcrop to the subsurface is difficult without well-defined marker beds, both data sets express similar trends with the presence of coal and successions of carbonaceous mudrock grading into thin, stacked siltstones and sandstones. However, the sandstone bodies in outcrop are much thinner, contain an abundance of lower-flow-regime sedimentary structures (with the exception of MS-04), and do

not display complex stacking when compared to the cored wells. The outcrop also displays a higher proportion of fine-grained facies, thicker floodplain successions in between sandstone bodies, and more evidence of brackish-water influence relative to the subsurface. These differences can be reconciled by suggesting the outcrop deposits were either closer to the paleoshoreline, more distal from the main channel-belt axis, or a combination of both relative to the contemporaneous coastal-plain deposits in the subsurface. This could possibly reflect a decreasing trend in energy of the system toward the northeast, where the outcrop deposits were further subjected to brackish-water processes compared to the subsurface deposits at Red Wash Field, which only display marine influence in the lowermost interval.

THREE-DIMENSIONAL MODELS OF FLUVIAL DEPOSITS

Spatial variability of fluvial architecture and sandstone connectivity in the subsurface at Red Wash Field was assessed through three-dimensional modeling using multi-point geostatistics. Multi-point geostatistics, herein referred to as MPS, is a stochastic, pixel-based method that uses a training image to establish a geologic concept among facies or architectural elements (Guardiano and Srivastava, 1993; Strebelle and Journel, 2001; Strebelle, 2002). A training image is a 3-D volume that serves as a database of geologic patterns. Patterns extracted from the training image are stored in a search tree, along with the probability of their occurrence. Once hard data (i.e., from well logs) has been assigned to the closest grid cell, the MPS algorithm references the search tree and subsequently populates each cell in the model framework based on pattern probabilities from the training image. This method was chosen over variogram-based and Boolean methods, such as sequential indicator simulation and object-based modeling, for a variety of reasons. First, the variogram is a chiefly statistical tool that is used to describe the dissimilarities of one variable at two spatial locations. The consequence of this is that the variogram only gives a measure of linear continuity, and is thus not sufficient to reproduce curvilinear geometries or capture geologically complex relationships (Caers and Zhang, 2004; Strebelle, 2006). Also, because the dataset is relatively sparse in the modeling area, choosing variogram inputs and directions can be difficult. In MPS, the training image replaces the variogram. Therefore, the user can create a geologic concept using object-based modeling, a hand-drawn sketch, or a digitized geologic sketch to create geologically reasonable reservoir models, while honoring available subsurface data. Object-based methods populate the model with user-defined facies objects, such as channel or ellipsoid shapes (Shepherd, 2009). This method is advantageous in that it can honor geologic shapes and erosion rules, but it does not have the ability to control spatial relationships between deposits like the MPS approach (Liu et al., 2004). In this study, MPS was used to model fluvial systems within the lower

Mesaverde Group. In conjunction with MPS, object-based techniques were used to construct training images, while variogram-based methods were used to develop facies probability volumes. The MPS modeling of this study involves three comprehensive steps: (1) Develop a training image, (2) create and systematically test multi-point facies patterns, and (3) execute final MPS modeling that honors data constraints.

Model Framework

A stratigraphic framework (3-D model grid) was defined for the lower Mesaverde Group for an approximate 1 mi^2 (2.5 km^2) area of Red Wash Field (Figure 9). This area was selected because of the higher well density (10 wells) and availability of core (RW 12D4-25B). Seven horizons were correlated across the model area to produce six zones that extend from the top of the Sego Sandstone to just above the Neslen Formation (Figure 5). Stratigraphic zonation was determined based on net-to-gross ratio, facies changes, and coal occurrence in 10 wells on an approximate 40-ac spacing (1320 ft [396 m] between wells) within the model area (Appendix F). Net-to-gross ratio in this study is defined by the total sandstone volume from fluvial bars and crevasse splays divided by the total volume of the zone. Net-to-gross ratio varies within each zone from 27.6% to 55.3%. The dimensions of the model are approximately 6260 ft x 4213 ft x 550 ft (1878 m x 1264 m x 165 m) with a total of 4,069,800 cells. Individual cell size is 50 ft x 50 ft (15 m x 15 m). A proportional layering scheme was used for all zones to produce an average cell thickness of 1.4 ft (0.4 m). Although the thinnest crevasse splay observed in core was 1.0 ft (0.3 m), increasing the number of layers in each zone to decrease the cell thickness to less than 1.0 ft (0.3 m) would have caused the number of cells in the model framework to increase and thus cause the MPS process to be computationally exhaustive. Therefore, the cell thickness varies slightly at

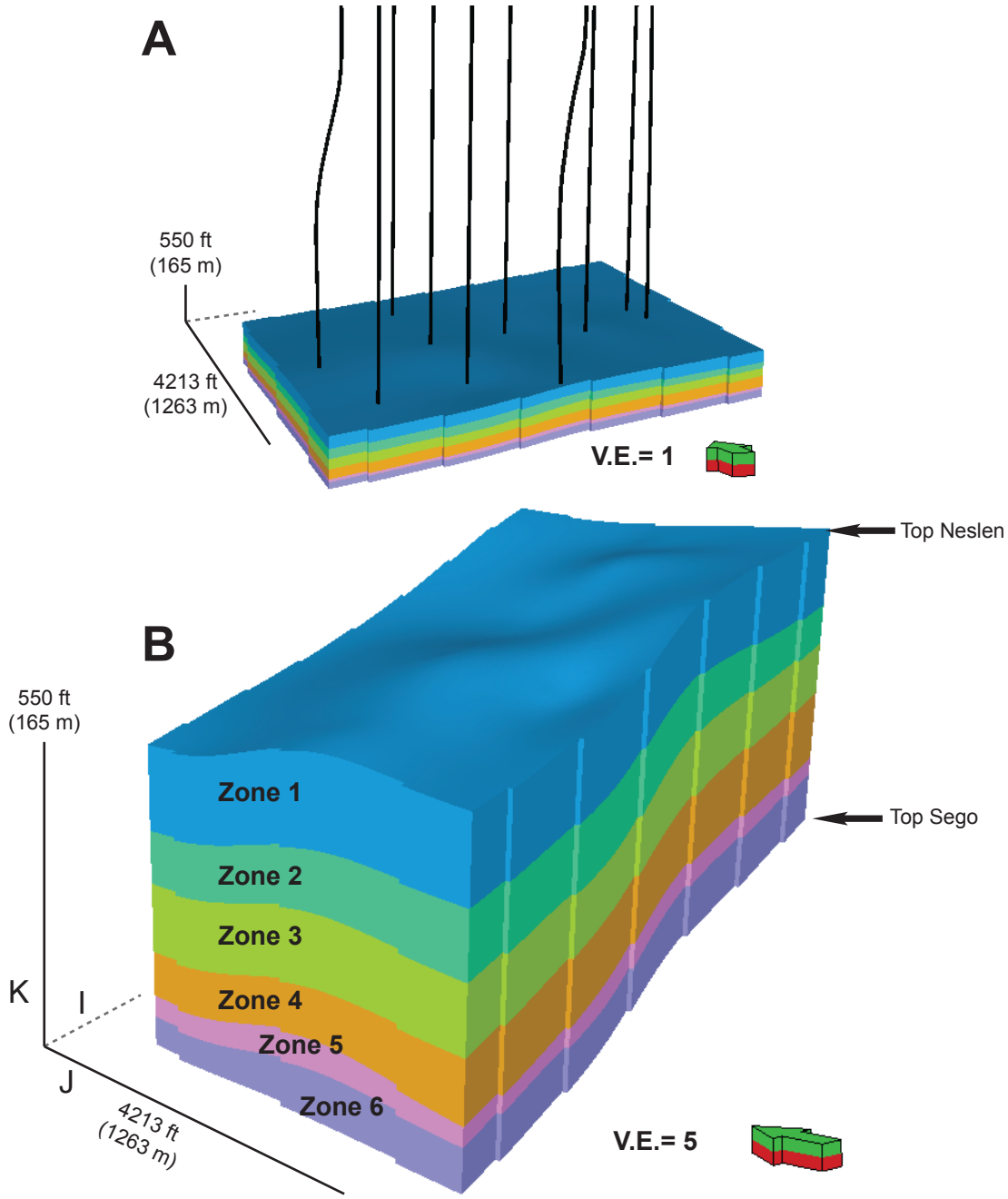

Figure 9. Three dimensional model framework for the lower Mesaverde Group (from the top of the Sego Sandstone to the top of the Neslen Formation). A: Location of 10 wells used in the modeling with no vertical exaggeration. B: Six zones were correlated within the model area based on facies changes, net-to-gross ratio, and coal occurrence. Model dimensions are approximately 6260 ft x 4213 ft x 550 ft (1878 m x 1263 m x 165 m).

each point because it is dependent on the number of layers chosen for each zone and thickness of the zone at that particular point. Calculated lithology logs and manually interpreted architectural-elements logs were then upscaled to the model framework, so that model cells intersected by the well path are assigned the appropriate values from the logs. Statistics for thickness and upscaled architectural-element logs for each zone are in Table 2.

Training Images

To construct a training image, it is important to have a geologic concept in mind that encompasses the shapes, patterns, and spatial distribution of the facies or architectural elements of interest (Caers and Zhang, 2004; Harding et al., 2004; Strebelle, 2006). One can postulate the spatial distribution of fluvial deposits from studying outcrops and observing modern-day processes, but predicting the geometries of these deposits in the subsurface is challenging and there is significant uncertainty. For this study, two separate training images were created for each zone using object-based techniques to explore two end-member scenarios for how architectural elements (fluvial bars, crevasse splays, and floodplain) might be preserved in the subsurface (Figure 10). The first scenario uses a continuous, channel shape to represent a sinuous, channel geometry, where individual fluvial bars might be connected via a ribbon of sandstone (e.g., Donselaar and Overeem, 2008; Sloan, 2012). The second scenario uses a crescent shape to reflect smaller individual fluvial bars. Both scenarios use a fan-shaped object oriented perpendicular to channel axes for crevasse splays. Floodplain was chosen as the background lithology/architectural element. Coal was not included in the training images and was instead, deterministically placed into the model in a subsequent step, which is described later. Training images were built using a separate 3-D orthogonal grid, but geographically in the same location as the model grid. The

Zone	Layers	Zone Thickness (ft)			Architectural Element	Proportion (%)	AE Thickness (ft)			
		Min	Mean	Max			Min	Mean	Max	std
1	100	142	171	188	Fluvial Bars	30.0	1.8	8.8	24.6	5.3
					Crevasse Splays	5.3	1.8	2.5	5.3	1.0
					Floodplain	57.6	1.8	7.8	54.5	7.3
					Coal	7.1	1.8	2.5	5.3	1.1
2	60	67	100	155	Fluvial Bars	32.8	1.8	10.1	40.4	9.4
					Crevasse Splays	6.7	1.8	2.7	7.0	1.6
					Floodplain	60.2	1.8	10.1	58.0	10.5
					Coal	0.3	1.8	1.8	1.8	0.0
3	70	104	127	147	Fluvial Bars	40.7	3.5	12.9	63.3	12.9
					Crevasse Splays	7.4	1.8	2.9	10.6	2.0
					Floodplain	51.9	1.8	9.0	45.7	8.4
					Coal	0.0	0.0	0.0	0.0	0.0
4	60	87	122	147	Fluvial Bars	47.8	1.8	10.7	49.2	9.0
					Crevasse Splays	7.5	1.8	2.3	5.3	0.9
					Floodplain	44.7	1.8	7.0	29.9	6.0
					Coal	0.0	0.0	0.0	0.0	0.0
5	30	34	52	62	Fluvial Bars	45.4	1.8	13.3	28.1	8.2
					Crevasse Splays	8.8	1.8	4.0	8.8	2.3
					Floodplain	38.7	1.8	5.5	17.6	4.0
					Coal	7.1	1.8	3.5	5.3	1.1
6	60	62	94	114	Fluvial Bars	15.2	3.5	11.1	28.1	7.9
					Crevasse Splays	12.4	1.8	3.2	10.6	2.1
					Floodplain	71.3	1.8	11.0	36.9	8.2
					Coal	1.0	1.8	1.8	1.8	0.0

Table 2. Thickness statistics and architectural-element statistics by zone. Statistics sourced from Petrel software (Schlumberger).

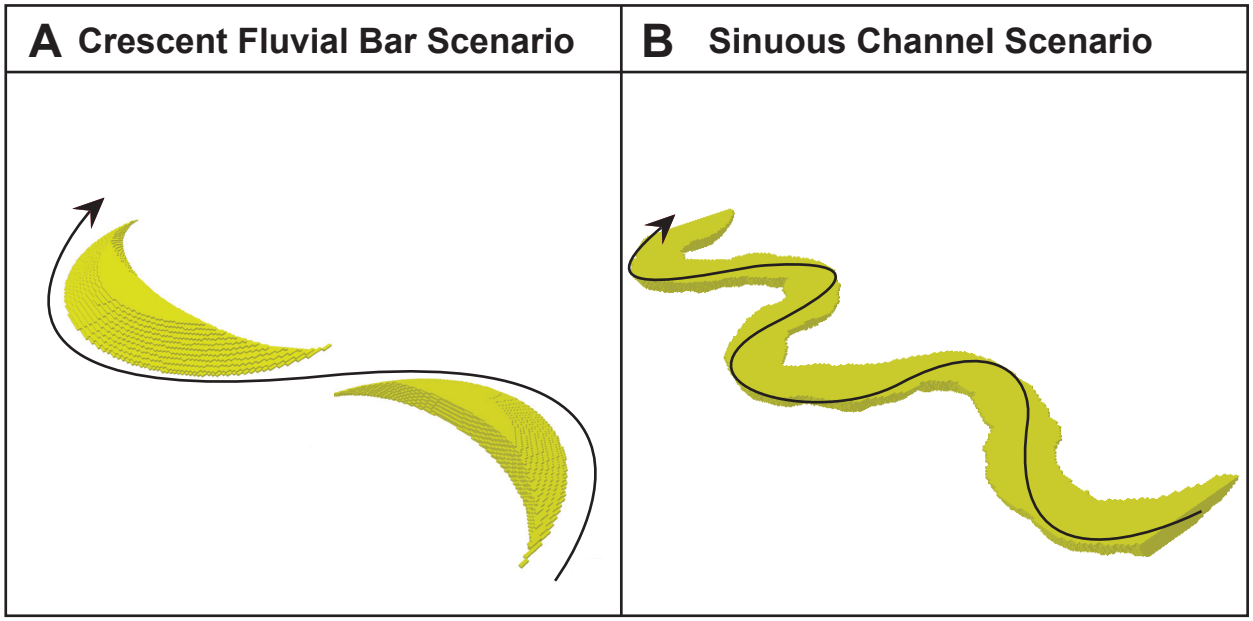

Figure 10. Example of two possible end member scenarios for fluvial bar preservation and the corresponding shape selected in Petrel. The black line represents the channel thalweg. A: Crescent-shaped fluvial bars may result when channels fill with mud after avulsion takes place. B: A sinuous, channelized geometry may result in a scenario where fluvial bars are connected by a thin ribbon of sandstone. Modified from Donselaar and Overeem (2008).

training image grid size was constructed to be approximately twice the size in the north-south direction relative to the model grid to capture the continuity of the channels in the dominant paleocurrent direction (22°) derived from outcrop data (Caers and Zhang, 2004). The grid measured approximately 7810 ft x 8820 ft x 30 ft (2343 m x 2646 m x 9 m) with a cell area of 50 ft x 50 ft (15 m x 15 m) and a thickness of 1 ft (0.3 m). As a rule of thumb, training-image global proportions should be similar (i.e., within 10%) to the architectural-element proportions desired in the final output model (Caers and Zhang, 2004; Strebelle, 2006). Therefore, training images were generated individually for each zone using a Boolean method (object-based) to replicate the respective proportions of architectural elements from the upscaled logs. The inputs for object dimensions honor thickness statistics from upscaled architectural element logs, outcrop geometry statistics of published data from Coal Canyon and other locations along the Douglas Creek Arch (Cole and Cumella, 2005; Panjaitan, 2006; Cole, 2008; Pranter et al., 2009; Hlava, 2011), in addition to outcrop data obtained from this study (Table 3). Channels and crescent-shaped fluvial bars were oriented using triangular distributions using statistics derived from paleocurrent indicators in the field ($\mu = 22°$). Crevasse splays were oriented perpendicular to channel axes to accurately capture their spatial relationship with respect to channel axes. Training images created in this study were meant to represent a geologic area over time, rather than a snapshot in time. Therefore, erosion rules were emplaced to allow younger deposits to partially remove older deposits, thus creating stacked cycles that represent channel migration through time.

SNESIM Algorithm

Before a training image can be used for MPS modeling, it must be analyzed to create a multi-point facies pattern. The SNESIM (Single Normal Equation SIMulation) algorithm is the

Sinuous Channel Scenario: Training Image Inputs (OBM)																
Zone	Architectural Element	Shape	Proportion (%)	Major Width (ft)					Thickness (ft)				Channel Layout		Orientation 1 (min, mean, max)	Orientation 2 (min, max)
				Min	Mean	Med	Max	Maj/Min Ratio	Min	Mean	Max	std	Amplitude (drift = 0.5)	Wavelength (drift = 0.5)		
1	Fluvial Bar	Channel	30	44.1	339.5	274.7	1700	-	-	8.4	-	5.0	1000	3000	-10°, 22°, 39°	-
	Crevasse Splay	Fan	5.3	40.1	231.1	198.7	843.3	0.8, 1, 1.2	1.4	2.4	5.3	-	-	-	-	-100°, 129°
2	Fluvial Bar	Channel	32.8	44.1	339.5	274.7	1700	-	-	10.0	-	8.5	1000	3000	-10°, 22°, 39°	-
	Crevasse Splay	Fan	6.7	40.1	231.1	198.7	843.3	0.8, 1, 1.2	1.4	2.7	7.7	-	-	-	-	-100°, 129°
3	Fluvial Bar	Channel	40.7	44.1	339.5	274.7	1700	-	-	13.1	-	13.6	1000	3000	-10°, 22°, 39°	-
	Crevasse Splay	Fan	7.4	40.1	231.1	198.7	843.3	0.8, 1, 1.2	1.7	2.9	10.2	-	-	-	-	-100°, 129°
4	Fluvial Bar	Channel	47.8	44.1	339.5	274.7	1700	-	-	12.6	-	11.4	1000	3000	-10°, 22°, 39°	-
	Crevasse Splay	Fan	7.5	40.1	231.1	198.7	843.3	0.8, 1, 1.2	1.7	2.7	6.9	-	-	-	-	-100°, 129°
5	Fluvial Bar	Channel	45.4	44.1	339.5	274.7	1700	-	-	13.3	-	8.2	1000	3000	-10°, 22°, 39°	-
	Crevasse Splay	Fan	8.8	40.1	231.1	198.7	843.3	0.8, 1, 1.2	1.4	3.8	9.5	-	-	-	-	-100°, 129°
6	Fluvial Bar	Channel	15.2	44.1	339.5	274.7	1700	-	-	10.1	-	7.0	1000	3000	-10°, 22°, 39°	-
	Crevasse Splay	Fan	12.4	40.1	231.1	198.7	843.3	0.8, 1, 1.2	1.3	3.0	10.2	-	-	-	-	-100°, 129°

Crescent-Shaped Fluvial Bar Scenario: Training Image Inputs (OBM)														
Zone	Architectural Element	Shape	Proportion (%)	Major Width (ft)					Thickness (ft)				Orientation 1 (min, max)	Orientation 2 (min, max)
				Min	Mean	Med	Max	Maj/Min Ratio	Min	Mean	Max	std		
1	Fluvial Bar	Crescent	30	44.1	339.5	274.7	1700	0.5, 0.8, 1	-	8.4	-	5.0	112°, 129°	-100°, -68°
	Crevasse Splay	Fan	5.3	40.1	231.1	198.7	843.3	0.8, 1, 1.2	1.4	2.4	5.3	-	-100°, 129°	-
2	Fluvial Bar	Crescent	32.8	44.1	339.5	274.7	1700	0.5, 0.8, 1	-	10.0	-	8.5	112°, 129°	-100°, -68°
	Crevasse Splay	Fan	6.7	40.1	231.1	198.7	843.3	0.8, 1, 1.2	1.4	2.7	7.7	-	-100°, 129°	-
3	Fluvial Bar	Crescent	40.7	44.1	339.5	274.7	1700	0.5, 0.8, 1	-	13.1	-	13.6	112°, 129°	-100°, -68°
	Crevasse Splay	Fan	7.4	40.1	231.1	198.7	843.3	0.8, 1, 1.2	1.7	2.9	10.2	-	-100°, 129°	-
4	Fluvial Bar	Crescent	47.8	44.1	339.5	274.7	1700	0.5, 0.8, 1	-	12.6	-	11.4	112°, 129°	-100°, -68°
	Crevasse Splay	Fan	7.5	40.1	231.1	198.7	843.3	0.8, 1, 1.2	1.7	2.7	6.9	-	-100°, 129°	-
5	Fluvial Bar	Crescent	45.4	44.1	339.5	274.7	1700	0.5, 0.8, 1	-	13.3	-	8.2	112°, 129°	-100°, -68°
	Crevasse Splay	Fan	8.8	40.1	231.1	198.7	843.3	0.8, 1, 1.2	1.4	3.8	9.5	-	-100°, 129°	-
6	Fluvial Bar	Crescent	15.2	44.1	339.5	274.7	1700	0.5, 0.8, 1	-	10.1	-	7.0	112°, 129°	-100°, -68°
	Crevasse Splay	Fan	12.4	40.1	231.1	198.7	843.3	0.8, 1, 1.2	1.3	3.0	10.2	-	-100°, 129°	-

Table 3. Object-based modeling (OBM) inputs for training image construction. Two scenarios were constructed using a channel shape and the other using a crescent shape for fluvial bars. Training images were created for each zone, totaling 12 images, to be used in MPS modeling. Width data from Pranter et al. (2009).

mathematical operation behind MPS and was developed by Strebelle (2000) to alleviate the computational requirements of the original algorithm proposed by Guardiano and Srivastava (1993). A basic summary of the steps is reviewed in this paper, but a more detailed description can be found in Strebelle (2002, 2006). First, a "search mask" is defined and used to scan the training image to identify repeating patterns in the image for which the probability of occurrence for the patterns is determined and stored in a "search tree". Next, hard data (i.e., from well logs) are assigned to the closest grid cells (the wellbore upscaled). Each unsampled cell is then visited in a certain order only one time. The probability of a particular geologic property occurring within each cell is evaluated for the pattern that exists based on the surrounding hard data, previously simulated cells, and the search tree. Finally, based on the probabilities, a property value is determined and assigned to each empty cell. The next unsampled cell is visited and the process continues until all cells have been assigned a value.

The appropriate search mask size and parameters were systematically tested using unconditioned models to best reproduce training images. The search mask used an ellipsoid shape with a defined cell radius in the I-, J-, and K-directions (i.e., x-, y-, and z-vectors) to capture the probability of particular patterns occurring within the training image. If the search mask is too small, the larger features in output models might appear discontinuous. If the search mask is too large, a better simulation might be expected, but longer computational times will be required (Caers and Zhang, 2004; Strebelle, 2006). Search mask parameters were systematically defined by varying search mask cell radius in the I-, J-, and K-directions, as well as number of multi-grids and maximum number of informed nodes to create multi-point facies patterns for a number of different training image sizes and facies proportions. A multi-grid is the coarsest grid used to capture large-scale heterogeneity patterns within the training image. The coarsest grid is populated

first, followed by the finer sub-grids until all unknown cells are assigned a value (Strebelle, 2002). The number of informed nodes refers to how many defined nodes are present within the sub-grids. The number of multi-grids and maximum number of informed nodes is dependent on the amount of detail the user prefers and computational time restraints. Unconditioned MPS output models were generated and visually inspected to evaluate reproducibility with respect to the original training image. Results from training image testing can be found in Appendix C. The final search mask used in the MPS process had a search mask radius of 40 x 30 x 8 cells, 2 multi-grids, and a maximum of 64 informed nodes.

Fluvial Architectural-Element Models

Modeling constraints for the multi-point simulations include both hard and soft data. Manually interpreted architectural-element logs served as hard data for the types of fluvial deposits intersected by each well in the model area. A lithology probability volume was used as a soft constraint, in place of vertical proportion curves, for the placement of sandstone architectural elements (fluvial bars and crevasse splays) stratigraphically and laterally within the model framework. The lithology probability volume was constructed from a sequential-indicator simulation model of lithology using a spherical variogram with a minor range of 3000 ft (900 m), a major range of 3000 ft (900 m), and vertical range of 10 ft (3 m). Major and minor ranges were subjectively chosen to be approximately one-half the width of the model area. The lithology model was then converted to a probability template and used during the modeling process as a soft constraint. Probability values for sandstone lithology (probability = 0.7) and all other lithologies (probability = 0.1) were arbitrarily chosen in order to preferentially place sandstone architectural elements within cells that were more likely to be assigned a “sandstone” value. Training images

were paired with their respective zone for each scenario during the MPS modeling process (Figure 11). However, because the training images did not include coal, a kriged model for coal was generated separately and deterministically merged into the MPS models.

The architectural-element models for each scenario were quantitatively evaluated in terms of architectural-element proportions and net-to-gross ratio relative to the global proportions in the upscaled logs. The upscaled architectural-element logs were 34.6% fluvial bars, 7.5% crevasse splays, 55.3% floodplain, and 2.7% coal with a net-to-gross ratio of 42.1% (Table 4). The sinuous channel model produced 33.0% fluvial bars, 13.2% crevasse splays, 51.5% floodplain, and 2.4% coal with a net-to-gross ratio of 46.2%, while the crescent-shaped fluvial bar model produced 32.4% fluvial bars, 12.7% crevasse splays, 52.6% floodplain, and 2.4% coal, with a net-to-gross ratio of 45.0% (Figure 12, Table 4). Overall, both scenarios produced global architectural-element proportions similar to the upscaled log proportions (within 6.0%). However, when the proportion of crevasse splays in the models is compared to the proportions in the upscaled architectural-element logs, both models overpopulate crevasse splays relative to the upscaled logs for the sinuous channel scenario and crescent-shape scenario, respectively (i.e., 7.5% in the upscaled logs, 13.2% and 12.7% in the models; Figure 12D). One explanation might be that coal was omitted from the training images, but still existed in the upscaled logs as hard data. Therefore, when coal was deterministically placed into the final models after the MPS process, it may have allowed coal to replace more fluvial bar and floodplain elements, causing the overall proportion for crevasse splays to increase. Fluvial bars are slightly underestimated in each zone (with the exception of Zone 3) and net-to-gross ratio is overestimated in each zone, but each parameter is still within 6.5% or less of the proportions in the upscaled logs.

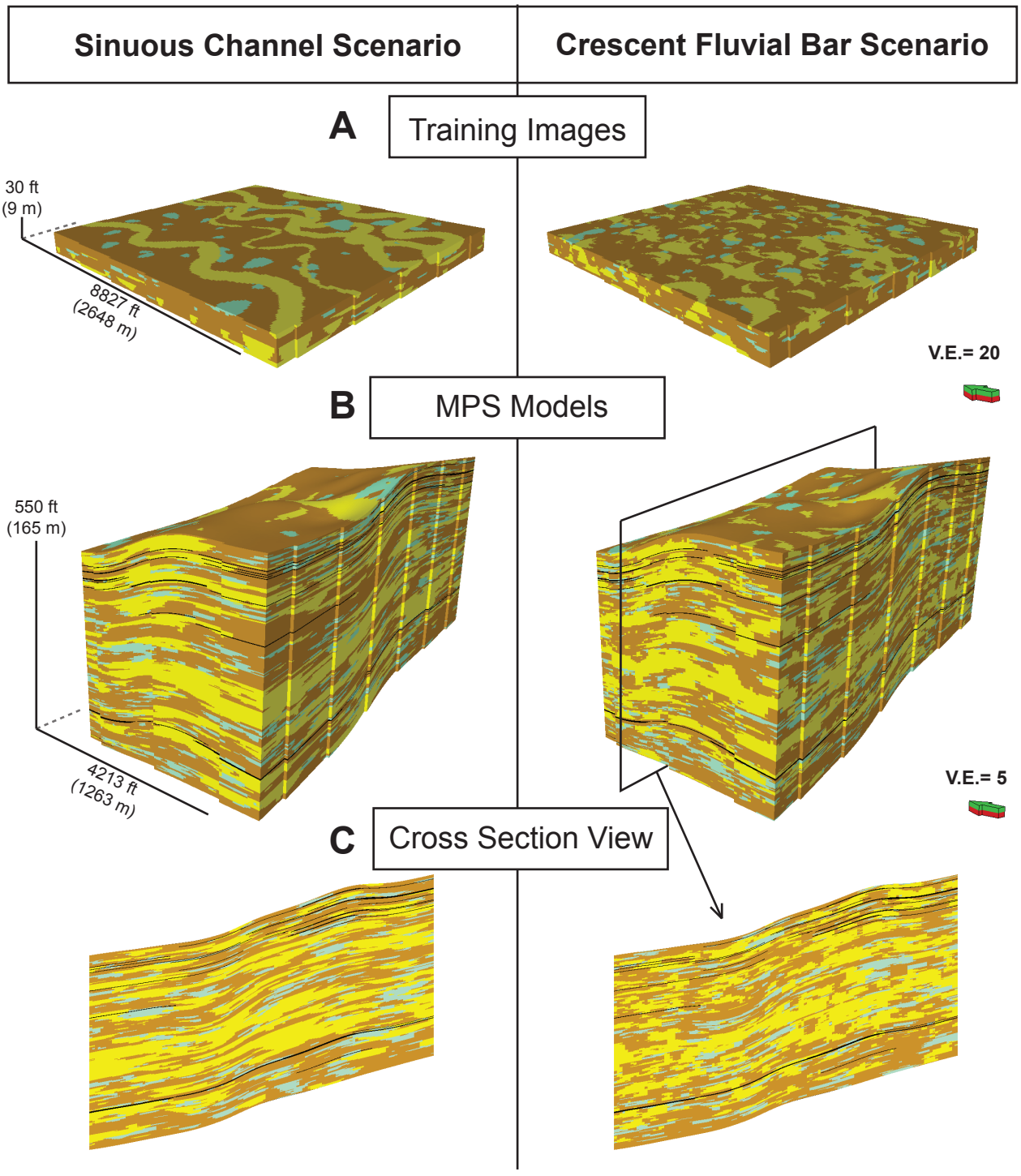

Figure 11. Training images (A), MPS volumes (B), and a cross sectional view (C) for each of the two end member scenarios: sinuous channel scenario and crescent fluvial bar scenario. Separate training images for each scenario were used for each zone (totaling 12 training images: pictured is an example from Zone 1). Box shown around MPS model in (B) shows the slice from which the cross section is taken (viewed from the south).

Zone	Architectural Element/Net-to-Gross	Model Proportions (%)		
		Upscaled Logs	Sinuous Channel Scenario	Crescent-shaped Fluvial Bar Scenario
Entire Model	Floodplain	55.3	51.5	52.6
	Fluvial Bars	34.6	33.0	32.4
	Crevasse Splays	7.5	13.2	12.7
	Coal	2.7	2.4	2.4
	Net-to-Gross	42.1	46.2	45.0
1	Floodplain	57.6	53.4	55.0
	Fluvial Bars	30.0	29.2	28.1
	Crevasse Splays	5.3	10.9	10.4
	Coal	7.1	6.5	6.5
	Net-to-Gross	35.3	40.1	38.5
2	Floodplain	60.2	55.0	55.3
	Fluvial Bars	32.8	31.8	32.4
	Crevasse Splays	6.7	13.0	12.1
	Coal	0.3	0.3	0.3
	Net-to-Gross	39.5	44.8	44.5
3	Floodplain	51.9	45.7	47.8
	Fluvial Bars	40.7	41.4	40.1
	Crevasse Splays	7.4	12.9	12.2
	Coal	0.0	0.0	0.0
	Net-to-Gross	48.1	54.3	52.2
4	Floodplain	44.7	42.8	44.1
	Fluvial Bars	47.8	45.1	44.0
	Crevasse Splays	7.5	12.1	11.9
	Coal	0.0	0.0	0.0
	Net-to-Gross	55.3	57.2	55.9
5	Floodplain	38.7	39.9	40.8
	Fluvial Bars	45.4	41.1	40.5
	Crevasse Splays	8.8	13.0	12.7
	Coal	7.0	6.1	6.1
	Net-to-Gross	54.2	54.1	53.2
6	Floodplain	71.3	66.0	66.0
	Fluvial Bars	15.2	14.6	14.7
	Crevasse Splays	12.4	18.5	18.4
	Coal	1.0	0.9	0.9
	Net-to-Gross	27.7	33.1	33.1

Table 4. Net-to-gross and architectural-element proportions in the upscaled logs, MPS sinuous channel model, and MPS crescent-shaped fluvial bar model.

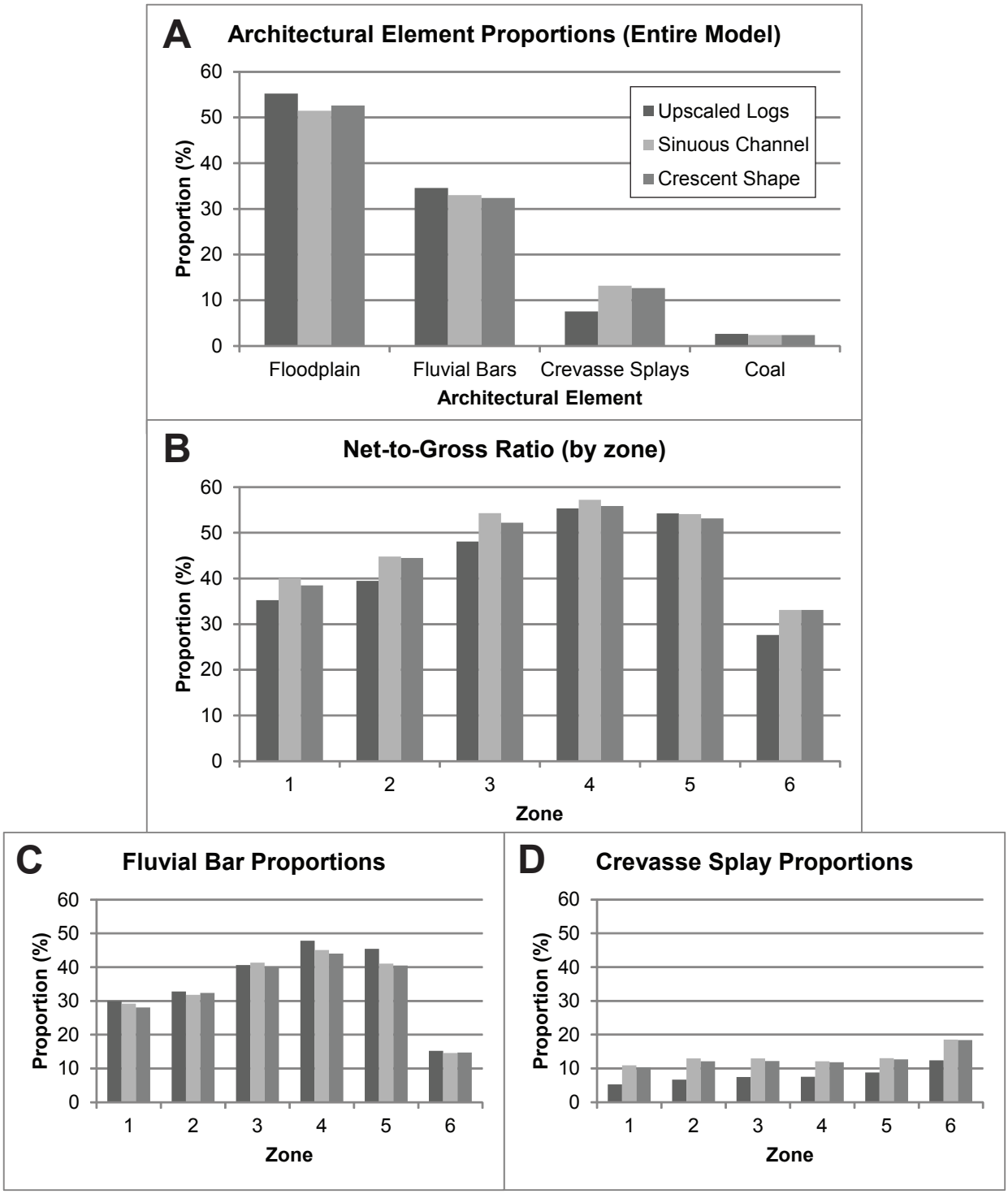

Figure 12. A: Proportions of each architectural element in the upscaled logs, sinuous channel MPS model, and crescent shaped fluvial bar MPS model. B: Net-to-gross ratio by zone for the upscaled logs and each of the two MPS scenarios. Both fluvial bars and crevasse splays contribute to net-to-gross calculations. C: Fluvial bar proportions by zone. D: Crevasse splay proportions by zone in the upscaled logs and each of the two MPS scenarios.

STATIC CONNECTIVITY OF FLUVIAL DEPOSITS AT RED WASH FIELD

Reservoir connectivity is one of the most important parameters to understand when making recovery estimates and developing a field, yet it often comes with a great amount of uncertainty. To address this uncertainty, previous work has focused on defining the relationship between depositional properties (i.e., net-to-gross ratio, sandstone-body geometry, and sandstone-body spatial distribution) and the connectedness of a reservoir (Allen, 1978; King, 1990; Allard and HERESIM-Group, 1993; Ainsworth, 2005; Larue and Hovadik, 2006; Hovadik and Larue, 2007; Sommer, 2007; Pranter and Sommer, 2011). Allen (1978) and King (1990) both concluded that connectivity in two dimensions rapidly increases when a certain net-to-gross ratio is reached. King (1990) defined this as the "percolation threshold", where connectivity is very low below this net-to-gross threshold, but then quickly approaches 100% once exceeded. Larue and Hovadik (2006) later confirmed this relationship, which became known as the "S-curve", due to the graphical appearance of connectivity versus net-to-gross (Sommer, 2007; Pranter and Sommer, 2011). Connectivity is improved by the presence of sandstone-rich overbank deposits, high sandstone-body width-to-thickness ratio, and variable floodplain aggradation rates, while factors that reduce connectivity include parallelism of channels (low sinuosity), compartmentalization by laterally continuous impermeable mudstone units, and vertical stratification due to flooding and abandonment surfaces (Larue and Hovadik, 2006). Under the percolation theory, it was also demonstrated that higher connectivity values would be expected at more modest net-to-gross ratios in three dimensions when compared to two-dimensional connectivity (King, 1990; Hovadik and Larue, 2007). Therefore, to accurately examine connectivity in the subsurface, it is essential to model fluvial sandstone bodies in 3-D to preserve the depositional trends that have direct implications for reservoir connectedness.

Many authors have defined connectivity to best suit their specific research motivation. This study investigates well-based static connectivity, which is herein defined as the percentage calculated by dividing the volume of sandstone connected to a particular pattern of wells by the total sandstone volume (Larue and Hovadik, 2006; Pranter and Sommer, 2011). This definition assumes that face-to-face contacts of sandstone cells in the model will allow fluids to flow within the reservoir so that sandstone may be connected both directly and indirectly to a wellbore (i.e., through amalgamation. Static sandstone connectivity was analyzed within the two MPS models on the current well spacing and four hypothetical scenarios (Figure 13), where pseudo wells were "drilled" (included) in the model domain to approximate well spacings at 160-ac, 40-ac, 10-ac, and 2.5-ac (distances between wells: 2640 ft [805 m], 1320 ft [402 m], 660 ft [201 m], and 330 ft [100 m], respectively). The goal of this portion of the study was to examine how static connectivity varies as a function of well density, sandstone-body type, and net-to-gross ratio.

"Reservoir-Quality" Sandstone vs. Total Sandstone

In addition to total sandstone connectivity, these analyses included a measure of connectivity for "reservoir-quality" sandstone, where a porosity cutoff was applied to account for internal porosity heterogeneity within fluvial sandstone bodies that is not accounted for in the architectural-element models. Factors that affect flow properties within a reservoir, such as size, sorting, and angularity of grains and occlusion of pore throats by diagenetic cements, can cause porosity and permeability to vary spatially. Because fluvial sandstones of the Mesaverde Group are considered to be "tight" (low-permeability), looking at "reservoir-quality" sandstone based on this porosity criterion might provide a more realistic measure of connected sandstone that is expected to have better flow properties.

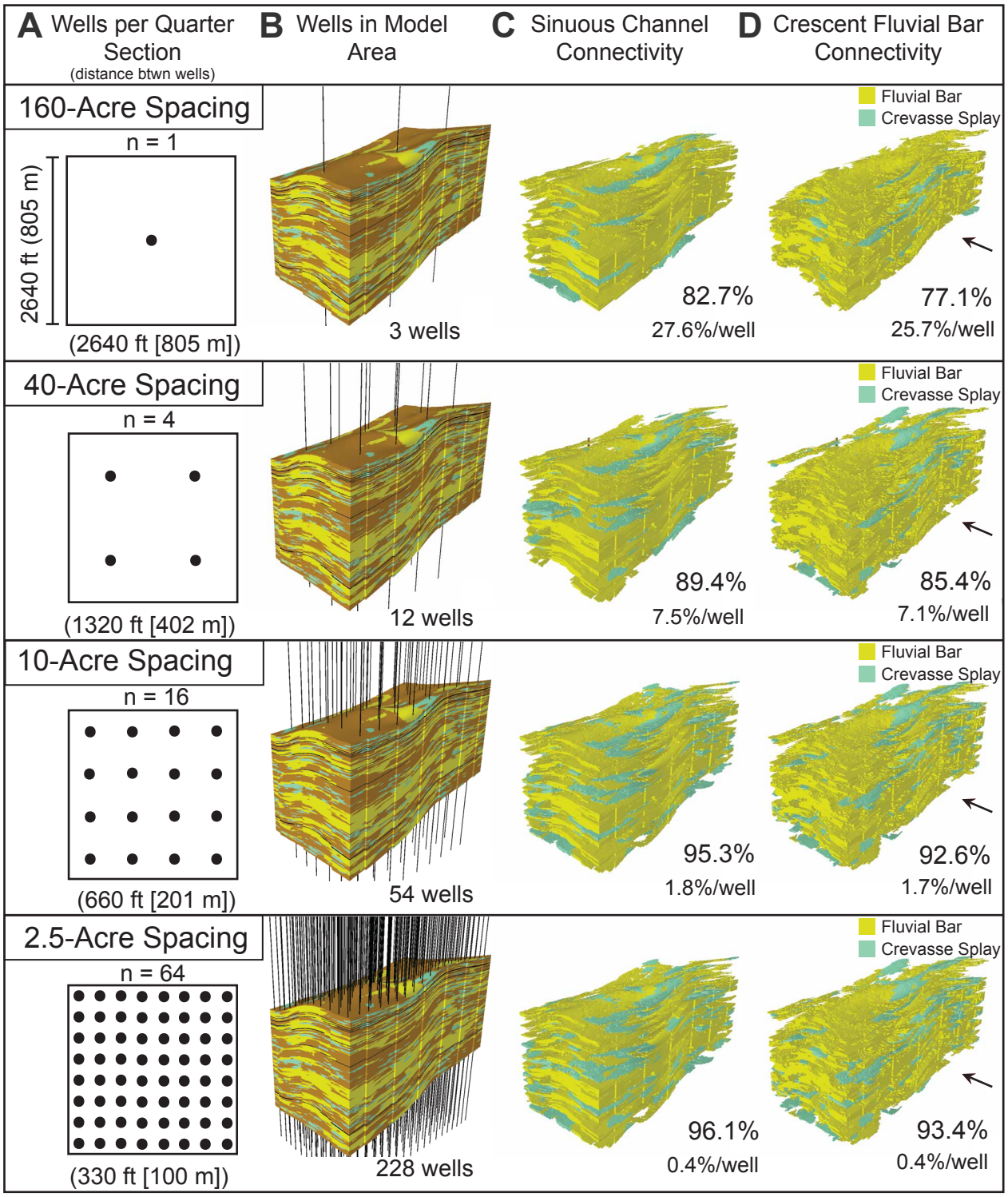

Figure 13. Diagram illustrating (A) well spacing patterns and distance between wells in a quarter section (2640 ft x 2640 ft [805 m x 805 m], (B) pseudo wells "drilled" in model area to approximate the respective well spacing pattern, (C) connected sandstone volume for the sinuous channel MPS model, and (D) connected sandstone volume for the crescent-shaped fluvial bar MPS model for each respective well spacing pattern. Vertical exaggeration = 5x for all 3-D volumes.

Total porosity (PHIT) logs for the 10 wells in the model area were calculated using the following root mean squared equation with neutron (NPHI) and density porosity (DPHI):

$$PHIT = \sqrt{\frac{NPHI^2 + DPHI^2}{2}}$$

Total porosity was then modeled for all zones simultaneously with sequential Gaussian simulation using a spherical variogram with a major range of 2000 ft (600 m), minor range of 2000 ft (600 m), and a vertical range of 4 ft (1.2 m). Major and minor ranges were arbitrarily chosen to be less than the variogram ranges selected for sandstone in the SIS lithology model. To distinguish between "reservoir-quality" sandstone, a porosity cutoff was derived using a cross-plot of confined porosity (net confining stress = 2550 psi) and Klinkenberg permeability measurements obtained from core plugs (from RW 12D4-25B, Appendix D). Porosity values between 6.0% and 15% were chosen because they best corresponded with permeability values greater than 0.001 md. During the connectivity analyses, a filter was applied to the architectural-element models so that they only incorporated sandstone with porosity values between 6.0% and 15%. Although this method is unlikely to account for all internal heterogeneities that hinder fluid flow and storage within fluvial sandstone bodies, it does allow a comparison of total sandstone connectivity to "reservoir-quality" sandstone connectivity.

Static Sandstone Connectivity Analysis

Static connectivity analysis was conducted on the sinuous channel model and the crescent-shaped fluvial bar model. Connectivity values for both "reservoir-quality" sandstone and total sandstone was reported for each model, zone, and well-spacing scenario in Table D1 – D3 of Appendix D. Fluvial-bar connectivity was reported as a separate value in order to determine the

effect of crevasse splays. For the entire model volume, total sandstone connectivity ranged from 82.7% at the lowest well density to 96.1% at the highest well density in the sinuous channel MPS model, and from 77.1% to 93.4% in the crescent-shaped fluvial bar model. "Reservoir-quality" sandstone connectivity ranged from 56.1% to 68.8% in the sinuous channel model, and from 53.6% to 66.4% in the crescent-shaped fluvial bar model (Figure 14).

There is a maximum connectivity difference of 6.0% between the sinuous-channel and crescent-shaped fluvial bar architectural-element models, with the sinuous-channel model exhibiting the slightly higher connectivity values. Although it may not be a striking difference, it was expected that using a channel shape in the training images would produce more connected sandstone bodies, while using a crescent-shape would create more discrete, isolated sandstone bodies. One reason the two architectural-element models do not display a large difference might be that the net-to-gross ratio is approaching the percolation threshold, where connectivity is expected to be high regardless of well spacing and sandstone-body geometry. However, there was a significant average decrease of 26.1% in connectivity when accounting for the porosity cutoff in the "reservoir-quality" sandstone (Figure 15A), causing connectivity to be uniformly lower in each well spacing scenario, regardless of which architectural-element model was evaluated.

These results also show that while it might be intuitive that well-based static connectivity would increase with well density, on a per well basis, static connectivity decreases for both scenarios and sandstone types (Figure 15B) as well spacing increases. Consequently, the increase in connectivity due to adding more wells was not substantial enough to maintain or increase the connectivity per well, which may have implications for field development.

All previous analysis included both fluvial bars and crevasse splays as contributors to static sandstone connectivity. The impact of sandstone-body type was considered by comparing the static

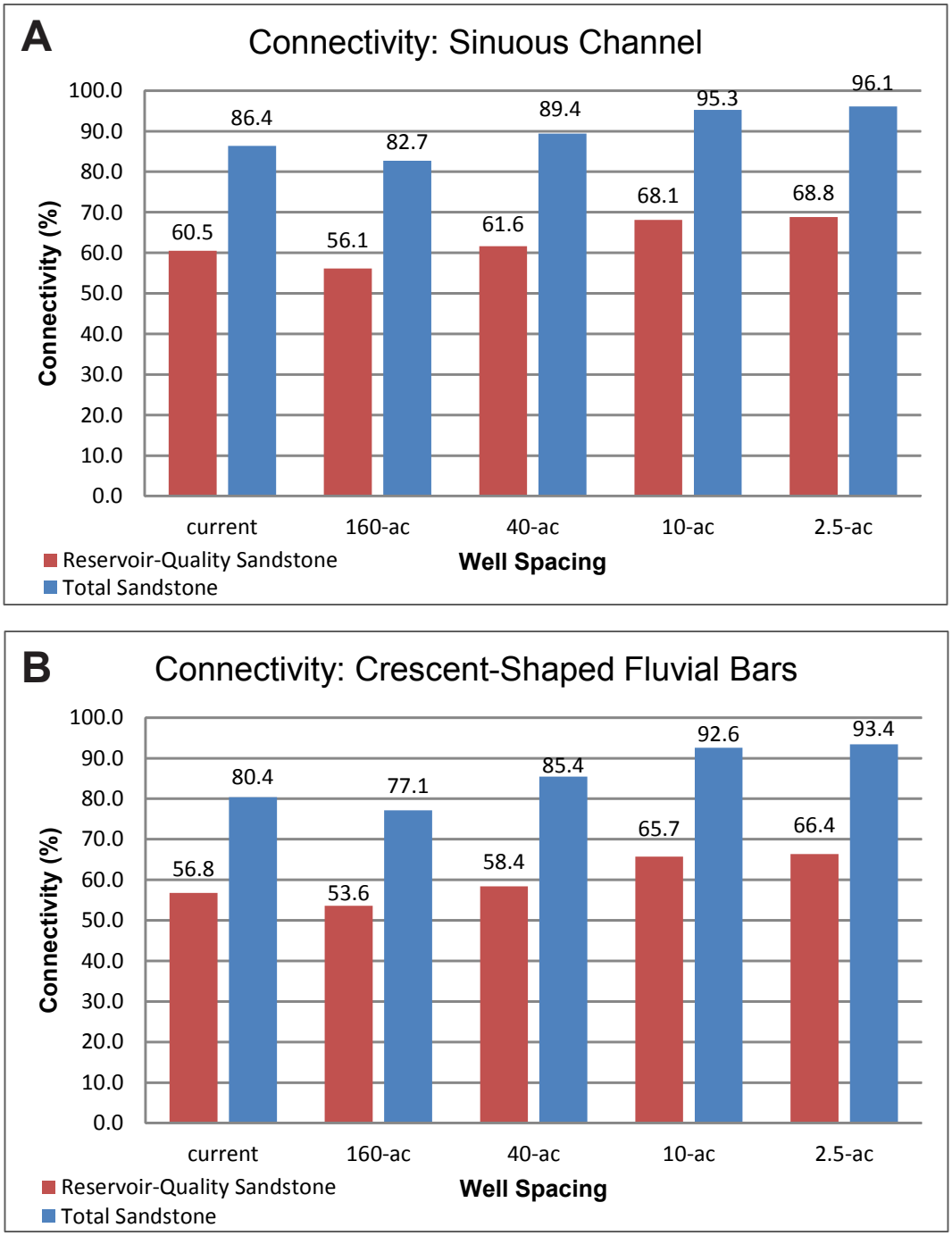

Figure 14. Histograms depicting three-dimensional static sandstone connectivity for total sandstone (shown in blue) and "reservoir-quality" sandstone (porosity between 6 - 15%, shown in red) for (A) the sinuous channel MPS model and (B) the crescent-shaped fluvial bar MPS model. Values reflect connectivity for the entire volume of the model. There is an average 26.1% decrease in connectivity when accounting for "reservoir-quality" sandstone. The maximum difference in connectivity between the two modeling scenarios is 6.0%.

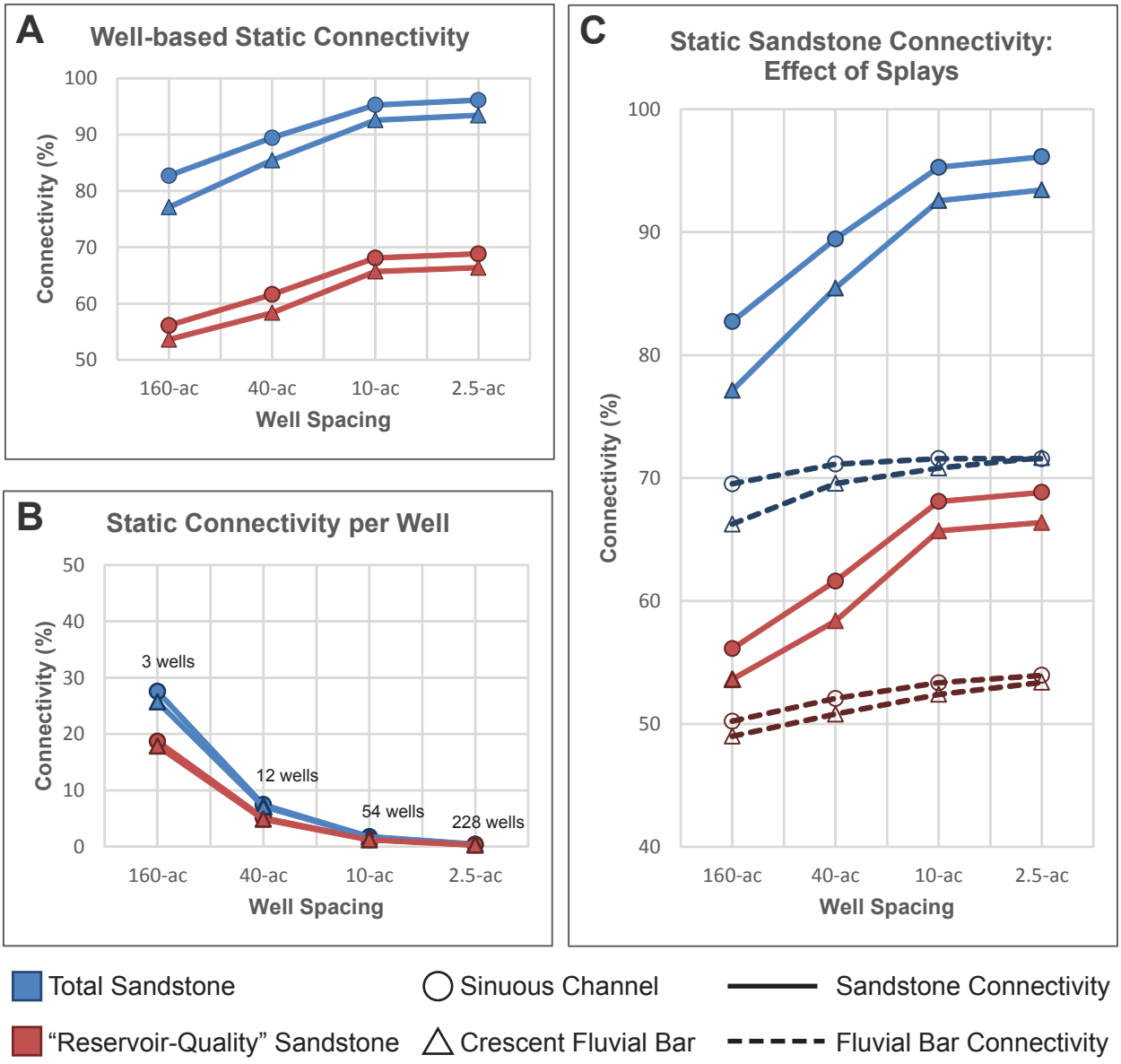

Figure 15. Graphs depicting (A) well-based static sandstone connectivity, (B) static sandstone connectivity per well, and (C) sandstone connectivity (fluvial bars and crevasse splays) with connectivity based solely on fluvial bars ("FB-connectivity") for each MPS scenario. A: Well-based static connectivity increases with well spacing for both total sandstone and "reservoir-quality" sandstone. B: On a per well basis, static connectivity rapidly decreases for both scenarios and sandstone types as well spacing decreases. C: Solid lines depict sandstone connectivity, which include fluvial bars and crevasse splays, and dotted lines include only the connected sandstone volumes attributed to fluvial bars (FB-connectivity), while omitting crevasse splays. With increasing well density, a larger portion of the sandstone connectivity is due to more wells penetrating crevasse splays.

connectivity of both fluvial bars and crevasse splays, with the static connectivity attributed exclusively to fluvial bars, herein referred to as FB-connectivity (Figure 15C). With increasing well density, sandstone connectivity increased, while FB-connectivity remained relatively constant, indicating that a larger portion of the total connectivity increase was attributed to the presence of crevasse splays. Therefore, discrete crevasse splays, which would otherwise be isolated from larger sandstone bodies and disconnected from wellbores at low densities, were progressively penetrated as well density increased. This agrees with the expectation of Larue and Hovadik (2006) that lateral sandy overbank deposits can augment communication between channel sands, and thus should not be disregarded in terms of reservoir potential (Anderson, 2005; Sommer, 2007; Hewlett, 2010; Pranter and Sommer, 2011; Sloan, 2012; Pranter et al., 2014).

When considering stratigraphic changes by zone, it was found that there is a distinct variation in connectivity depending on well density and net-to-gross ratio (Figure 16, Table 5). For higher well densities (i.e., 2.5-ac spacing [100 m]), connectivity did not fluctuate much stratigraphically with regards to net-to-gross ratio. The amount of sandstone-body connectivity remained high (above 87.8%) in both architectural-element models, regardless of net-to-gross ratio or sandstone type (i.e., "reservoir-quality" and total sandstone). However, at lower well densities (i.e., 160-ac spacing [805 m]), connectivity was highly variable stratigraphically. For example, at 160-ac spacing (805 m) for "reservoir-quality" sandstone, connectivity ranged within zones from 19.6% to 87.1% ($\sigma^2 = 571.2$) for the sinuous-channel model and from 6.0% to 84.4% ($\sigma^2 = 761.2$) in the crescent-shaped fluvial bar model. These ranges are much broader than the 2.5-ac spacing (100 m) scenario, where "reservoir-quality" connectivity within zones ranged from 93.1% to 98.8% ($\sigma^2 = 5.7$) for the sinuous-channel model and from 87.8% to 97.7% ($\sigma^2 = 13.2$) for the crescent-shaped fluvial bar model.

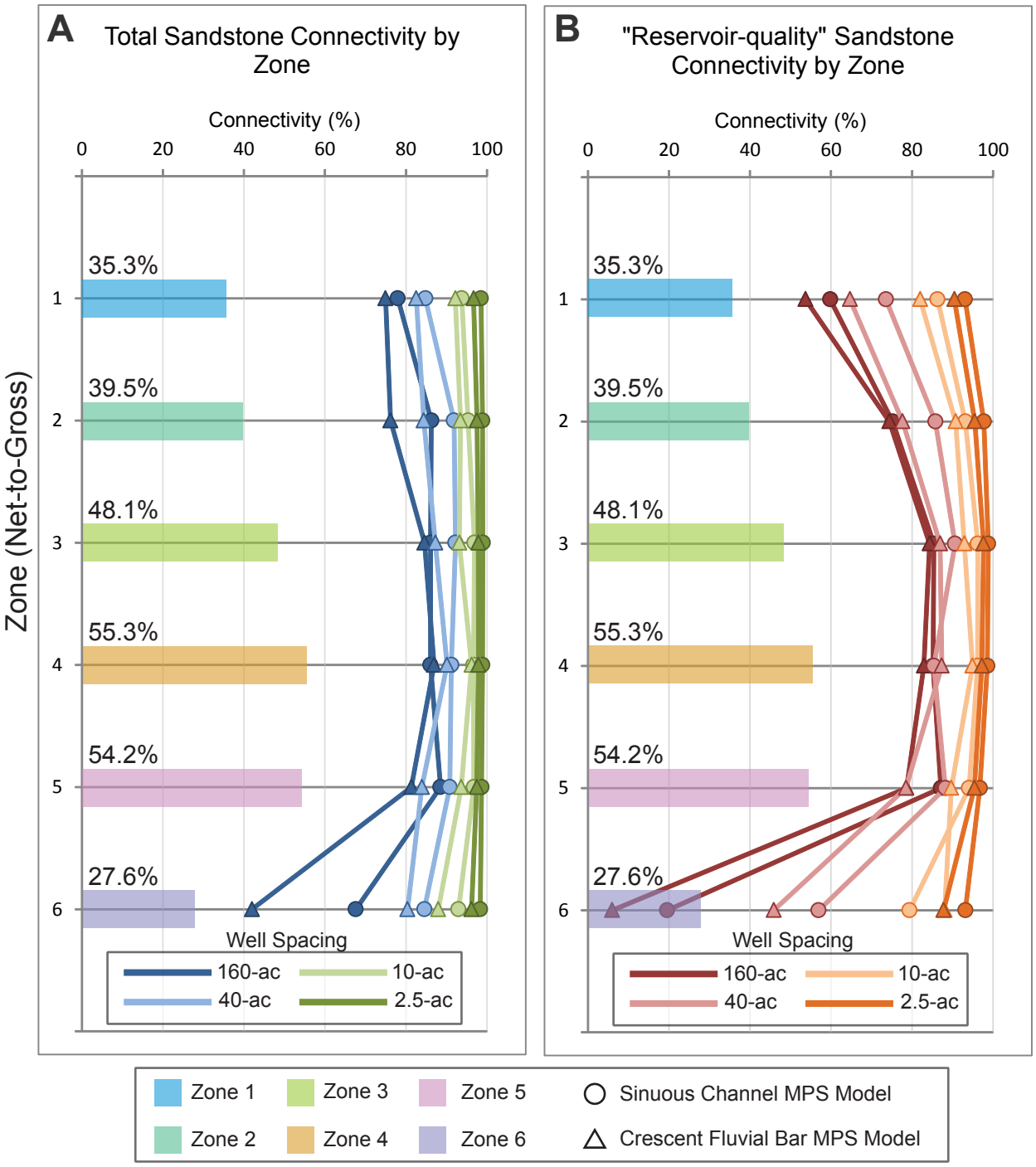

Figure 16. Static connectivity plotted with zone net-to-gross ratio from upscaled logs for (A) total sandstone and (B) "reservoir-quality" sandstone. For higher well density (i.e., 2.5-ac spacing), connectivity does not vary much stratigraphically. At low well densities (i.e., 160-ac spacing), connectivity is highly variable stratigraphically depending on net-to-gross ratio. This relationship is more prominent in the "reservoir-quality" sandstone connectivity.

Static Connectivity by Zone Statistics: Sinuous Channel MPS Model										
Well Spacing	"Reservoir-Quality" Connectivity (%)					Total Connectivity (%)				
	Min	Mean	Max	Var (σ^2)	std (σ)	Min	Mean	Max	Var (σ^2)	std (σ)
160-ac	19.6	68.7	87.1	571.2	23.9	67.6	82.1	88.5	52.9	7.3
40-ac	56.9	80.1	90.6	136.1	11.7	84.5	89.2	92.2	10.7	3.3
10-ac	79.4	90.9	96.2	37.5	6.1	93.0	95.4	96.9	2.4	1.5
2.5-ac	93.1	96.4	98.8	5.7	2.4	98.3	98.7	99.0	0.1	0.2

Static Connectivity by Zone Statistics: Crescent-Shaped Fluvial Bar MPS Model										
Well Spacing	"Reservoir-Quality" Connectivity (%)					Total Connectivity (%)				
	Min	Mean	Max	Var (σ^2)	std (σ)	Min	Mean	Max	Var (σ^2)	std (σ)
160-ac	6.0	63.3	84.4	761.2	27.6	42.0	74.3	86.9	227.1	15.1
40-ac	45.9	73.5	87.4	209.4	14.5	80.4	84.8	90.1	10.0	3.2
10-ac	82.0	89.7	94.9	16.8	4.1	88.0	92.8	96.2	6.1	2.5
2.5-ac	87.8	94.0	97.7	13.2	3.6	96.2	97.3	97.9	0.4	0.6

Table 5. Statistics for zone static connectivity by well spacing pattern for both MPS architectural-element models. Each statistic is based on connectivity values for 6 zones in the model framework. It should be noted that sample size is statistically small (n = 6) and thus not necessarily representative of the population distribution. However, it is appropriate to refer to these as sample statistics, where the sample mean and variance are considered biased estimators of the population mean (μ) and variance (σ^2).

As expected, the zones exhibiting the lowest net-to-gross ratios experienced the greatest connectivity increase when raising well density from 160-ac to 2.5-ac (805 m to 100 m) spacing. For instance, Zone 6 had the lowest net-to-gross ratio (27.6% from the upscaled logs), but the connectivity increased by as much as 81.8% from 160-ac to 2.5-ac spacing. Conversely, Zone 4, which has the highest net-to-gross ratio (55.3%), only experienced a maximum connectivity increase of 14.4%. In other words, at low well densities, connectivity is low at lower net-to-gross ratios, and increases between 30 and 40% (Figure 17). Above 40% net-to-gross, the connectivity levels off, and is only improved by about 10 – 15% when raising well density to 2.5-ac (100 m) spacing, whereas the intervals below 40% net-to-gross experienced a more pronounced spread of connectivity values. This variability in connectivity agrees with the findings of Pranter and Sommer (2011), where the S-curve relationship between connectivity and net-to-gross is most pronounced at 160-ac well spacing and becomes more linear as well density increases (Appendix D, Figure D3). Therefore, at high well densities, little variability in connectivity would be expected regardless of net-to-gross ratio. Finally, there are notably larger variances associated with the "reservoir-quality" connectivity (σ^2 = 5.7 – 761.2) when compared to the variances of the total sandstone connectivity values (σ^2 = 0.2 – 15.1) per zone. This further suggests that connectivity is more sensitive to parameters such as stratigraphic variability in net-to-gross and well spacing when accounting for petrophysical constraints.

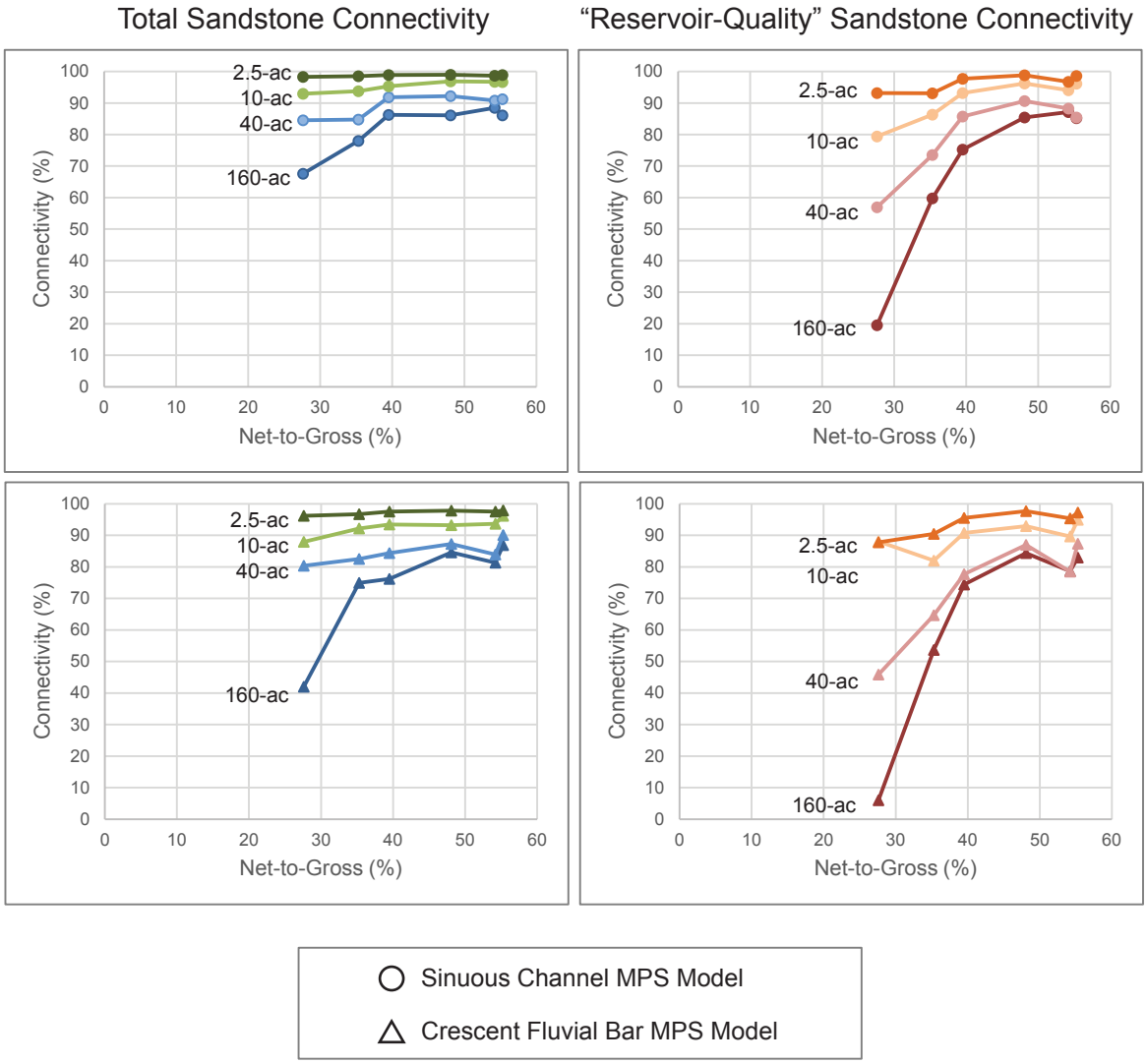

Figure 17. Graphs of total sandstone connectivity and "reservoir-quality" sandstone connectivity versus net-to-gross ratio of both architectural-element MPS modeling scenarios. At low well densities (e.g., 160-ac spacing), connectivity is low at lower net-to-gross ratios, and increases between 30 and 40%. Above 40% net-to-gross, connectivity values level off. This observation is consistent with the S-curve relationship between connectivity and net-to-gross ratio at low well densities reported by Sommer (2007) and Pranter and Sommer (2011).

CONCLUSIONS

The lower Mesaverde Group at Red Wash Field is characterized by sandstones, carbonaceous mudrock, and coals deposited during the Late Cretaceous in low-energy, fluvial settings within a lower coastal-plain environment. Four main architectural elements interpreted from core include sandstone fluvial bars, shaley sandstone crevasse splays, mudstone-rich floodplain deposits, and coal. In contrast to cored intervals, fluvial deposits in outcrop are characterized by an abundance of lower-flow-regime sedimentary structures, thinner sandstones, and thicker fine-grained floodplain successions, suggesting the outcrop may have been closer to the paleoshoreline or more distal from the main channel belt relative to the contemporaneous subsurface deposits. This trend reflects an overall decrease in energy toward the northwest, where the subsurface deposits were located on the periphery of the main channel-belt axis, while the outcrop deposits were subjected to more extensive brackish-water influence closer to the paleoshoreline.

Static connectivity analyses of the MPS architectural-element models revealed how static connectivity varies as a function of well density, sandstone-body type, and net-to-gross ratio. Overall, the sinuous-channel scenario produced higher connectivity values, but only by a maximum of 6.0% more than the crescent-shaped fluvial bar scenario. Connectivity increases as well density increased, but decreases on a per well basis for both models.

It was demonstrated in this study that crevasse splays enhance connectivity at all well spacings. Crevasse splays, that would have otherwise been isolated from larger sandstone bodies at 160-ac (805 m) spacing, were progressively penetrated by wellbores as well density increased. It is uncertain whether or not the crevasse splays would be of adequate reservoir quality to be producible units themselves. Nevertheless, it is shown that crevasse splays can enhance

communication between larger channel elements and should therefore be considered potentially important for reservoir performance.

As expected, there is little variability in connectivity regardless of net-to-gross ratio at high well densities (i.e., 2.5-ac [100 m] spacing). However, connectivity is highly variable at low well densities (i.e., 160-ac [805 m] spacing) as net-to-gross varied stratigraphically. For intervals below 40% net-to-gross, connectivity increases as a result of increasing well density, while connectivity only improved by about 10 – 15% for intervals above 40% net-to-gross when increasing to 2.5-ac (100 m) spacing. Thus, it is recommended that the infill drilling program be adjusted on a case-by-case basis depending on the predicted net-to-gross of the targeted interval. High reservoir connectivity can theoretically be accomplished with 160-ac spacing for intervals above 40% net-to-gross, but well density should be increased to add reserves and enhance reservoir connectivity from lower net-to-gross intervals. However, the connectivity analyses presented in this study assumes that all sandstone-on-sandstone contacts permit unrestricted hydrocarbon migration regardless of the size of the interface and internal heterogeneities within sandstone bodies. Therefore, it should be noted that actual static connectivity values are likely less than the reported values in all cases.

"Reservoir-quality" sandstone connectivity is, on average, 26.1% lower than total sandstone connectivity in each well-spacing scenario and MPS architectural-element model scenario and displays a larger spread of connectivity values at low well densities and net-to-gross ratios. This supports the expectation that connectivity is more sensitive to depositional constraints and well density when accounting for rock quality.

REFERENCES

Ainsworth, R. B., 2005, Sequence stratigraphic-based analysis of reservoir connectivity: influence of depositional architecture – a case study from a marginal marine depositional setting: Petroleum Geoscience, v. 11, p. 257–276.

Allard, D., and HERESIM-Group, 1993, On the connectivity of two random set models; the truncated Gaussian and the Boolean: Quantitative Geology and Geostatistics, v. 5, p. 467–478.

Allen, J. R. L., 1978, Studies in fluviatile sedimentation; an exploratory quantitative model for the architecture of avulsion-controlled alluvial sites: Sedimentary Geology, v. 21, p. 129–147.

Allen, J. R. L., 1983, Studies in fluviatile sedimentation: bars, bar-complexes and sandstone sheets (low-sinuosity braided streams) in the Brownstones (L. Devonian), Welsh Borders: Sedimentary Geology, v. 33, p. 237–293.

Anderson, D. S., 2005, Architecture of crevasse splay and point-bar bodies of the nonmarine Iles Formation north of Rangely, Colorado: Implications for reservoir description: The Mountain Geologist, v. 42, no. 3, p. 109–122.

Bohacs, K., and J. Suter, 1997, Sequence stratigraphic distribution of coaly rocks: fundamental controls and paralic examples: AAPG Bulletin, v. 81, no. 10, p. 1612–1639.

Bridge, J. S., 2006, Fluvial facies models: recent developments, *in* H. W. Posamentier, and R. G. Walker, eds., Facies Models Revisted: Special Publications: Society for Sedimentary Geology 84, p. 85–170.

Bridge, J. S., and R. S. Tye, 2000, Interpreting the dimensions of ancient fluvial channel bars, channels, and channel belts from wireline-logs and cores: AAPG Bulletin, v. 84, no. 8, p. 1205–1228.

Caers, J., and T. Zhang, 2004, Multiple-point geostatistics: A quantitative vehicle for integrating geologic analogs into multiple reservoir models, *in* Integration of outcrop and modern analogs in reservoir modeling: AAPG Memoir 80: p. 383–394.

Chatfield, J., 1972, Case history of Red Wash field, Uintah County, Utah: Case Histories: v. 10, p. 342–353.

Cole, R., 2008, Characterization of fluvial sand bodies in the Neslen and lower Farrer Formations (Upper Cretaceous), Lower Sego Canyon, Utah, *in* M. W. Longman, and C. D. Morgan, eds., Hydrocarbon systems and production in the Uinta Basin, Utah: Rocky Mountain Association of Geologists and Utah Geological Association Publication 37: p. 81–100.

Cole, R., and S. P. Cumella, 2005, Sand-body architecture in the lower Williams Fork Formation (Upper Cretaceous), Coal Canyon, Colorado, with comparison to the Piceance Basin subsurface: The Mountain Geologist, v. 42, no. 3, p. 85–107.

Cole, R. D., and M. J. Pranter, 2010, Stratigraphic architecture and reservoir characteristics of the Mesaverde Group: Application of outcrop-based concepts and statistics to the subsurface, western and northern Piceance Basin, Colorado: Energy and Minerals Applied Research Center, Williams Fork Consortium - Phase V 2010 Sponsor Field Trip and Research Meeting, p. 91.

DeCelles, P. G., 2004, Late Jurassic to Eocene evolution of the Cordilleran thrust belt and foreland basin system, western U.S.A.: American Journal of Science, v. 304, p. 105–168.

DeCelles, P. G., and B. S. Currie, 1996, Long-term sediment accumulation in the Middle Jurassic–early Eocene Cordilleran retroarc foreland-basin system: Geology, v. 24, no. 7, p. 591.

Donselaar, M. E., and I. Overeem, 2008, Connectivity of fluvial point-bar deposits: An example from the Miocene Huesca fluvial fan, Ebro Basin, Spain: AAPG Bulletin, v. 92, no. 9, p. 1109–1129.

Ellison, A., 2004, Numerical modeling of heterogeneity within a fluvial point-bar deposit using outcrop and Lidar data: Williams Fork Formation, Piceance Basin, Colorado: M.S. Thesis, University of Colorado, p. 249.

Foster, R. M., 2010, Sequence stratigraphy of the Upper Cretaceous middle Williams Fork Formation, Piceance Basin, Northwestern Colorado: Implications for reservoir sandstones: M.S. Thesis, University of Colorado, p. 263.

Franczyk, K. J., J. K. Pitman, and D. J. Nichols, 1990, Sedimentology, mineralogy, palynology, and depositional history of some uppermost Cretaceous and lowermost Tertiary rocks along the Utah Book and Roan cliffs east of the Green River: USGS Bulletin 1787-N, p. 27.

German, Q., 2006, Analysis of fluvial sandstone-body characteristics and architecture in a high net-to-gross system: upper Williams Fork Formation, Plateau Creek Canyon, Piceance Basin, Colorado: M.S. Thesis, University of Colorado, p. 151.

Guardiano, F. B., and R. M. Srivastava, 1993, Multivariate geostatistics - beyond bivariate moments: Quantitative Geology and Geostatistics, v. 5, p. 133–144.

Harding, A., S. Strebelle, M. Levy, J. Thorne, D. Xie, S. Leigh, and R. Preece, 2004, Reservoir facies modelling: new advances in MPS, *in* O Leuangthong and C.V. Deutsch (eds.), Geostatistics Banff: p. 559–568.

Harper, E., 2011, Fluvial architecture of the lower Williams Fork Formation (middle Mesaverde Group), Douglas Creek Arch, Colorado: M.S. Thesis, University of Colorado, p. 210.

Hettinger, R. D., and M. A. Kirschbaum, 2003, Stratigraphy of the Upper Cretaceous Mancos Shale (upper part) and Mesaverde Group in the southern part of the Uinta and Piceance Basins , Utah and Colorado, *in* Petroleum systems and geologic assessment of oil and gas in the Uinta-Piceance Province, Utah and Colorado, USGS Uinta-Piceance Assessment Team: U.S. Geological Survey Digital Data Series DDS-69-B, Version 1.0, p. 25.

Hettinger, R. D., and M. A. Kirschbaum, 2002, Stratigraphy of the Upper Cretaceous Mancos Shale (upper part) and Mesaverde Group in the southern part of the Uinta and Piceance Basins, Utah and Colorado: United States Geological Survey Geologic Investigation Series I-2674, p. 21.

Hewlett, A., 2010, Fluvial architecture and static connectivity of the Williams Fork Formation, Central Mamm Creek Field, Piceance Basin, Colorado: M.S. Thesis, University of Colorado, p. 227.

Hlava, K., 2011, Sequence-stratigraphic controls on reservoir-scale architecture of the middle Mesaverde Group, Douglas Creek Arch, Colorado: M.S. Thesis, University of Colorado, p. 331.

Holbrook, J., 2001, Origin, genetic interrelationships, and stratigraphy over the continuum of fluvial channel-form bounding surfaces: an illustration from middle Cretaceous strata, southeastern Colorado: Sedimentary Geology, v. 144, p. 179–222.

Hovadik, J. M., and D. K. Larue, 2007, Static characterizations of reservoirs: refining the concepts of connectivity and continuity: Petroleum Geoscience, v. 13, no. 3, p. 195–211.

Johnson, R. C., 2003, Depositional framework of the Upper Cretaceous Mancos Shale and the lower part of the Upper Cretaceous Mesaverde Group , western Colorado and eastern Utah, *in* Petroleum systems and geologic assessment of oil and gas in the Uinta-Piceance Province, Utah and Colorado, USGS Uinta-Piceance Assessment Team: U.S. Geological Survey Digital Data Series DDS-69-B, Version 1.0, p. 28.

Kelley, J. M., and J. W. Castle, 1975, Red Wash Field-U.S.A. Uinta Basin, Utah: *in* TR: Stratigraphic traps, p. 231–256.

King, P. R., 1990, The connectivity and conductivity of overlapping sand bodies, *in* A. T. Buller, E. Berg, O. Hjelmeland, J. Kleppe, O. Torsaeter, and J. O. Aasen, eds., North Sea Oil and Gas Reservoirs-II: p. 353–362.

Kirschbaum, M. A., and R. D. Hettinger, 2004, Facies analysis and sequence stratigraphic framework of upper Campanian Strata (Neslen and Mount Garfield Formations, Bluecastle Tongue of the Castlegate Sandstone , and Mancos Shale), eastern Book Cliffs, Colorado and Utah: U.S. Geological Survey, Report DDS-69-G, p. 46.

Larue, D. K., and J. Hovadik, 2006, Connectivity of channelized reservoirs: a modelling approach: Petroleum Geoscience, v. 12, p. 291–308.

Lawton, T. F., 1986, Fluvial systems of the Upper Cretaceous Mesaverde Group and Paleocene North Horn Formation, central Utah: A record of transition from thin-skinned to thick-skinned deformation in the foreland region, *in* J. A. Peterson, ed., Paleotectonics and sedimentation in the Rocky Mountain Region, United States: AAPG Memoir 41: p. 423–442.

Leibovitz, M. B., 2010, Sequence stratigraphy of the Upper Cretaceous upper Williams Fork Formation, Piceance Basin, northwest Colorado, and its contribution to the basin-centered gas accumulation: M.S. Thesis, University of Colorado, p. 170.

Liu, Y., A. Harding, W. Abriel, and S. Strebelle, 2004, Multiple-point simulation integrating wells, three-dimensional seismic data, and geology: AAPG Bulletin, v. 88, no. 7, p. 905–921.

McLaurin, B. T., and R. J. Steel, 2007, Architecture and origin of an amalgamated fluvial sheet sand, lower Castlegate Formation, Book Cliffs, Utah: Sedimentary Geology, v. 197, no. 3-4, p. 291–311.

Mclaurin, B. T., and R. J. Steel, 2000, Fourth-order nonmarine to marine sequences, middle Castlegate Formation, Book Cliffs, Utah: Geology, v. 28, no. 4, p. 359–362.

Miall, A. D., 2006, Reconstructing the architecture and sequence stratigraphy of the preserved fluvial record as a tool for reservoir development: A reality check: AAPG Bulletin, v. 90, no. 7, p. 989–1002.

Miall, A. D., 1996, The geology of fluvial deposits: Sedimentary Facies, Basin Analysis, and Petroleum Geology: New York, Springer, p. 582.

Osmond, J. C., 2003, History of oil and gas exploration in the Uinta Basin, Utah: The Mountain Geologist, v. 40, no. 4, p. 101–110.

Osmond, J. C., 1964, Tectonic history of the Uinta Basin, Utah, *in* Guidebook to the geology and mineral resources of the Uinta Basin: Utah's Hydrocarbon Storehouse: Utah Geological Association, Thirteenth Annual Field Conference, p. 47–58.

Painter, C. S., C. C. York-Sowecke, and B. Carrapa, 2013, Sequence stratigraphy of the Upper Cretaceous Sego Sandstone Member reveals spatio-temporal changes in depositional processes, Northwest Colorado, U.S.A: Journal of Sedimentary Research, v. 83, no. 4, p. 323–338.

Panjaitan, H., 2006, Sand-body dimensions in outcrop and subsurface, Lower Williams Fork Formation, Piceance Basin, Colorado: M.S. Thesis, Colorado School of Mines, p. 187.

Patterson, P. E., R. L. Skelly, and C. R. Jones, 2012, Climatic controls on depositional setting and alluvial architecture, Doba Basin, Chad, *in* O. W. Baganz, Y. Bartov, K. Bohacs, and D.

Nummedal, eds., Lacustrine sandstone reservoir and hydrocarbon systems: AAPG Memoir 95: p. 265–298.

Pranter, M. J., R. D. Cole, H. Panjaitan, and N. K. Sommer, 2009, Sandstone-body dimensions in a lower coastal-plain depositional setting: Lower Williams Fork Formation, Coal Canyon, Piceance Basin, Colorado: AAPG Bulletin, v. 93, no. 10, p. 1379–1401.

Pranter, M. J., A. I. Ellison, R. D. Cole, and P. E. Patterson, 2007, Analysis and modeling of intermediate-scale reservoir heterogeneity based on a fluvial point-bar outcrop analog, Williams Fork Formation, Piceance Basin, Colorado: AAPG Bulletin, v. 91, no. 7, p. 1025–1051.

Pranter, M. J., a. C. Hewlett, R. D. Cole, H. Wang, and J. Gilman, 2014, Fluvial architecture and connectivity of the Williams Fork Formation: use of outcrop analogues for stratigraphic characterization and reservoir modelling: Geological Society, London, Special Publications, v. 387, p. 57–83.

Pranter, M. J., and N. K. Sommer, 2011, Static connectivity of fluvial sandstones in a lower coastal-plain setting: An example from the Upper Cretaceous lower Williams Fork Formation, Piceance Basin, Colorado: AAPG Bulletin, v. 95, no. 6, p. 899–923.

Pranter, M. J., M. F. Vargas, and T. L. Davis, 2008, Characterization and 3D reservoir modelling of fluvial sandstones of the Williams Fork Formation, Rulison Field, Piceance Basin, Colorado, USA: Journal of Geophysics and Engineering, v. 5, no. 2, p. 158–172.

Shaak, R. V., 2010, Stratigraphic architecture of shallow-marine to coastal-plain parasequences: Lower Williams Fork Formation, southeastern Piceance basin, Colorado: M.S. Thesis, University of Colorado, p. 176.

Shepherd, M., 2009, Geostatistical methods, *in* M. Shepherd, ed., Oil field production geology: AAPG Memoir 91: AAPG Special Volumes, p. 159–174.

Shier, D. E., 2004, Well log normalization: methods and guidelines: Petrophysics, v. 45, no. 3, p. 268–280.

Sloan, J., 2012, Stratigraphic architecture and connectivity of a low net-to-gross fluvial system: combining outcrop analogs and multiple-point geostatistical modeling, lower Williams Fork Formation, Piceance Basin, Colorado: M.S. Thesis, University of Colorado, p. 266.

Sommer, N., 2007, Sandstone-body connectivity in a meandering-fluvial system: an example from the Williams Fork Formation, Piceance Basin, Colorado: M.S. Thesis, University of Colorado, p. 193.

Stancel, S. G., J. J. Cuzella, L. Macmillan, and A. Ragas, 2008, Controls on gas production along the southern flank of Greater Natural Buttes Field: a case study of the Love Area, Uinta Basin, Utah, *in* M. W. Longman, and C. D. Morgan, eds., Hydrocarbon Systems and

Production in the Uinta Basin, Utah: Rocky Mountain Association of Geologists and Utah Geological Association Publication 37: p. 237–265.

Strebelle, S., 2002, Conditional simulation of complex geological structures using multiple-point statistics: Mathematical Geology, v. 34, no. 1, p. 1–21.

Strebelle, S. B., 2006, Sequential simulation for modeling geological structures from training images, *in* T. C. Coburn, J. M. Yarus, and R. L. Chambers, eds., Stochastic modeling and geostatistics: Principles, methods, and case studies, volume II: AAPG Computer Applications in Geology 5: AAPG Special Volumes, p. 139–149.

Strebelle, S., and A. Journel, 2001, Reservoir modeling using multiple-point statistics, *in* Proceedings of SPE Annual Technical Conference and Exhibition: Society of Petroleum Engineers, p. 11.

Tyler, R., and R. G. Mcmurry, 1995, Genetic stratigraphy, coal occurrence, and regional cross section of the Williams Fork Formation, Mesaverde Group, Piceance Basin, northwestern Colorado: Colorado Geological Survey Open-File Report 95-2, p. 41.

Van Wagoner, J. C., R. M. Mitchum, K. M. Campion, and V. D. Rahmanian, 1990, Stratigraphy in well logs, cores, and outcrops: concepts for high-resolution correlation of time and facies: AAPG Methods in Exploration Series, no. 7, p. 55.

White, H., R. Cole, S. Stancel, C. Lee, and L. Macmillan, 2008, "Window" outcrop analogs for Greater Natural Buttes Field, Uinta Basin, Utah, *in* M. W. Longman, and C. D. Morgan, eds., Hydrocarbon systems and production in the Uinta Basin, Utah: Rocky Mountain Association of Geologists and Utah Geological Association Publication 37: p. 209–235.

Yoshida, S., A. Willis, and A. D. Miall, 1996, Tectonic control of nested sequence architecture in the Castlegate Sandstone (upper Cretaceous), Book Cliffs, Utah: Journal of Sedimentary Research, v. 66, no. 4, p. 737–748.

Appendix A

Core Descriptions and Lithofacies Photos

Appendix A contains full core descriptions for two wells in Red Wash Field: RW 12D4-25B and RW 32-29B (see Figure 3A for locations). It also contains photographs of each lithofacies described in Table 1.

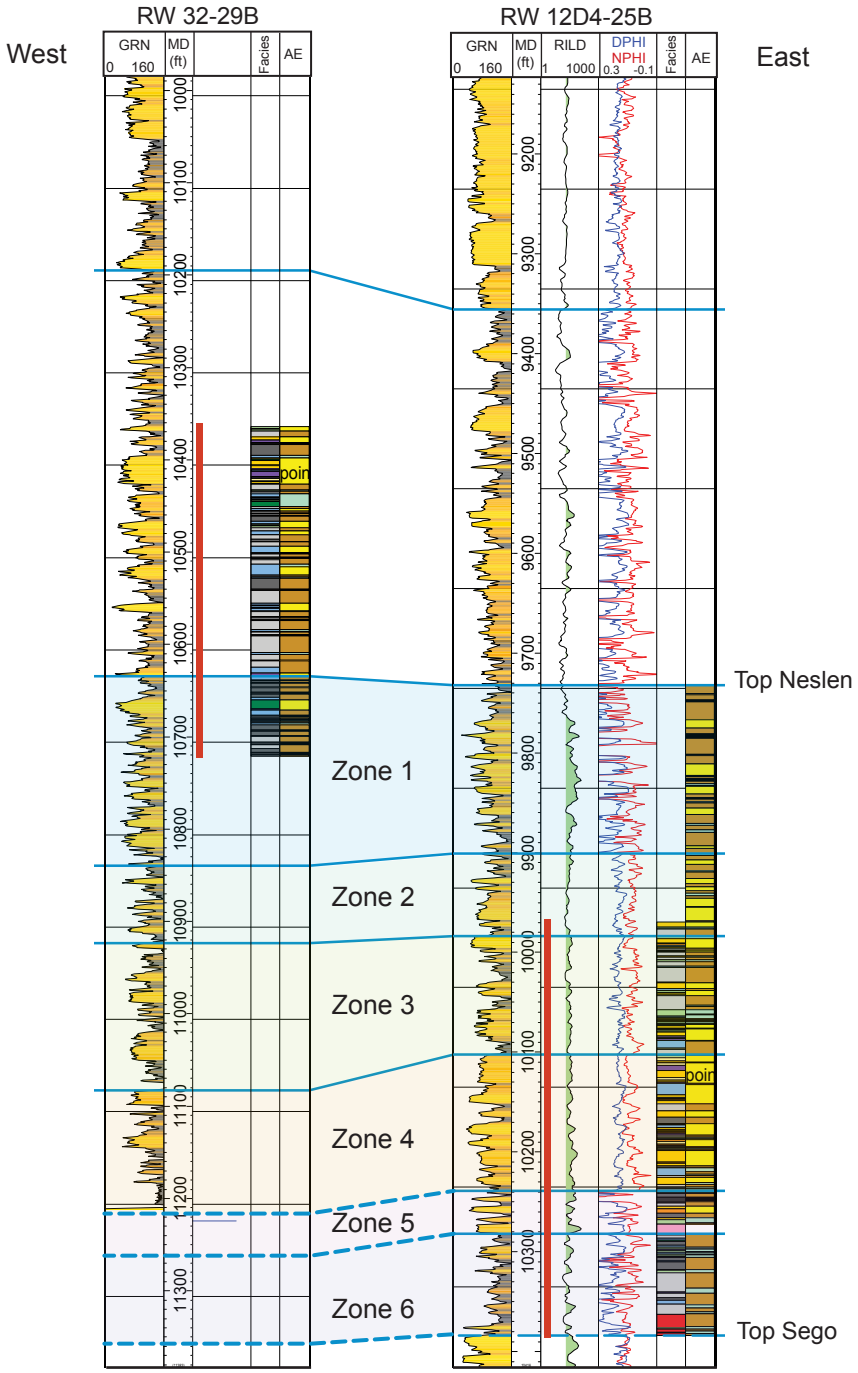

Figure A1. Stratigraphic location of cored intervals (red bars) in RW 32-29B and RW 12D4-25B. Distance between wells is about 4 mi (6.4 km). See Figure 3A for well locations.

Lithofacies Photos

Planar-laminated sandstone/mudrock

Wavy-laminated sandstone/mudrock

Structureless mudrock

Coal

High-angle cross-bedded sandstone

Low-angle cross-bedded to planar-laminated sandstone

Lithofacies Photos

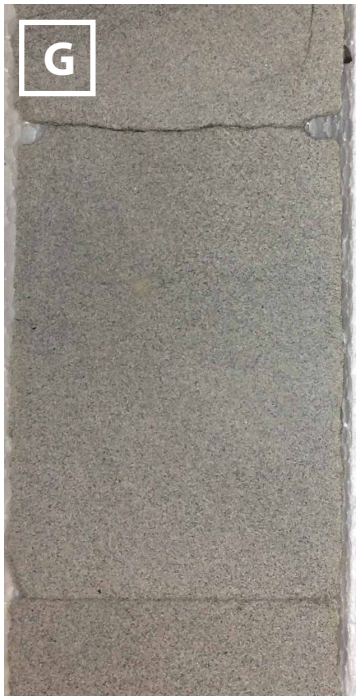

Structureless sandstone

Mudstone-clast conglomeratic sandstone

Carbonaceous siltstone

Carbonaceous siltstone

Contorted sandstone/mudrock

Finely laminated sandstone/mudrock

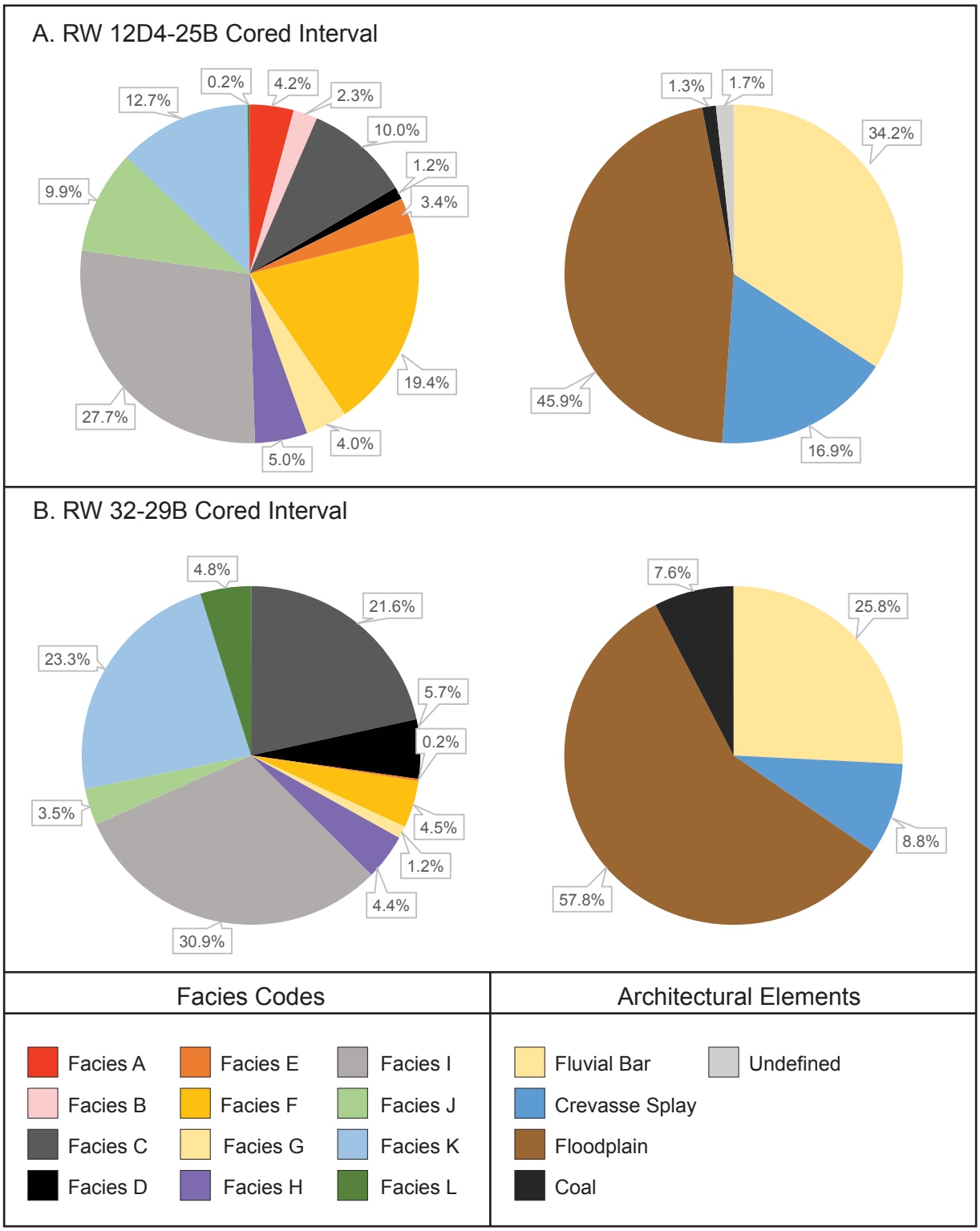

Facies and architectural-element proportions for the cored intervals in RW 12D4-25B and RW 32-29B.

LEGEND FOR MEASURED SECTIONS & CORE DESCRIPTIONS

Lithology

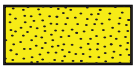
Upper Fine to Coarse-Grained Sandstone

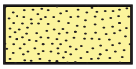
Very Fine to Lower Fine-Grained Sandstone

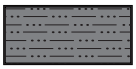
Siltstone


Mudrock (Claystone & Mudstone)


Coal

Sedimentary Structures

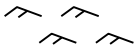
Ripple Laminations

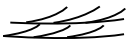
Low-Angle Cross Bedding


High-Angle Cross Bedding


Wavy Laminations


Planar Laminations

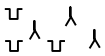
Rooting & Burrows


Convolute Bedding


Mudchip Rip-Up Clasts


Carbonaceous Material

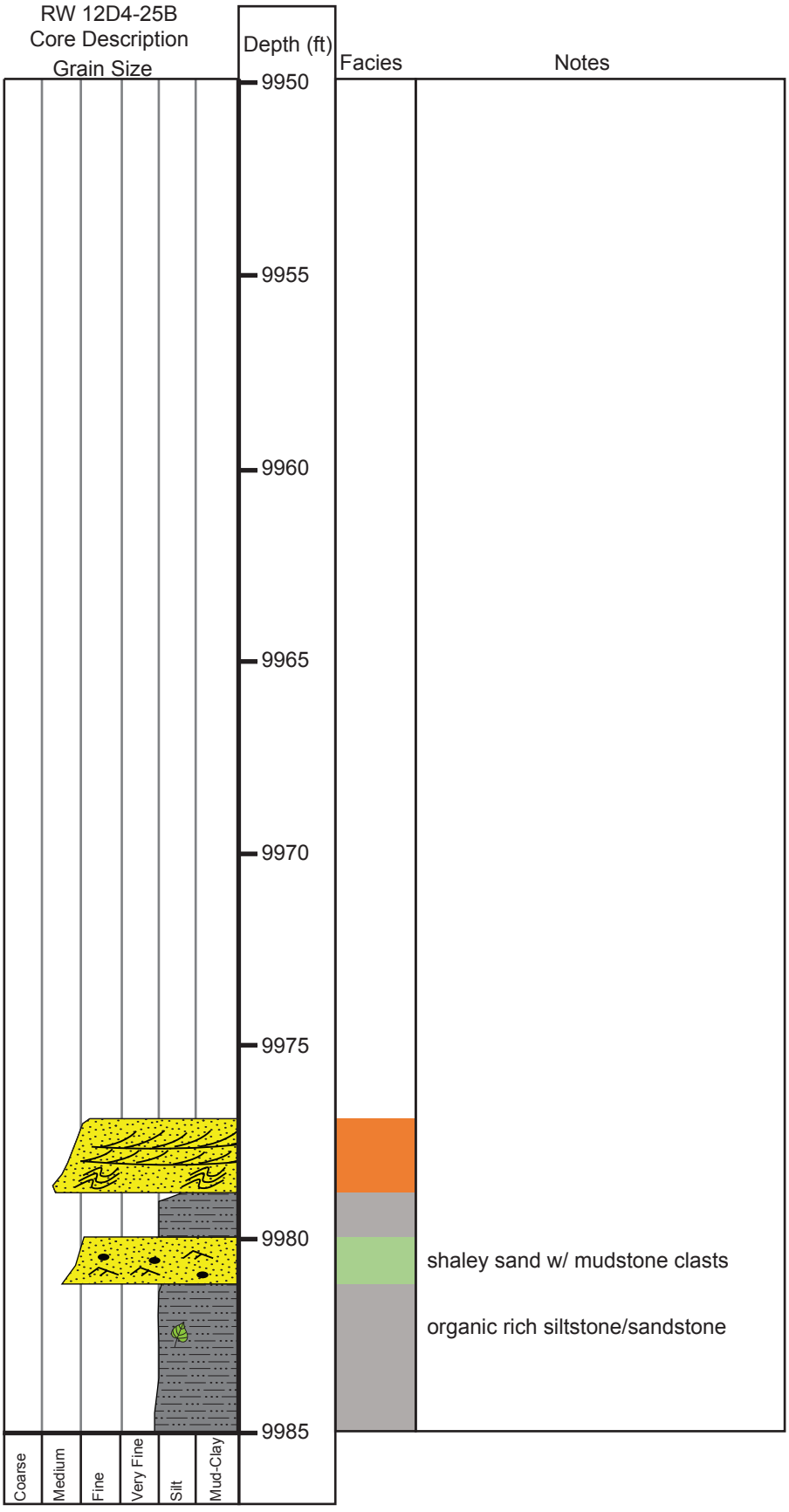
RW 12D4-25B
Core Description
Grain Size
Depth (ft)
Facies
Notes
9950
9955
9960
9965
9970
9975
9980
9985
shaley sand w/ mudstone clasts
organic rich siltstone/sandstone
Coarse
Medium
Fine
Very Fine
Silt
Mud-Clay

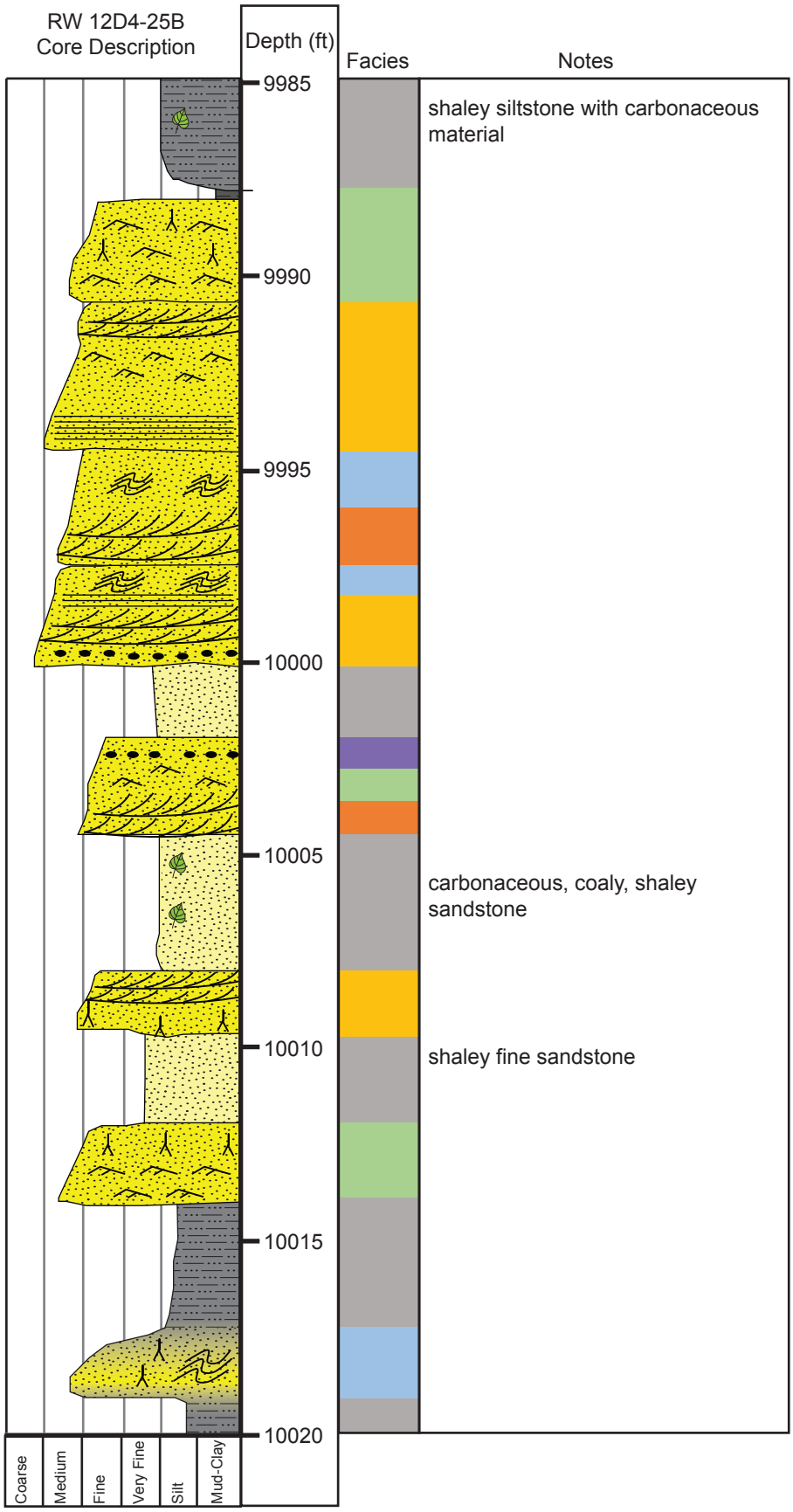
RW 12D4-25B
Core Description
Depth (ft)
Facies
Notes
9985
9990
9995
10000
10005
10010
10015
10020
shaley siltstone with carbonaceous material
carbonaceous, coaly, shaley sandstone
shaley fine sandstone
Coarse
Medium
Fine
Very Fine
Silt
Mud-Clay

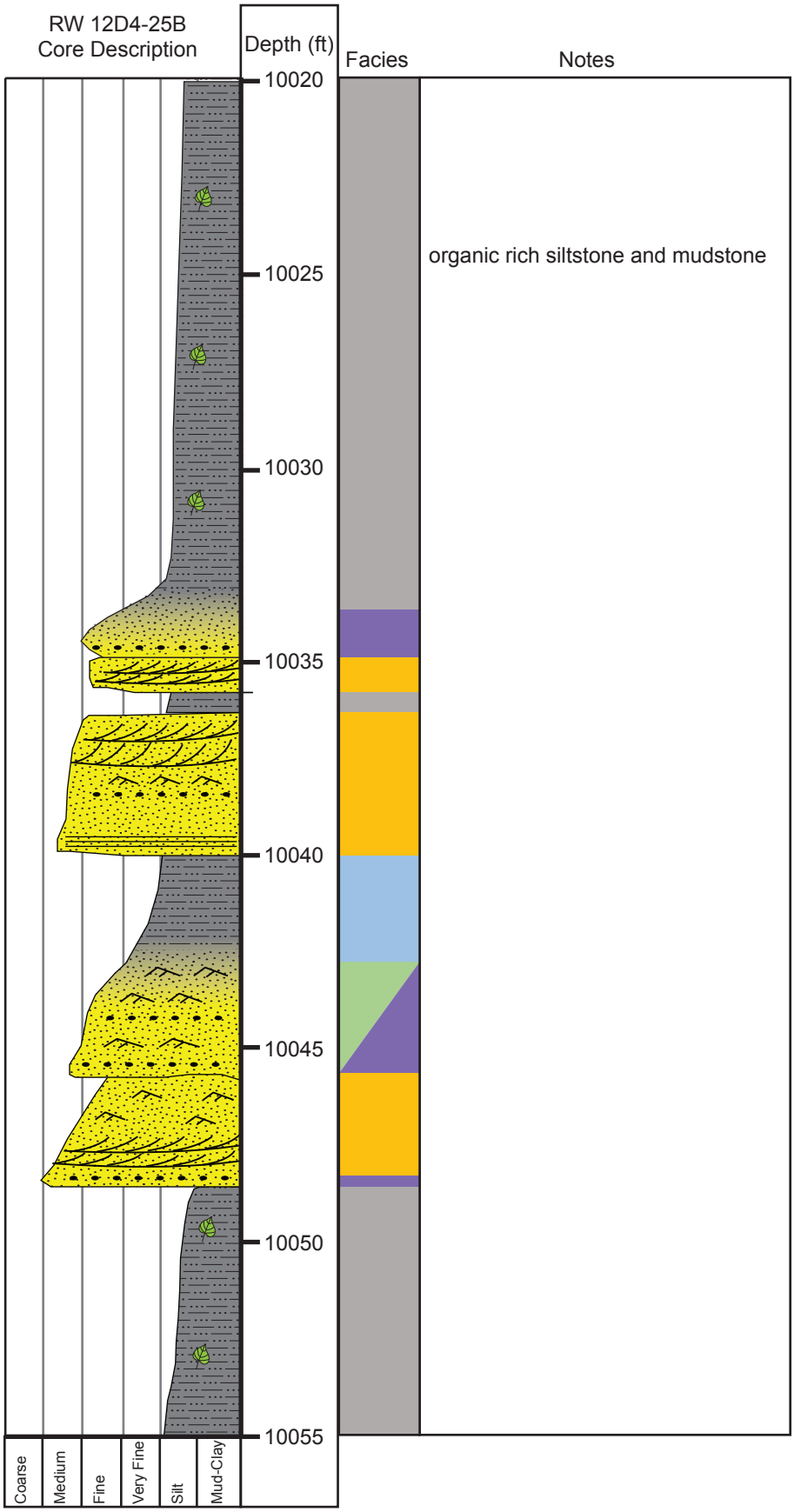
RW 12D4-25B
Core Description
Depth (ft)
Facies
Notes
10020
10025
10030
10035
10040
10045
10050
10055
organic rich siltstone and mudstone
Coarse
Medium
Fine
Very Fine
Silt
Mud-Clay

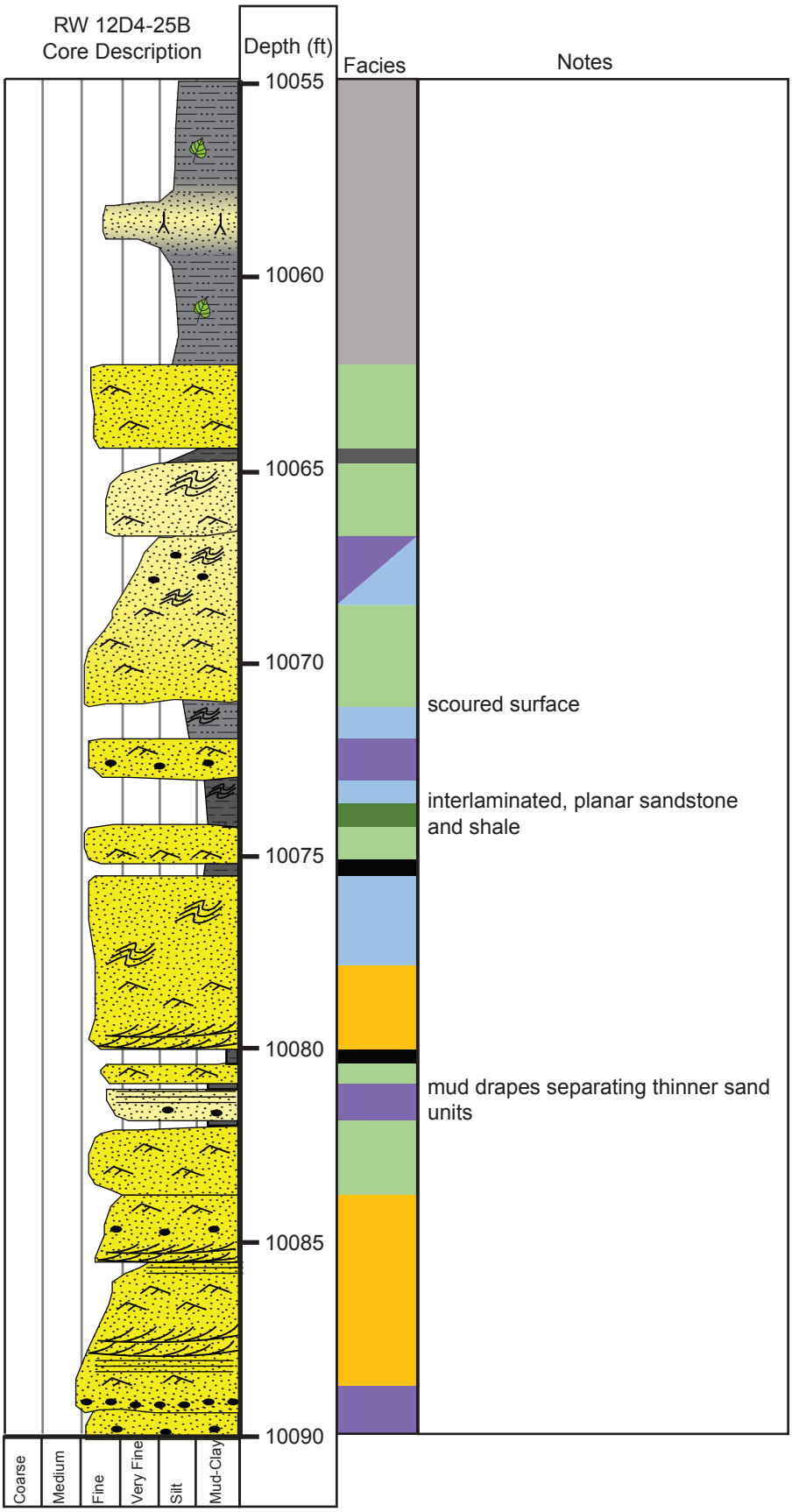
RW 12D4-25B
Core Description
Depth (ft)
Facies
Notes
10055
10060
10065
10070
10075
10080
10085
10090
scoured surface
interlaminated, planar sandstone and shale
mud drapes separating thinner sand units
Coarse
Medium
Fine
Very Fine
Silt
Mud-Clay

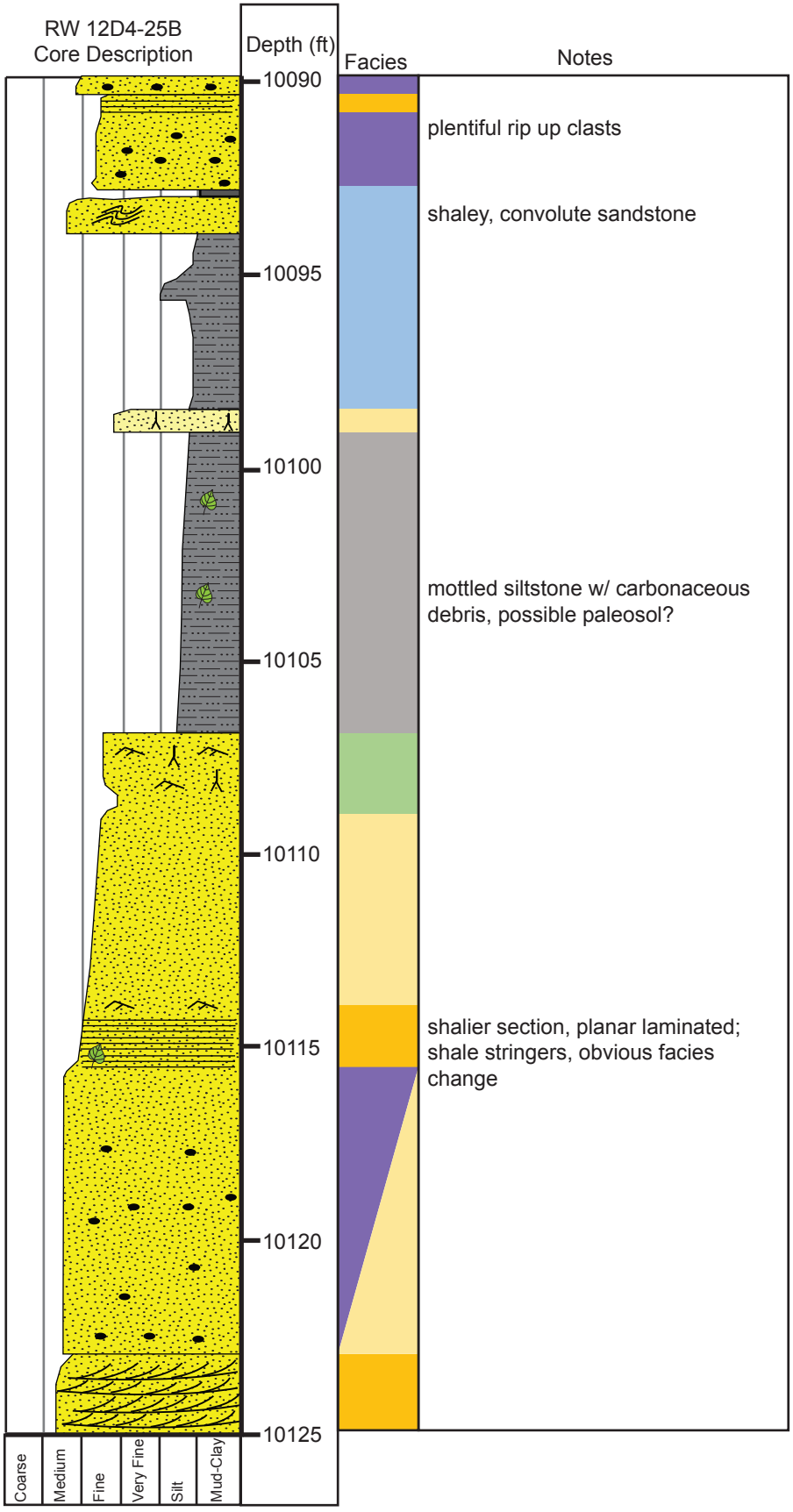
RW 12D4-25B
Core Description
Depth (ft)
Facies
Notes
10090
10095
10100
10105
10110
10115
10120
10125
plentiful rip up clasts
shaley, convolute sandstone
mottled siltstone w/ carbonaceous debris, possible paleosol?
shalier section, planar laminated; shale stringers, obvious facies change
Coarse
Medium
Fine
Very Fine
Silt
Mud-Clay

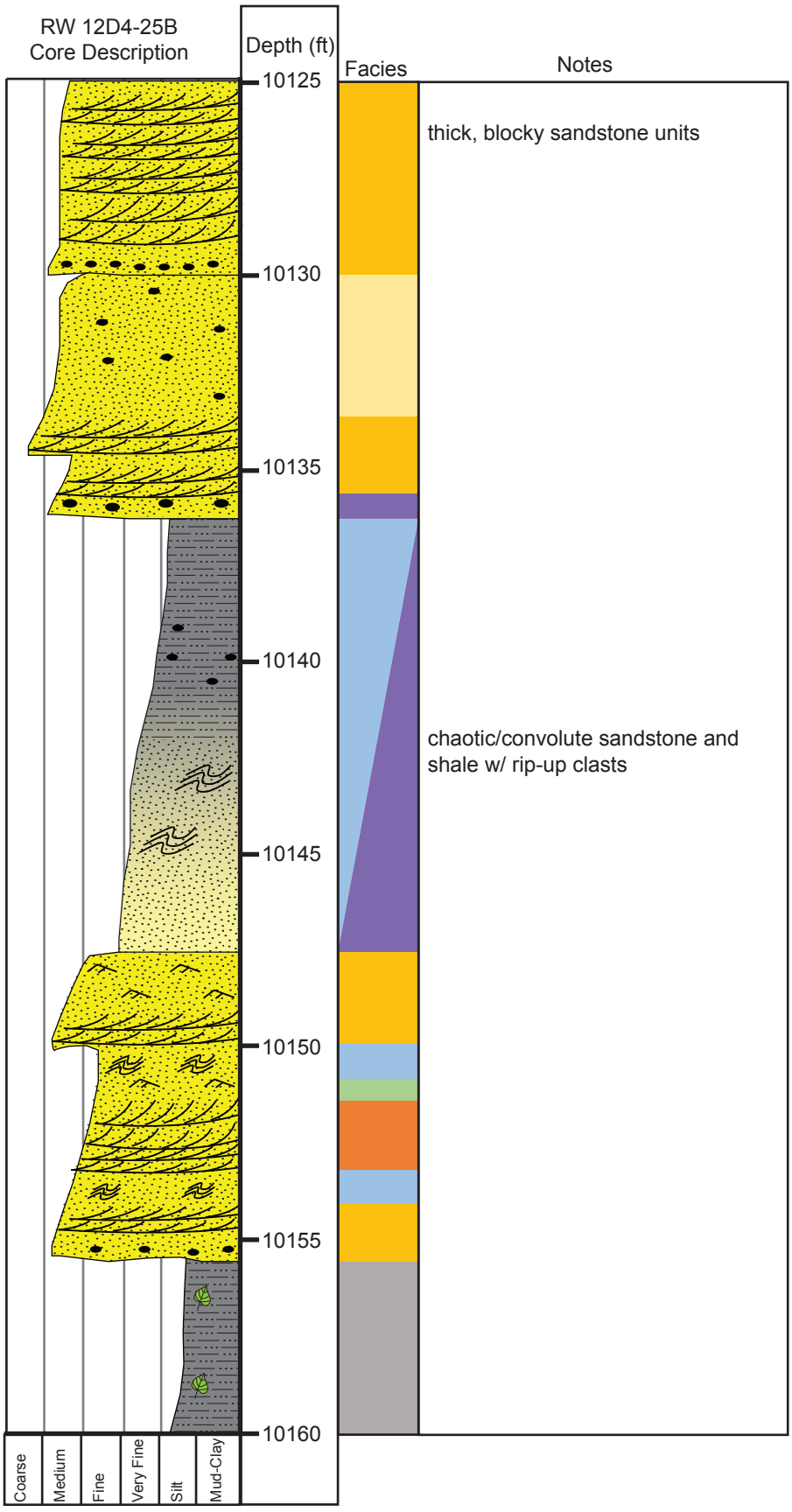
RW 12D4-25B
Core Description
Depth (ft)
Facies
Notes
10125
10130
10135
10140
10145
10150
10155
10160
thick, blocky sandstone units
chaotic/convolute sandstone and
shale w/ rip-up clasts
Coarse
Medium
Fine
Very Fine
Silt
Mud-Clay

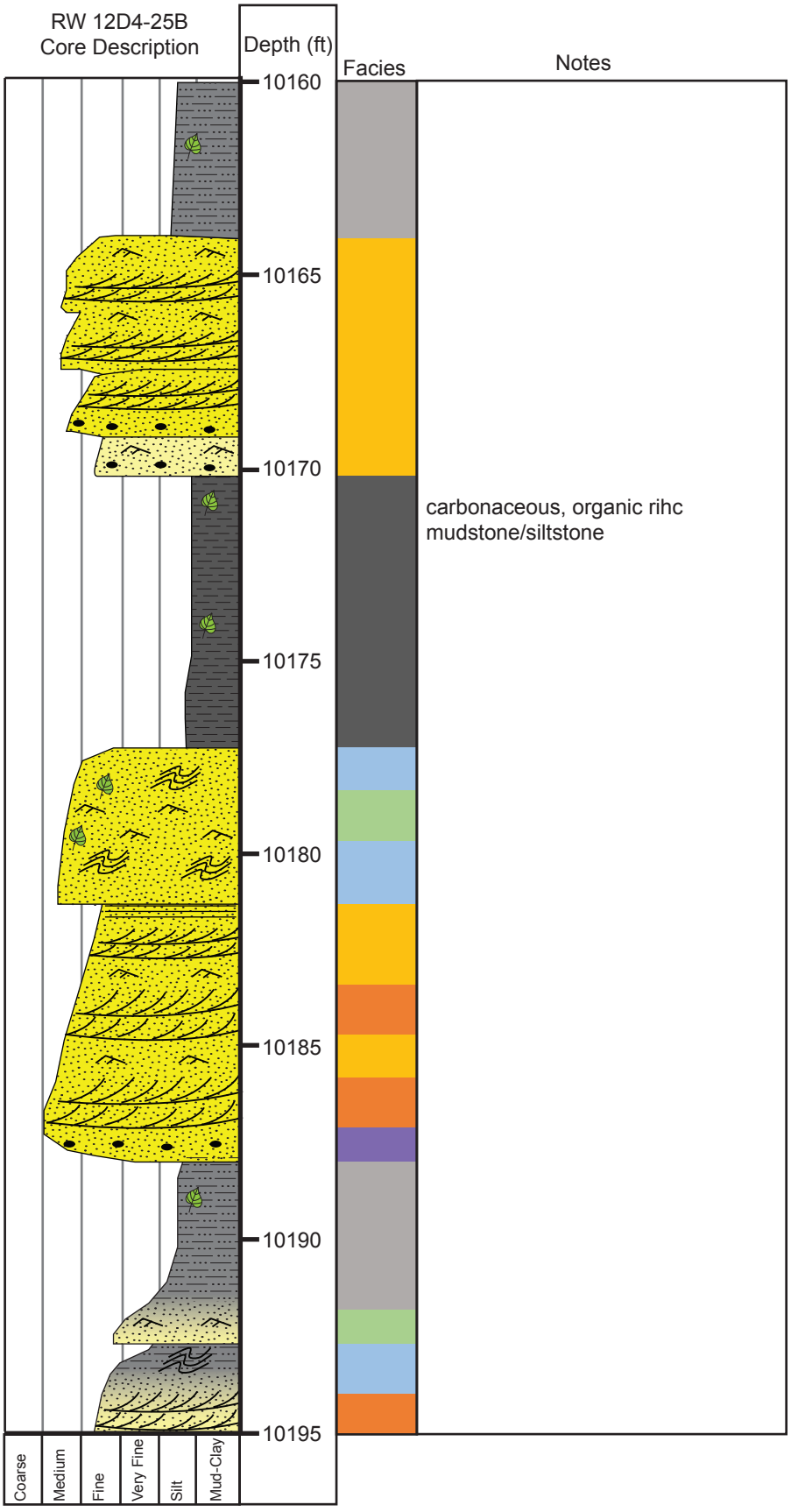
RW 12D4-25B
Core Description
Depth (ft)
Facies
Notes
10160
10165
10170
10175
10180
10185
10190
10195
carbonaceous, organic rihc
mudstone/siltstone
Coarse
Medium
Fine
Very Fine
Silt
Mud-Clay

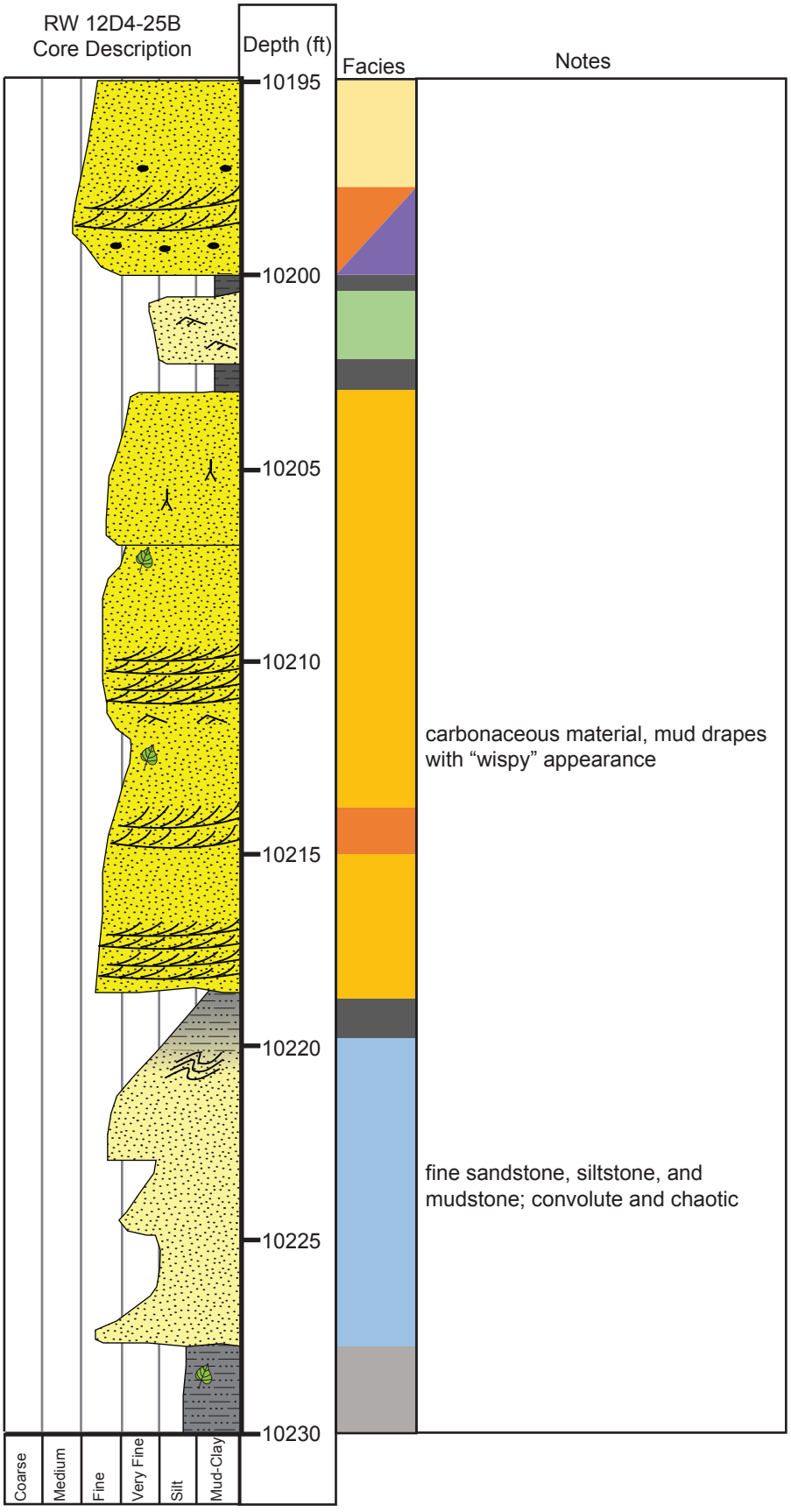
RW 12D4-25B
Core Description
Depth (ft)
Facies
Notes
10195
10200
10205
10210
10215
10220
10225
10230
carbonaceous material, mud drapes with “wispy” appearance
fine sandstone, siltstone, and mudstone; convolute and chaotic
Coarse
Medium
Fine
Very Fine
Silt
Mud-Clay

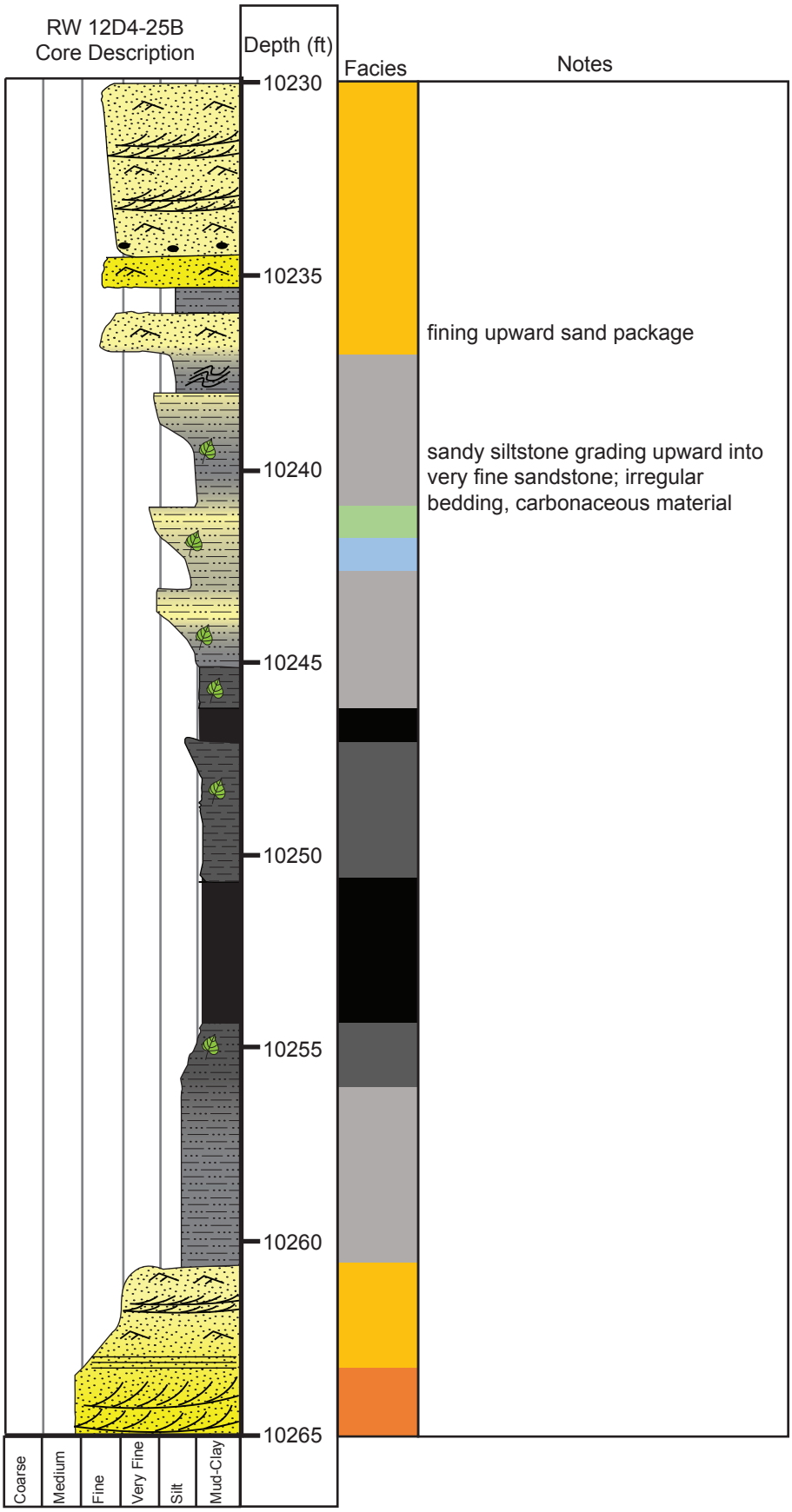
RW 12D4-25B
Core Description
Depth (ft)
Facies
Notes
10230
10235
10240
10245
10250
10255
10260
10265
fining upward sand package
sandy siltstone grading upward into very fine sandstone; irregular bedding, carbonaceous material
Coarse
Medium
Fine
Very Fine
Silt
Mud-Clay

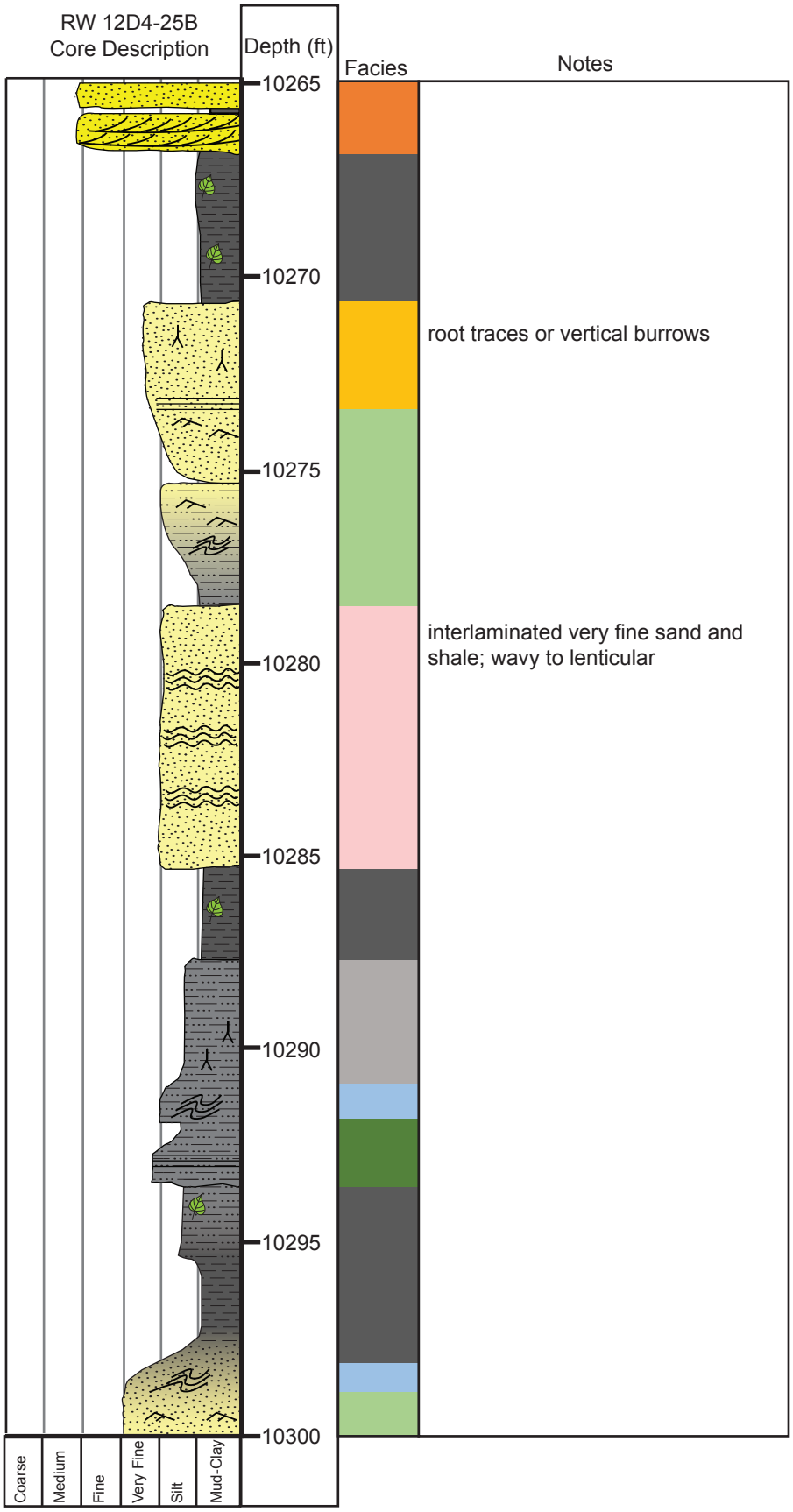
RW 12D4-25B
Core Description
Depth (ft)
Facies
Notes
10265
10270
10275
10280
10285
10290
10295
10300
root traces or vertical burrows
interlaminated very fine sand and shale; wavy to lenticular
Coarse
Medium
Fine
Very Fine
Silt
Mud-Clay

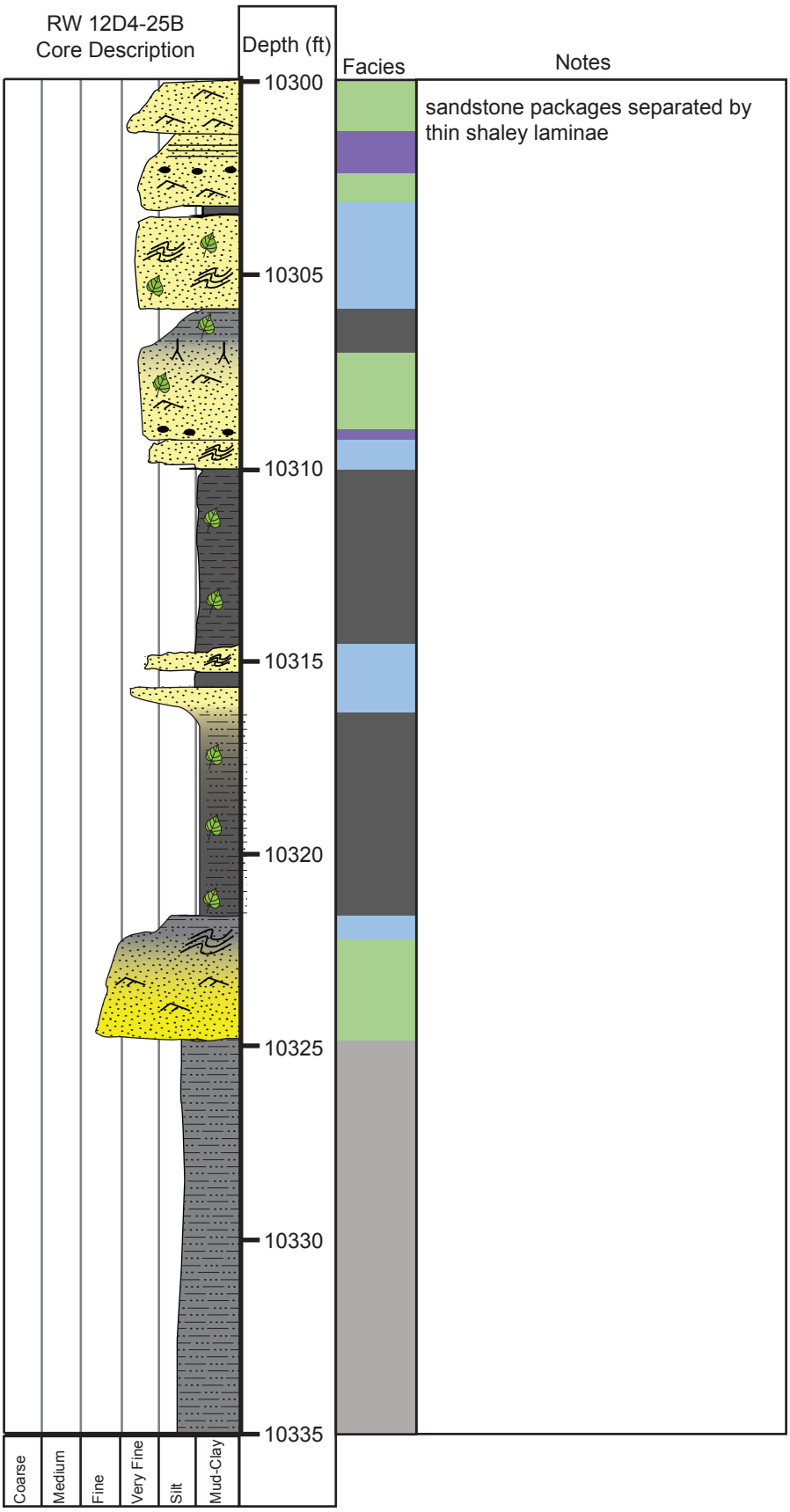
RW 12D4-25B
Core Description
Depth (ft)
Facies
Notes
sandstone packages separated by thin shaley laminae
10300
10305
10310
10315
10320
10325
10330
10335
Coarse
Medium
Fine
Very Fine
Silt
Mud-Clay

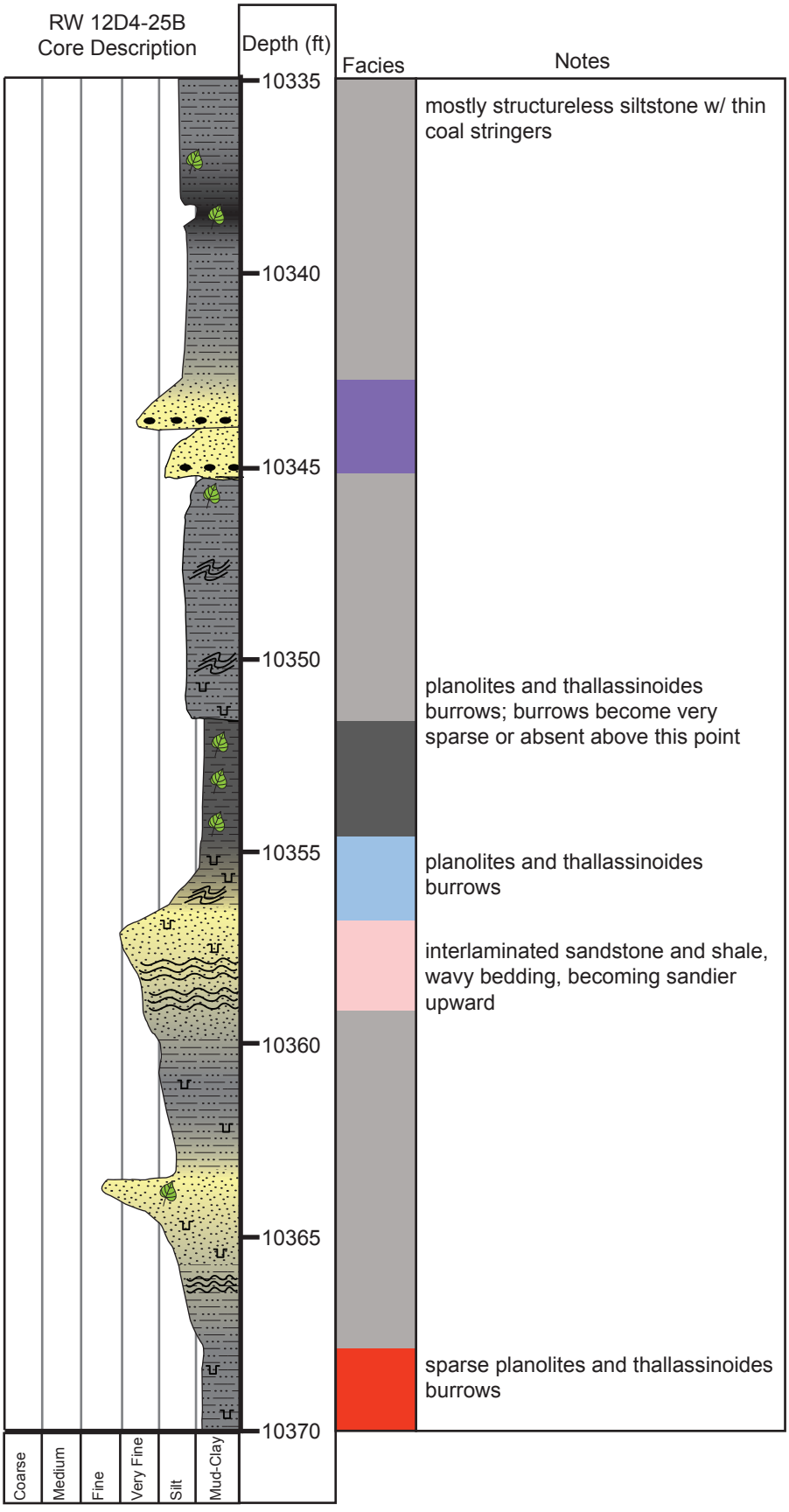
RW 12D4-25B
Core Description
Depth (ft)
Facies
Notes
10335
10340
10345
10350
10355
10360
10365
10370
mostly structureless siltstone w/ thin coal stringers
planolites and thallassinoides burrows; burrows become very sparse or absent above this point
planolites and thallassinoides burrows
interlaminated sandstone and shale, wavy bedding, becoming sandier upward
sparse planolites and thallassinoides burrows
Coarse
Medium
Fine
Very Fine
Silt
Mud-Clay

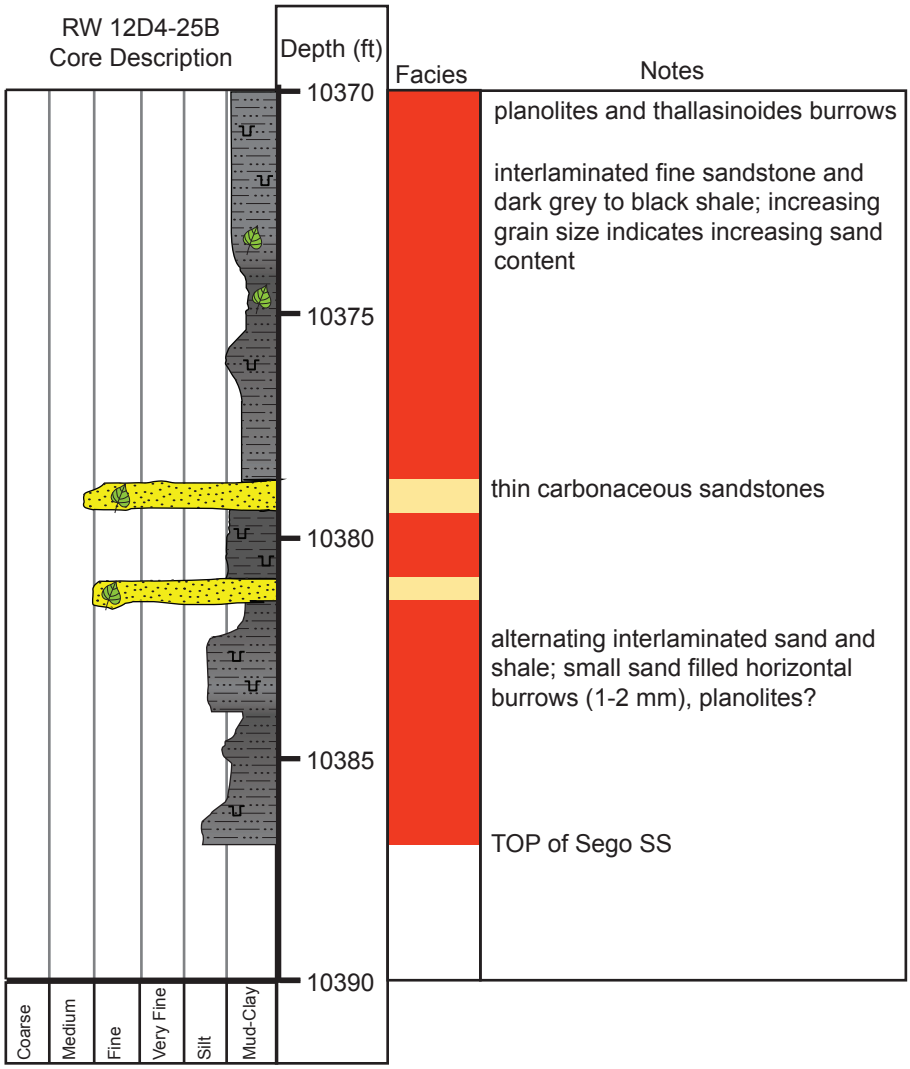
RW 12D4-25B
Core Description
Depth (ft)
Facies
Notes
10370
10375
10380
10385
10390
planolites and thallasinoides burrows
interlaminated fine sandstone and dark grey to black shale; increasing grain size indicates increasing sand content
thin carbonaceous sandstones
alternating interlaminated sand and shale; small sand filled horizontal burrows (1-2 mm), planolites?
TOP of Sego SS
Coarse
Medium
Fine
Very Fine
Silt
Mud-Clay

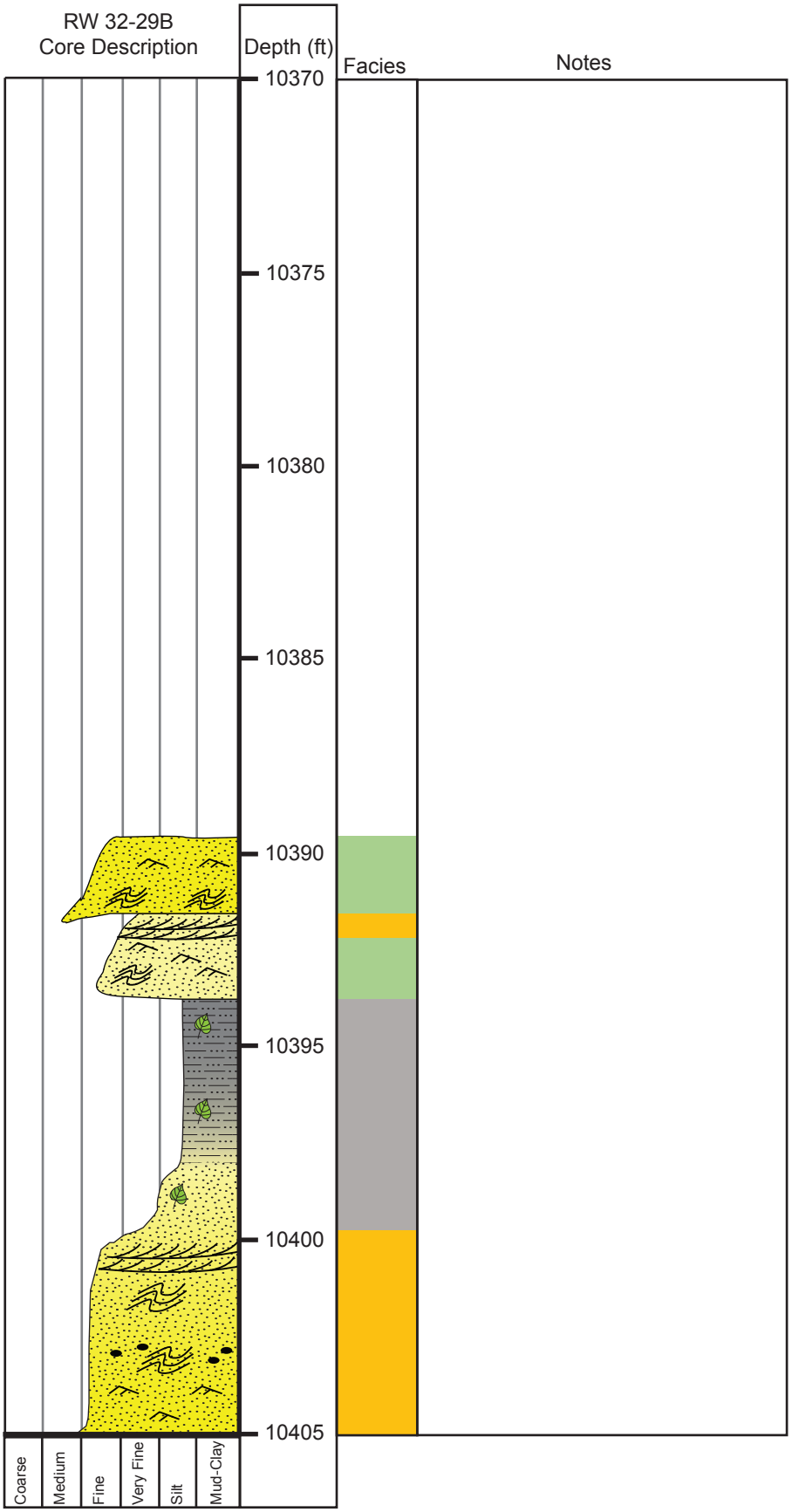
RW 32-29B
Core Description
Depth (ft)
Facies
Notes
10370
10375
10380
10385
10390
10395
10400
10405
Coarse
Medium
Fine
Very Fine
Silt
Mud-Clay

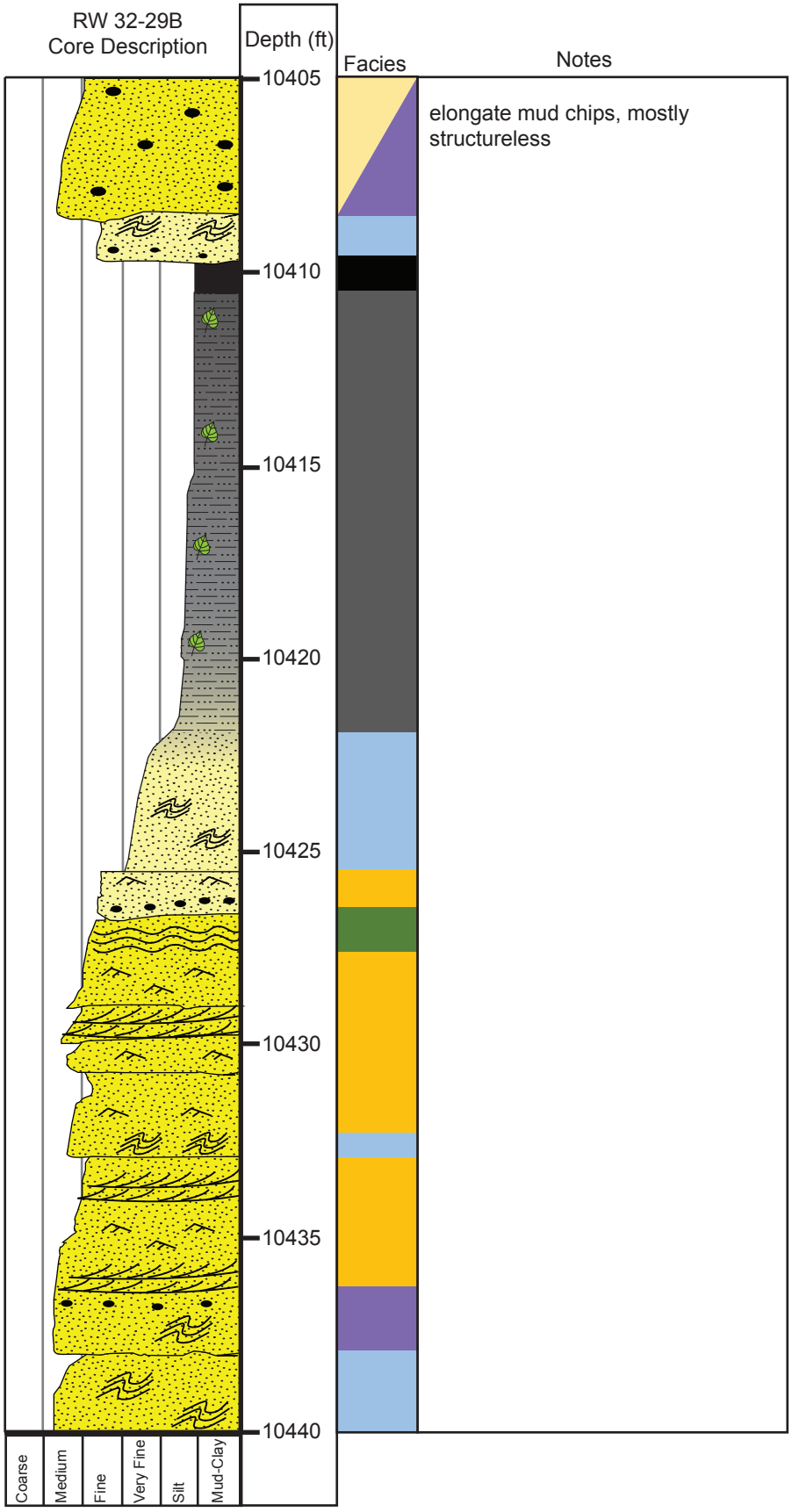
RW 32-29B
Core Description
Depth (ft)
Facies
Notes
10405
10410
10415
10420
10425
10430
10435
10440
elongate mud chips, mostly structureless
Coarse
Medium
Fine
Very Fine
Silt
Mud-Clay

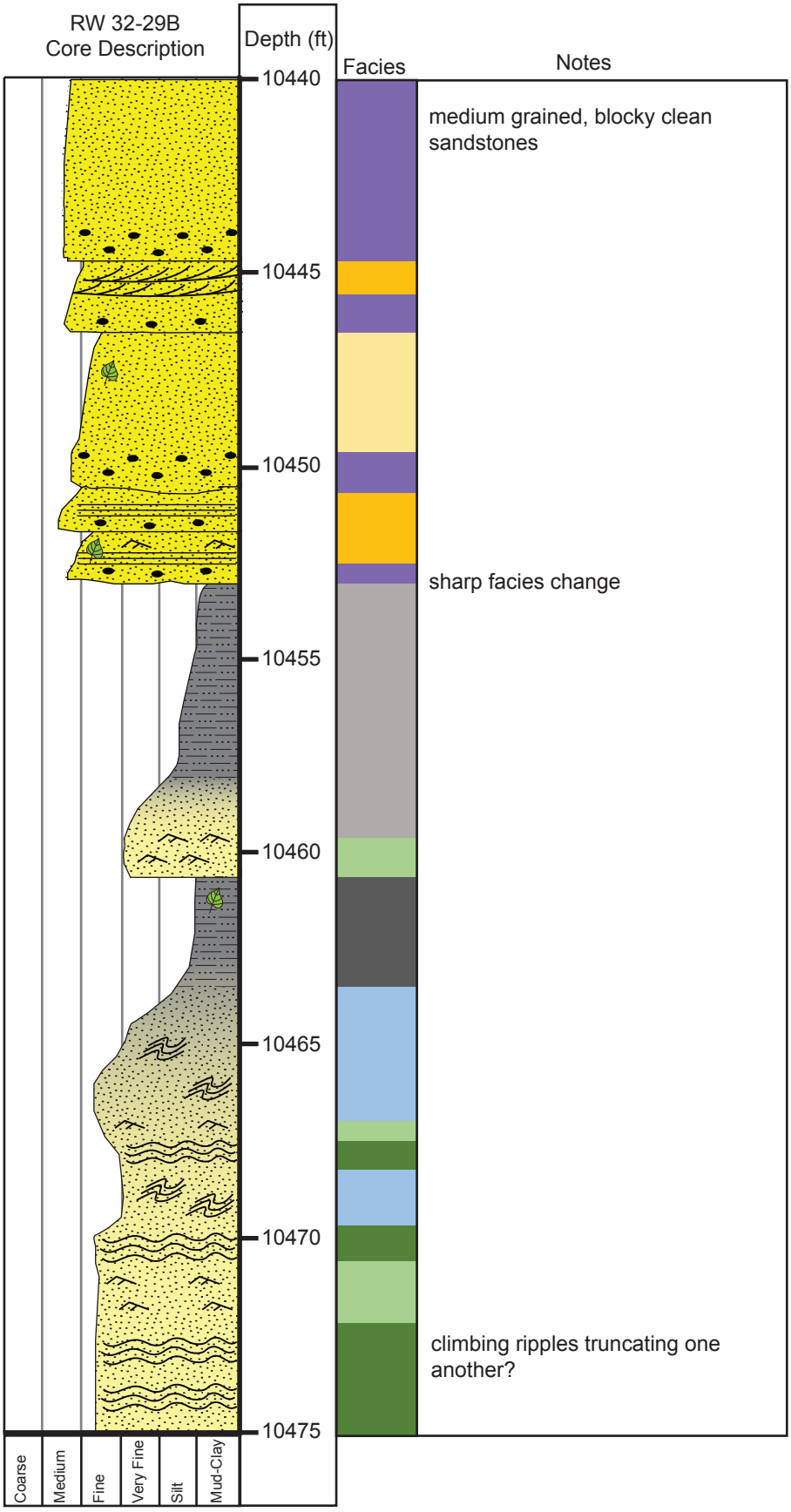
RW 32-29B
Core Description
Depth (ft)
Facies
Notes
10440
10445
10450
10455
10460
10465
10470
10475
medium grained, blocky clean sandstones
sharp facies change
climbing ripples truncating one another?
Coarse
Medium
Fine
Very Fine
Silt
Mud-Clay

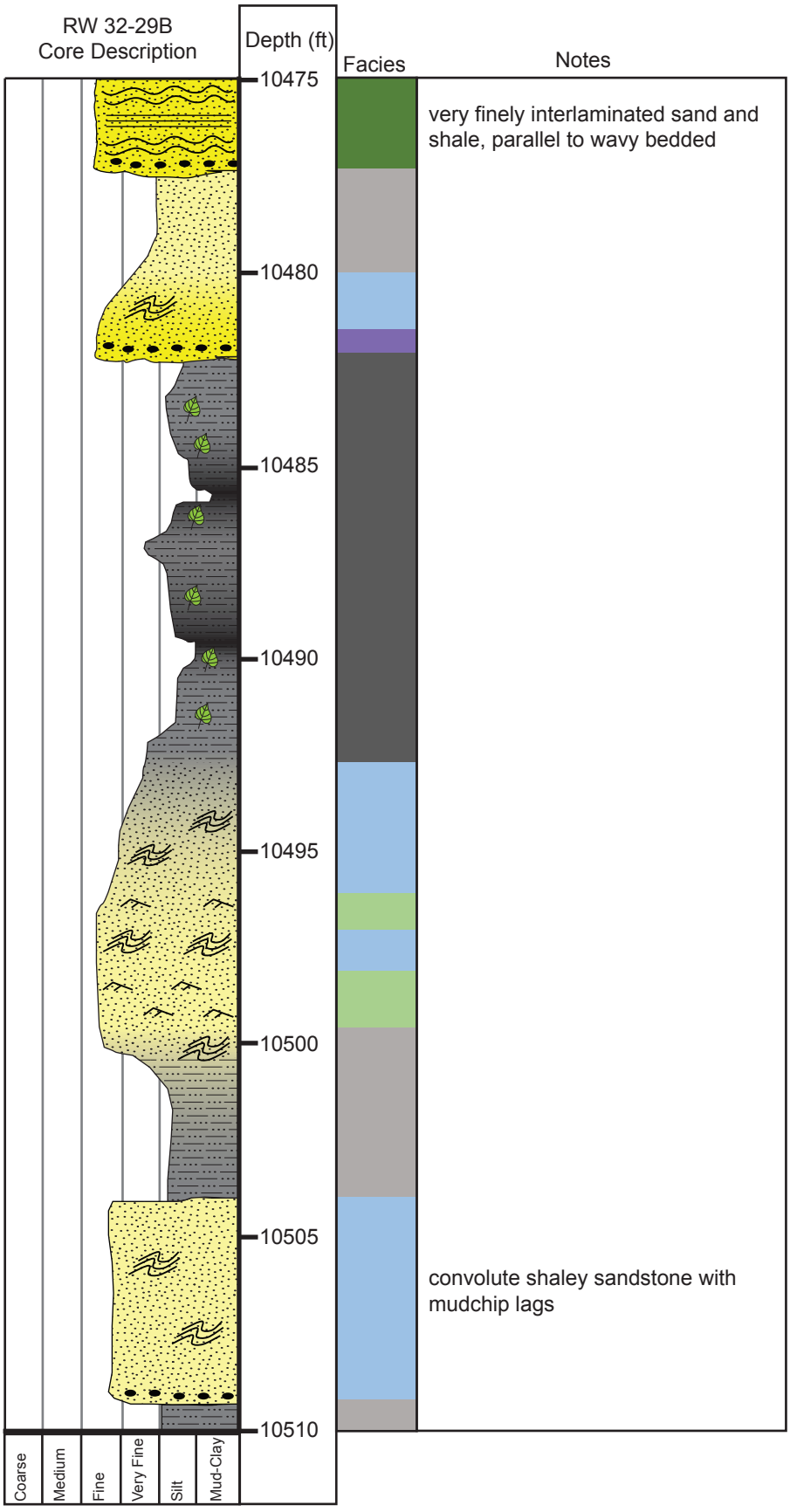
RW 32-29B
Core Description
Depth (ft)
Facies
Notes
10475
10480
10485
10490
10495
10500
10505
10510
very finely interlaminated sand and shale, parallel to wavy bedded
convolute shaley sandstone with mudchip lags
Coarse
Medium
Fine
Very Fine
Silt
Mud-Clay

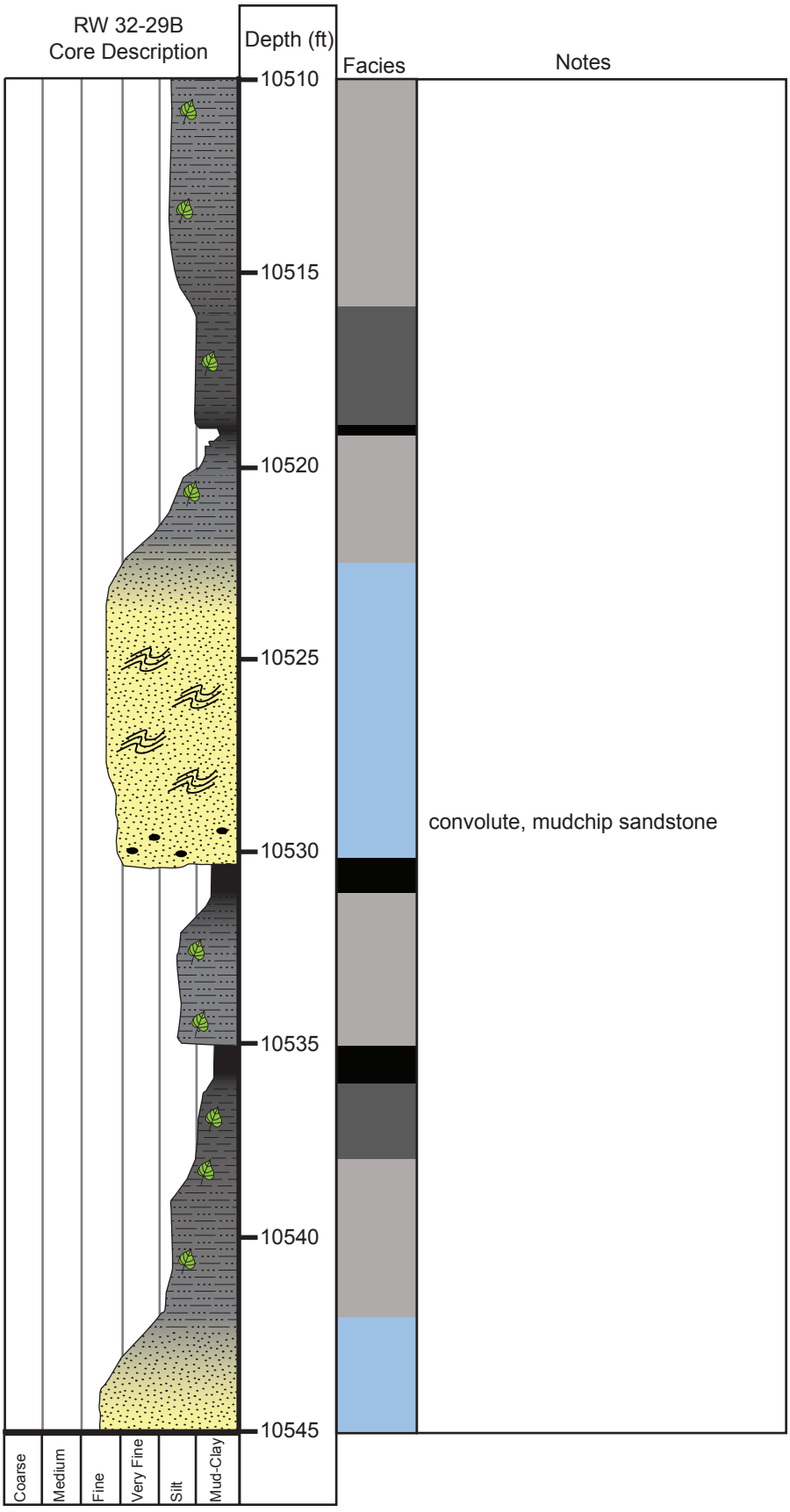
RW 32-29B
Core Description
Depth (ft)
Facies
Notes
10510
10515
10520
10525
10530
10535
10540
10545
convolute, mudchip sandstone
Coarse
Medium
Fine
Very Fine
Silt
Mud-Clay

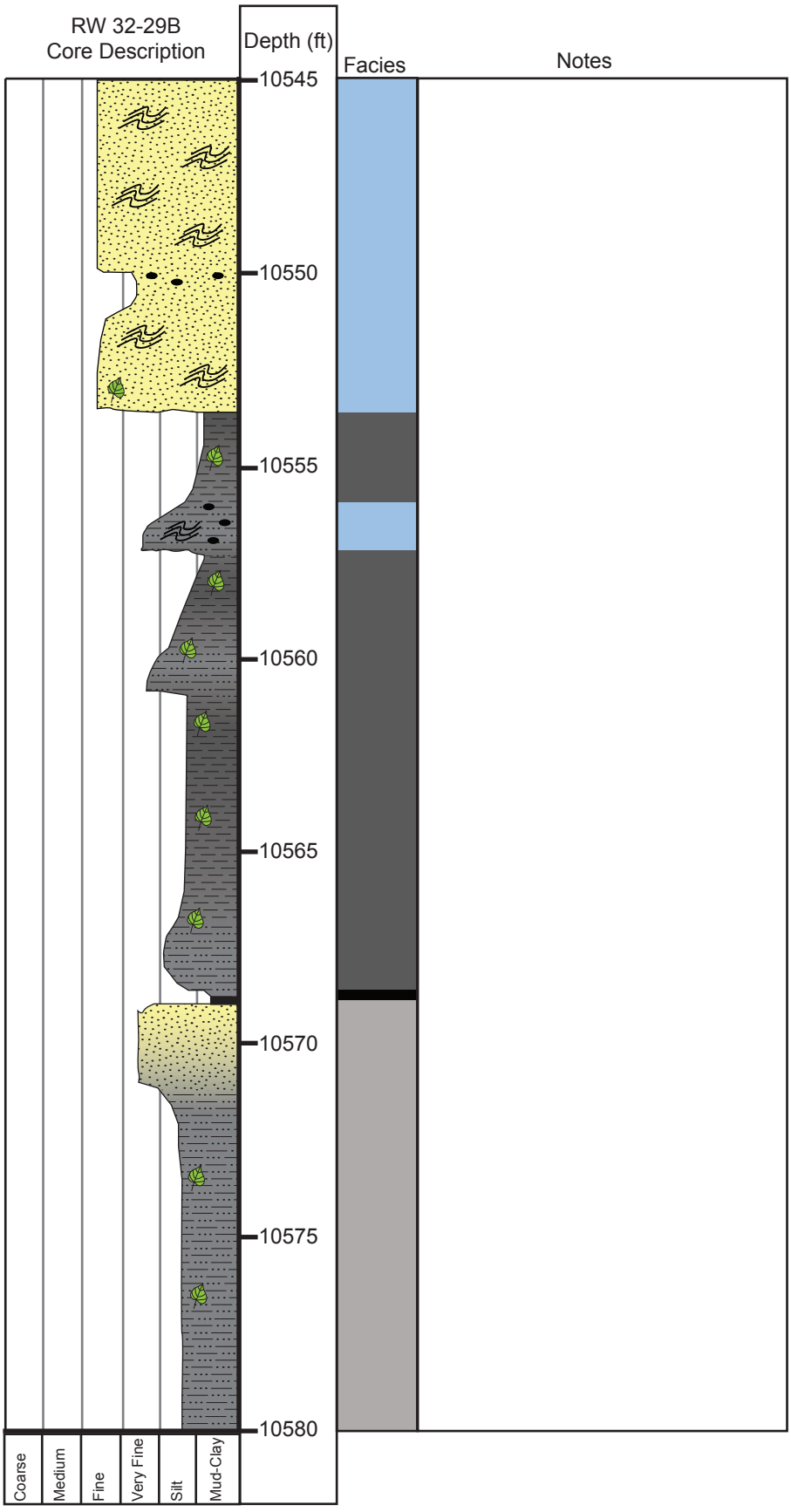
RW 32-29B
Core Description
Depth (ft)
Facies
Notes
10545
10550
10555
10560
10565
10570
10575
10580
Coarse
Medium
Fine
Very Fine
Silt
Mud-Clay

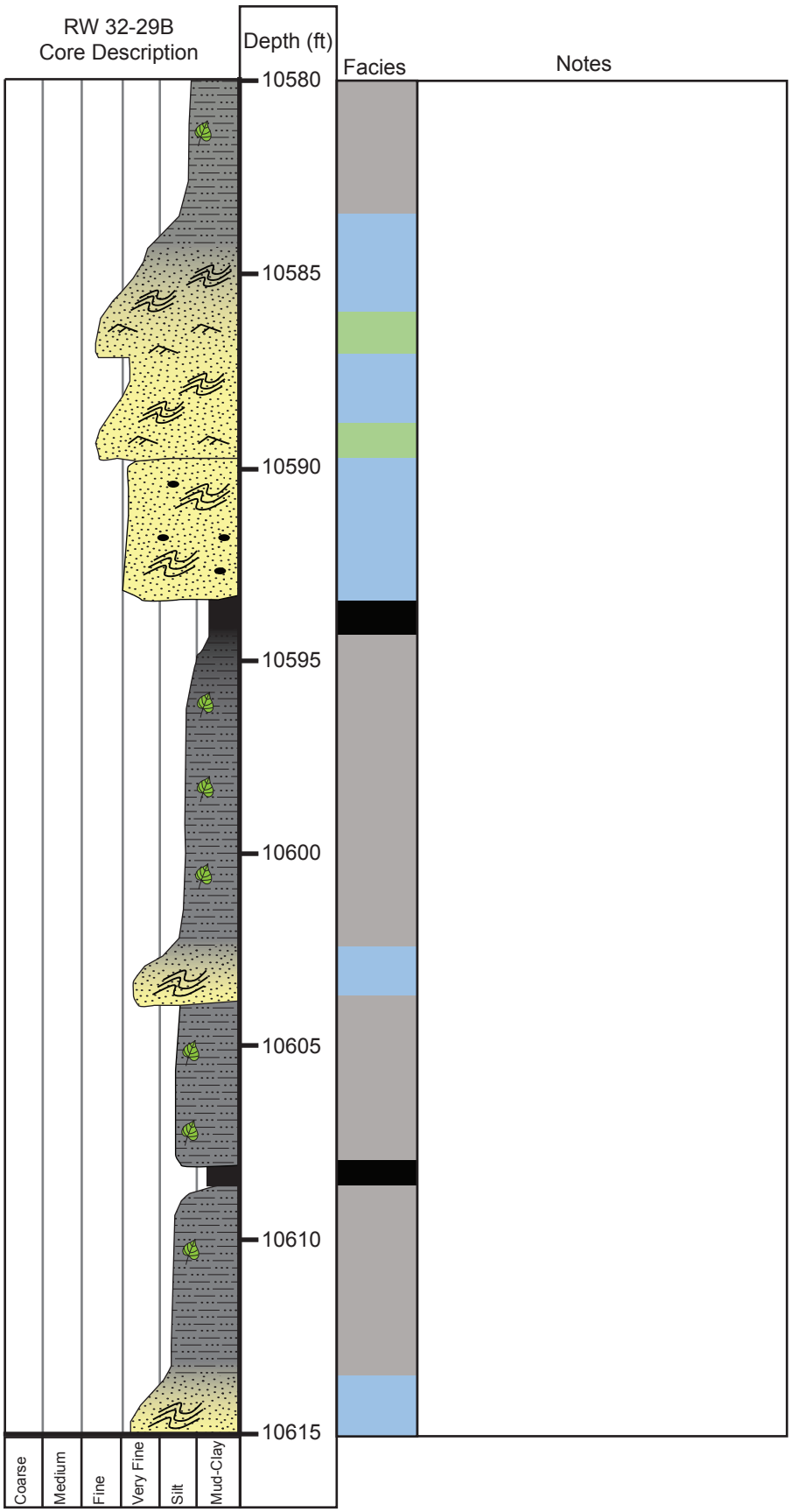
RW 32-29B
Core Description
Depth (ft)
Facies
Notes
10580
10585
10590
10595
10600
10605
10610
10615
Coarse
Medium
Fine
Very Fine
Silt
Mud-Clay

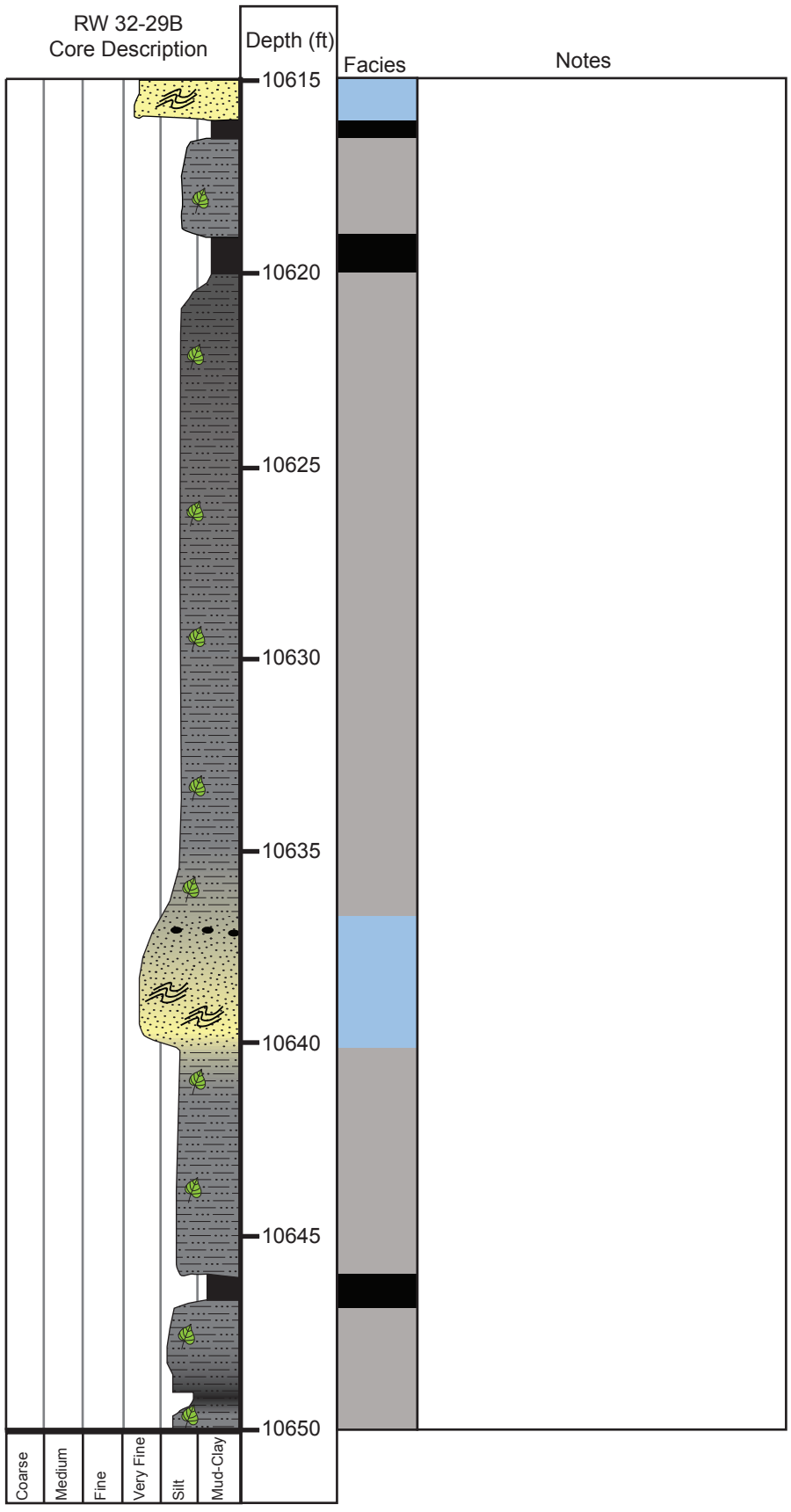
RW 32-29B
Core Description
Depth (ft)
Facies
Notes
10615
10620
10625
10630
10635
10640
10645
10650
Coarse
Medium
Fine
Very Fine
Silt
Mud-Clay

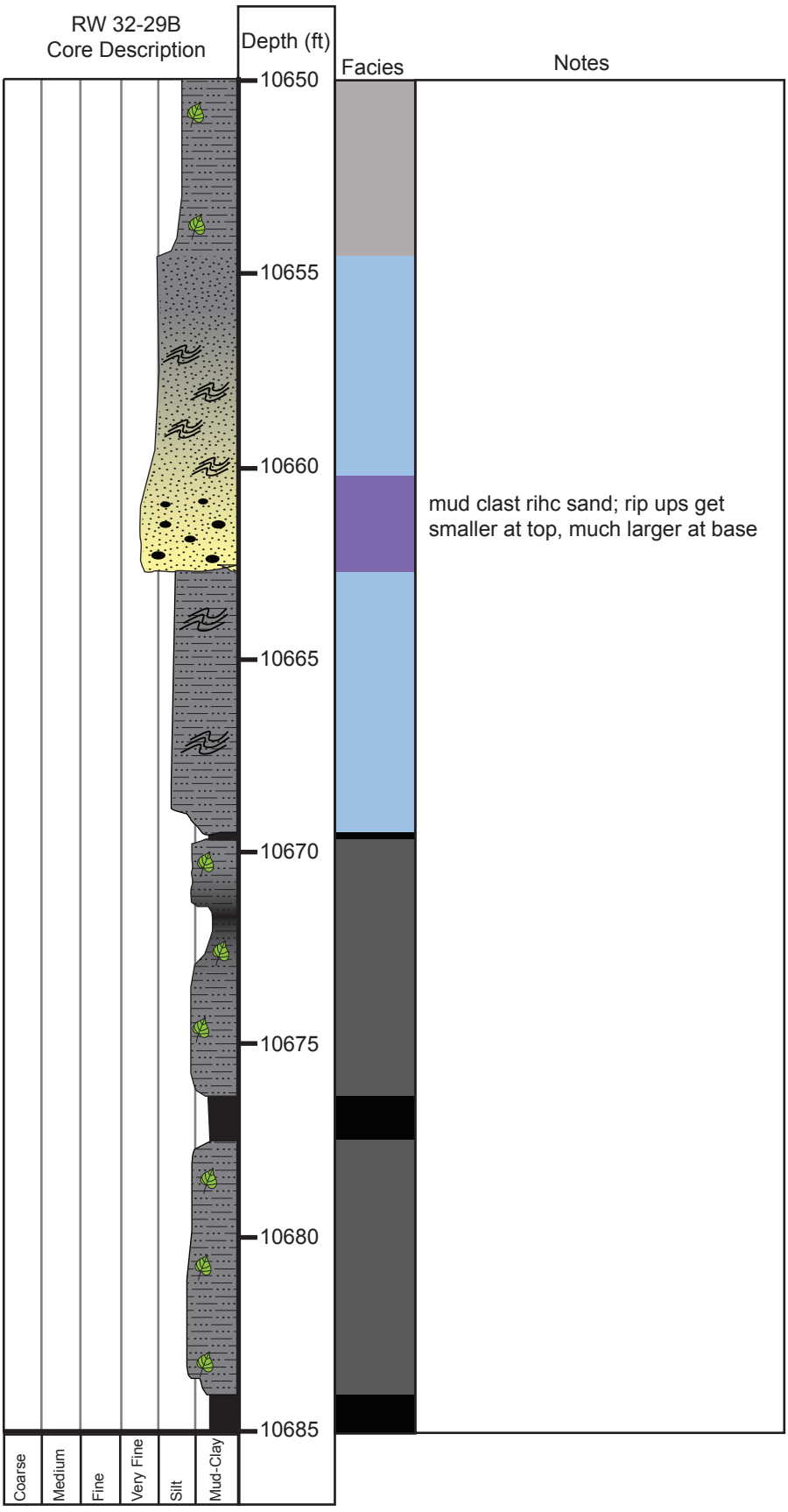
RW 32-29B
Core Description
Depth (ft)
Facies
Notes
10650
10655
10660
10665
10670
10675
10680
10685
mud clast rihc sand; rip ups get smaller at top, much larger at base
Coarse
Medium
Fine
Very Fine
Silt
Mud-Clay

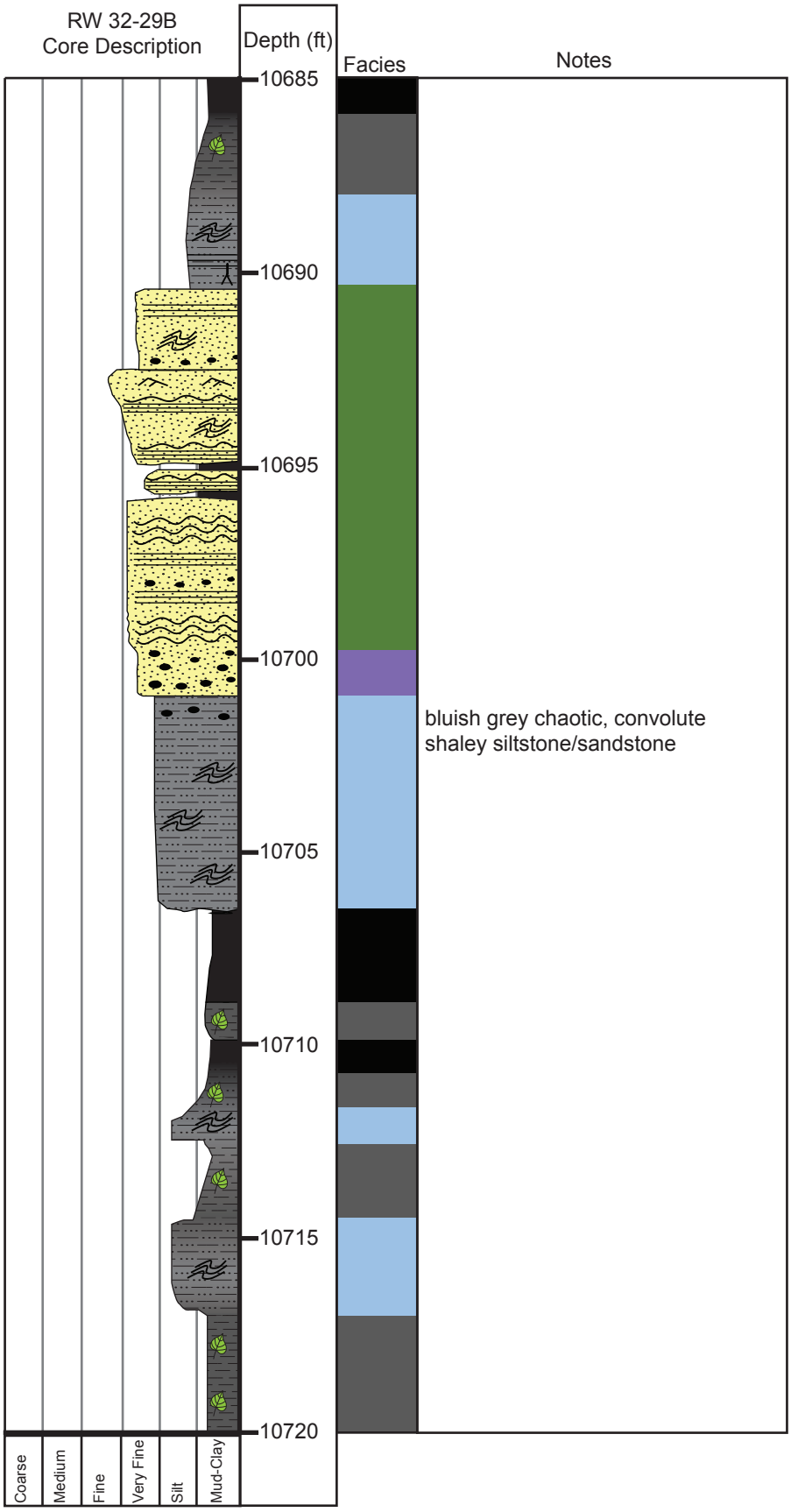
RW 32-29B
Core Description
Depth (ft)
Facies
Notes
10685
10690
10695
10700
10705
10710
10715
10720
bluish grey chaotic, convolute
shaley siltstone/sandstone
Coarse
Medium
Fine
Very Fine
Silt
Mud-Clay

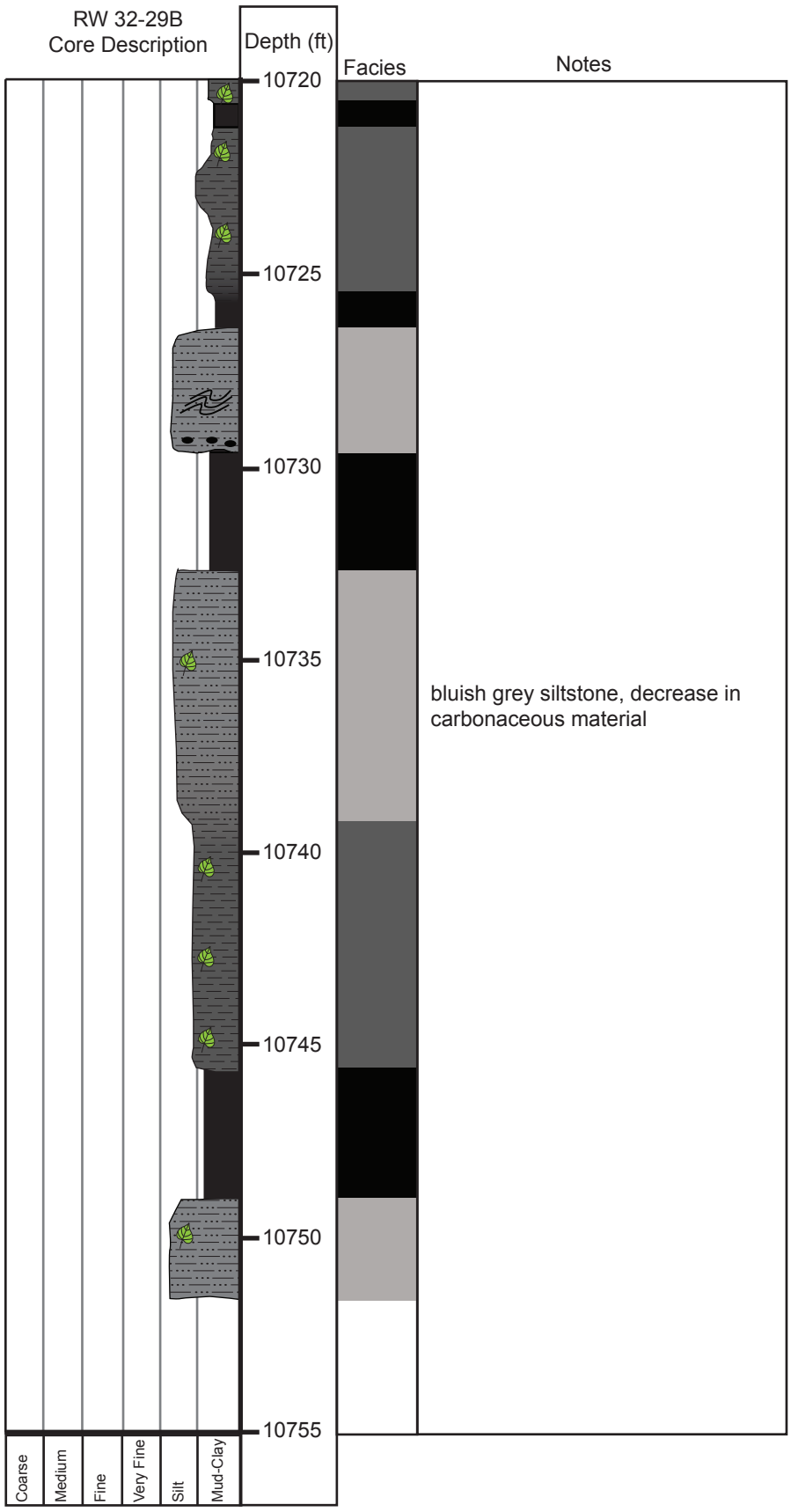
RW 32-29B
Core Description
Depth (ft)
Facies
Notes
10720
10725
10730
10735
10740
10745
10750
10755
bluish grey siltstone, decrease in carbonaceous material
Coarse
Medium
Fine
Very Fine
Silt
Mud-Clay

Appendix B

Outcrop Photos, Measured Section Descriptions, Fieldwork Data

Appendix B contains additional outcrop photos and full descriptions for each of the four measured sections, totaling 663.4 ft (202 m) collected along the western flank of the Douglas Creek Arch (see Figure 3B for locations). Observations were collected along each measured section and include descriptions of: lithology, grain size, sedimentary structures, ichnofossils, and nature of bounding surfaces. All paleocurrent measurements were acquired from ripple marks using a Brunton compass. Structure corrected measurements can be found in this appendix (approximate strike/dip = 177°/12°), but uncorrected values were used for rose diagrams in Figure 8 (cross section of measured section). Spectral gamma-ray readings were collected in 1 ft (0.3 m) increments using an RS-125 Super Spec hand-held scintillation counter (Radiation Solutions, Inc., Canada). Each measurement was collected in assay mode over the course of 60 seconds. If accessible, shale intervals were trenched using a pick axe and gamma-ray measurements were collected on fresh, exposed surfaces. Untrenched, covered intervals were assumed to be fine-grained floodplain deposits, and spectral gamma-ray values were estimated using typical readings from trenched intervals: 40 total cps, 3.0% potassium (K), 25 ppm thorium (Th), and 7.5 ppm uranium (U).

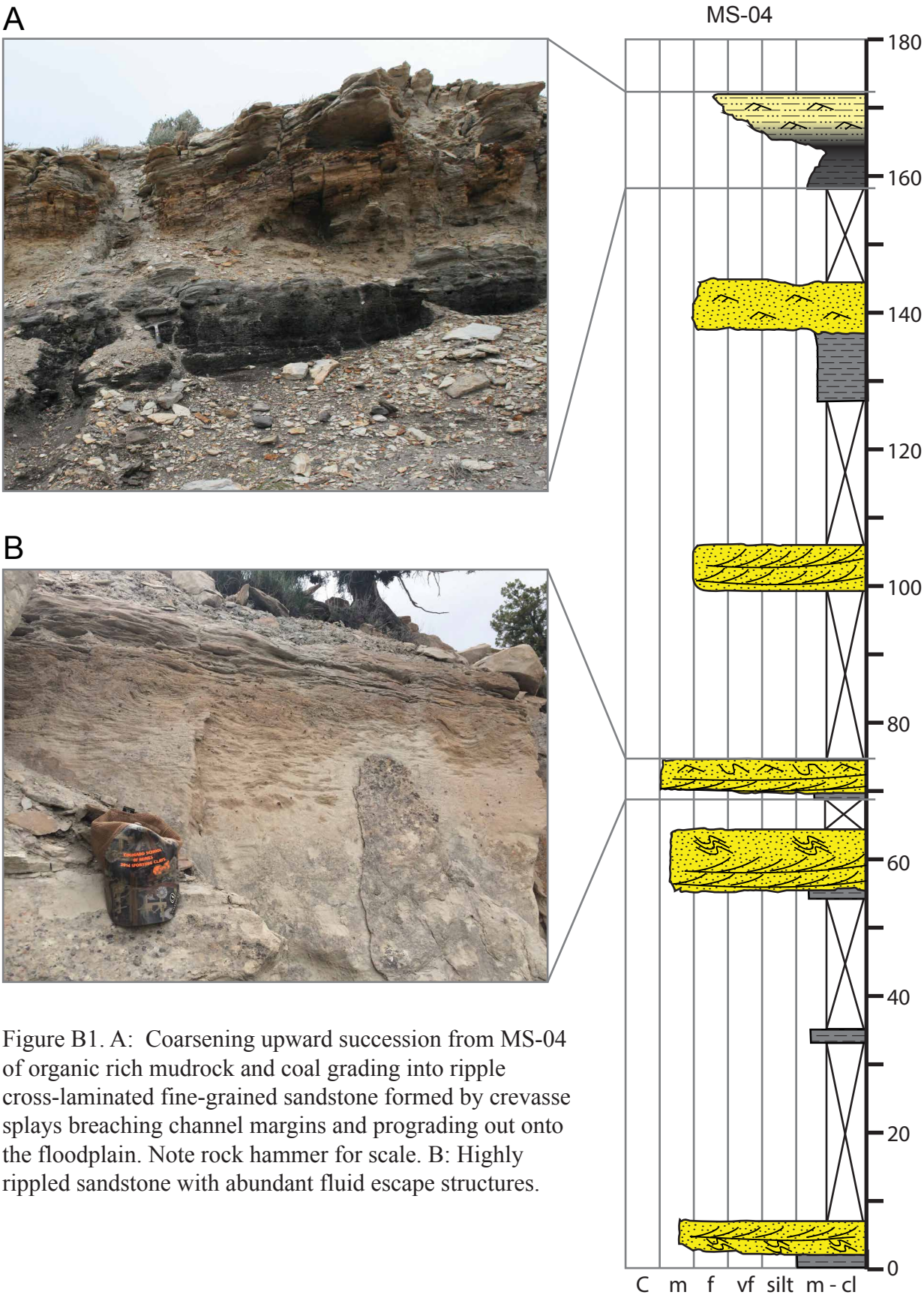

Figure B1. A: Coarsening upward succession from MS-04 of organic rich mudrock and coal grading into ripple cross-laminated fine-grained sandstone formed by crevasse splays breaching channel margins and prograding out onto the floodplain. Note rock hammer for scale. B: Highly rippled sandstone with abundant fluid escape structures.

A

B

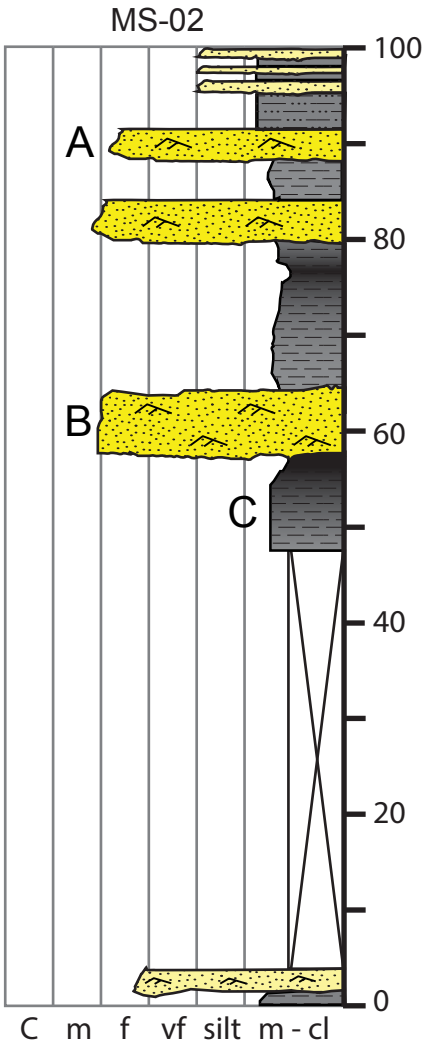

C

Figure B2. A: Ripple cross-laminated sandstone. Hammer for scale (~1 ft [0.3 m]). B: Sharp contact between rippled sandstone and organic rich mudrock and coal below. C: Plant debris cast preserved on the parting of an organic rich mudrock interval.

A

B

Figure B3. A: Contorted bedding in a rippled sandstone bed caused by dinosaur footprints. B: Sand-filled casts of two separate footprints from a three-toed dinosaur, possibly a hadrosaur (Martin Lockley, personal communication).

LEGEND FOR MEASURED SECTIONS & CORE DESCRIPTIONS

Lithology

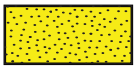
Upper Fine to Coarse-Grained Sandstone

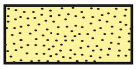
Very Fine to Lower Fine-Grained Sandstone


Siltstone


Mudrock (Claystone & Mudstone)


Coal

Sedimentary Structures

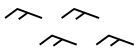
Ripple Laminations


Low-Angle Cross Bedding


High-Angle Cross Bedding


Wavy Laminations


Planar Laminations

Paleocurrent Measurements

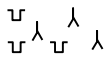
Rooting & Burrows


Convolute Bedding


Mudchip Rip-Up Clasts


Carbonaceous Material

Measured Section #1 : MS-01
Total footage: 192.5 ft

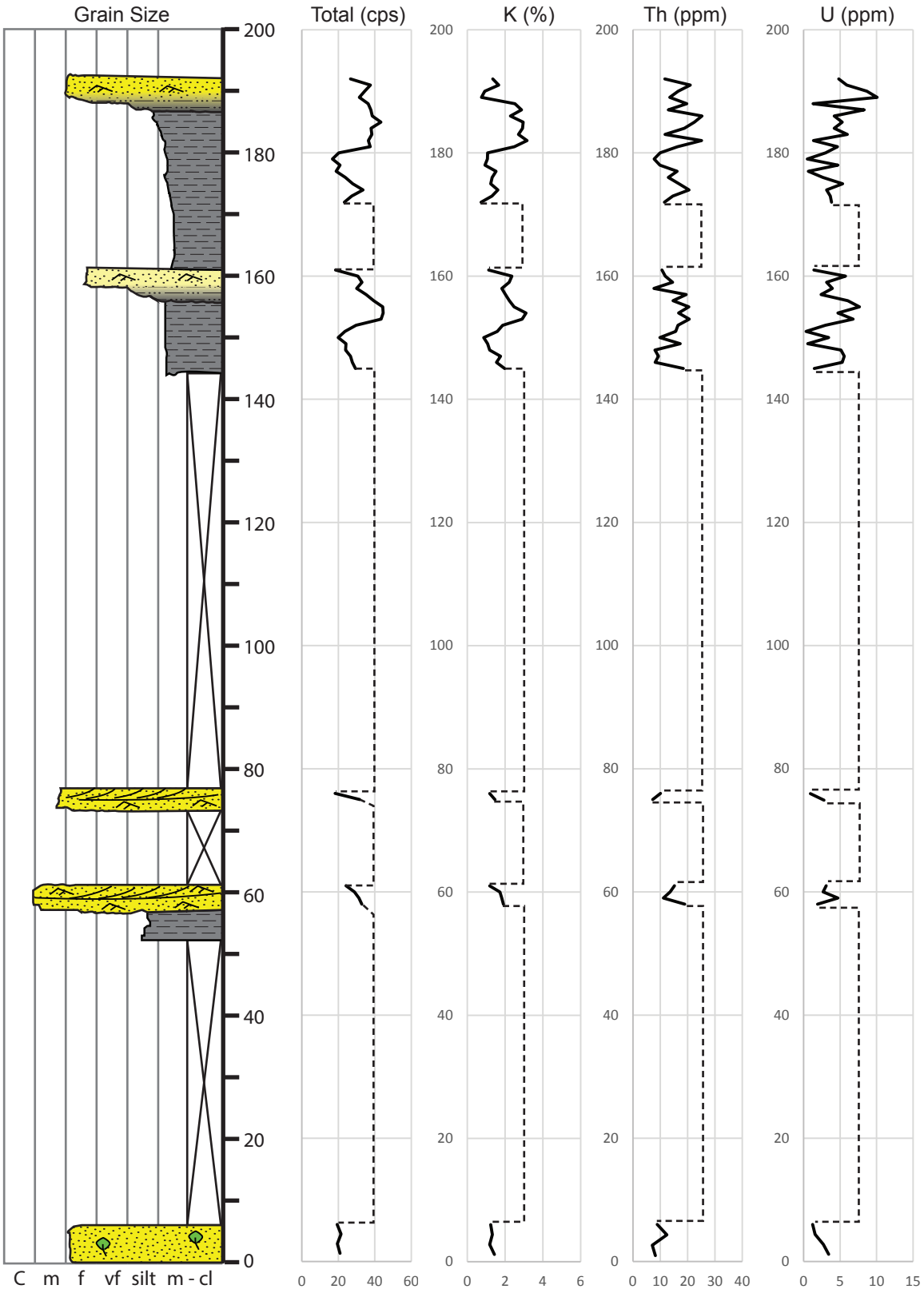

Measured Section #1 : MS-01
Units 4 & 5: Trench 2
Total footage: 46.0 ft

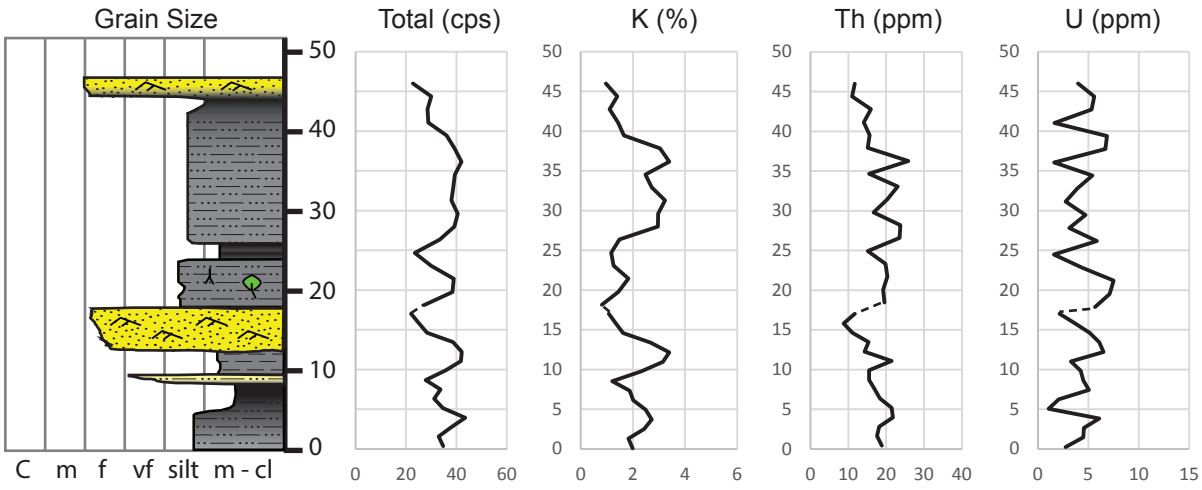

Measured Section #2 : MS-02
Total footage: 99.5 ft

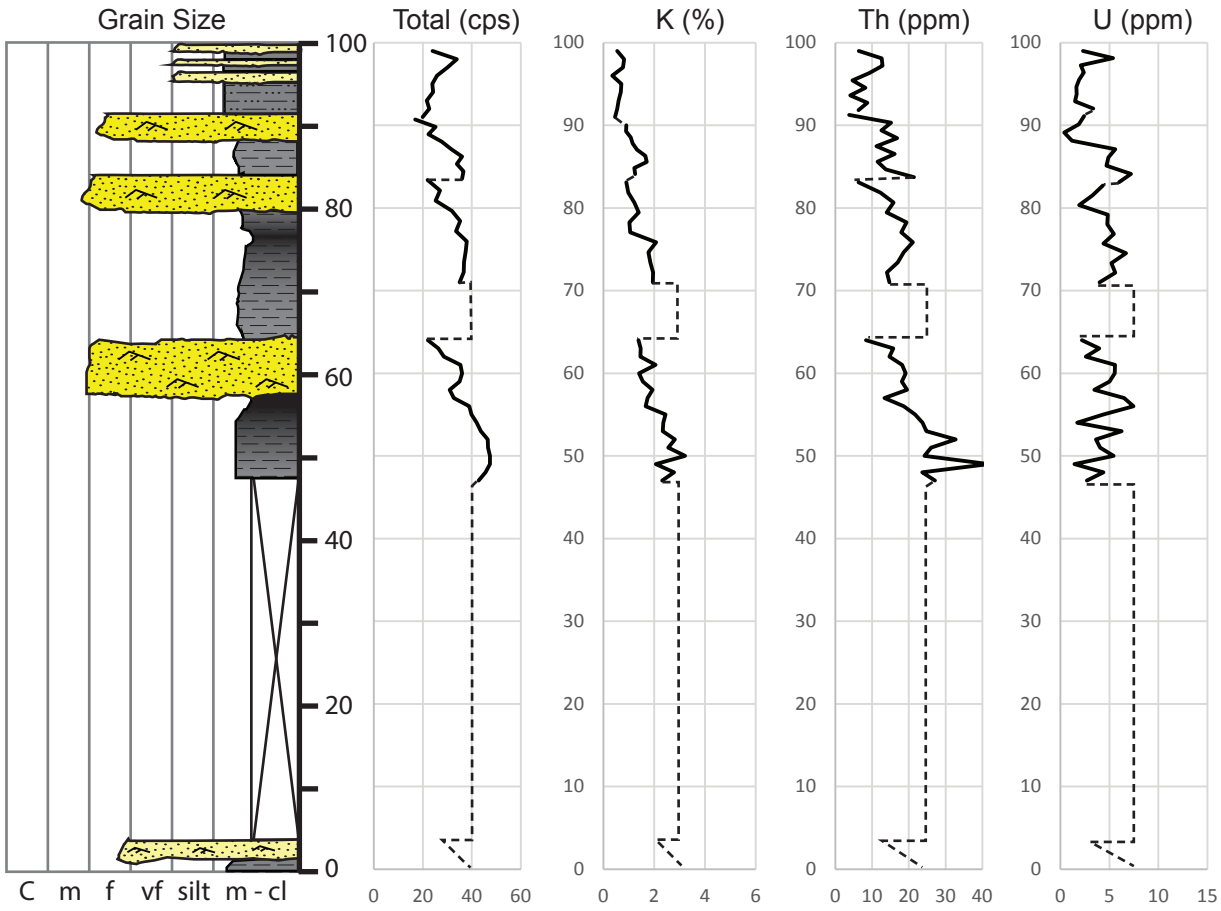

Measured Section #3 : MS-03
Total footage: 199.5 ft

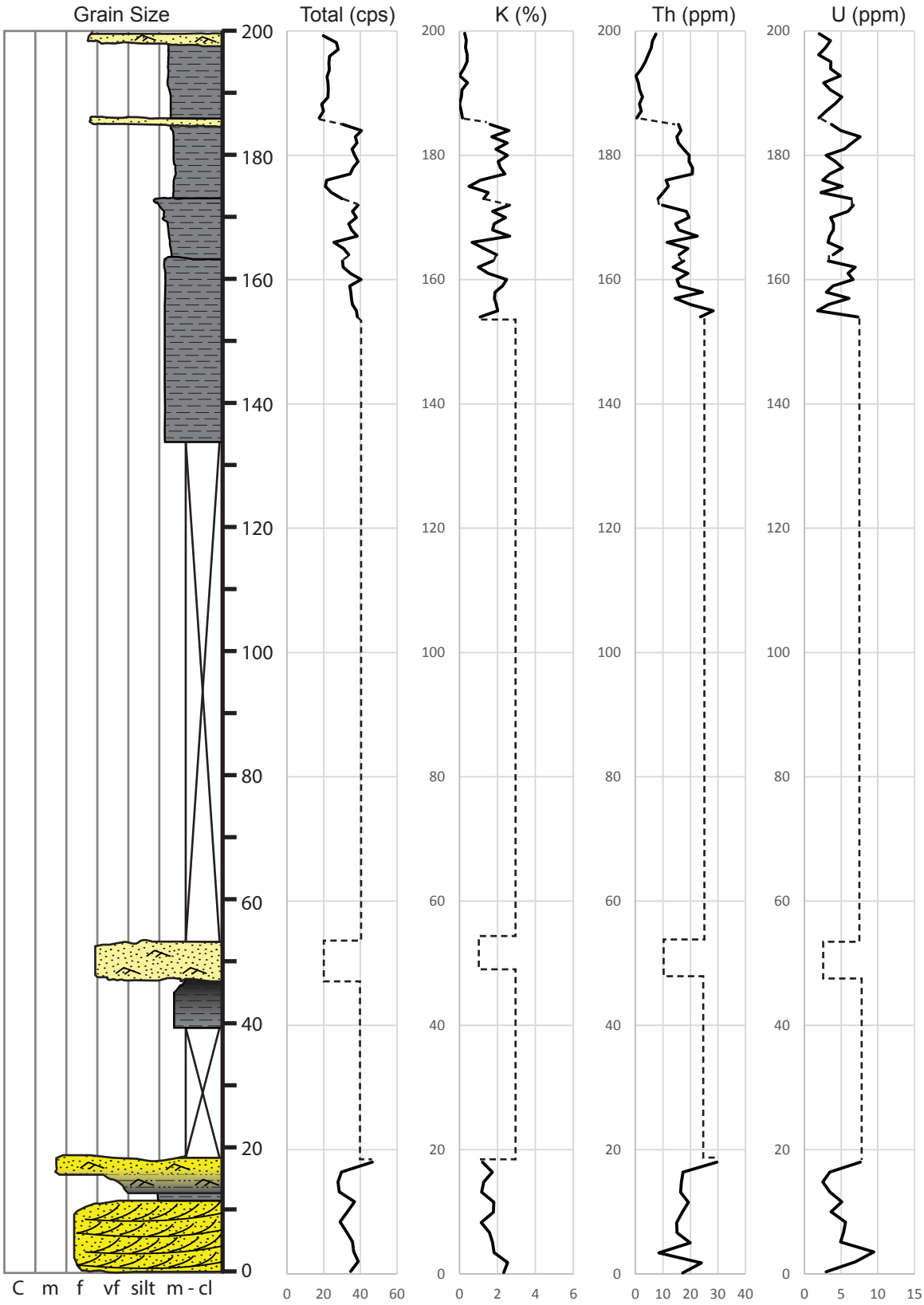

Measured Section #4 : MS-04
Total footage: 172.0 ft

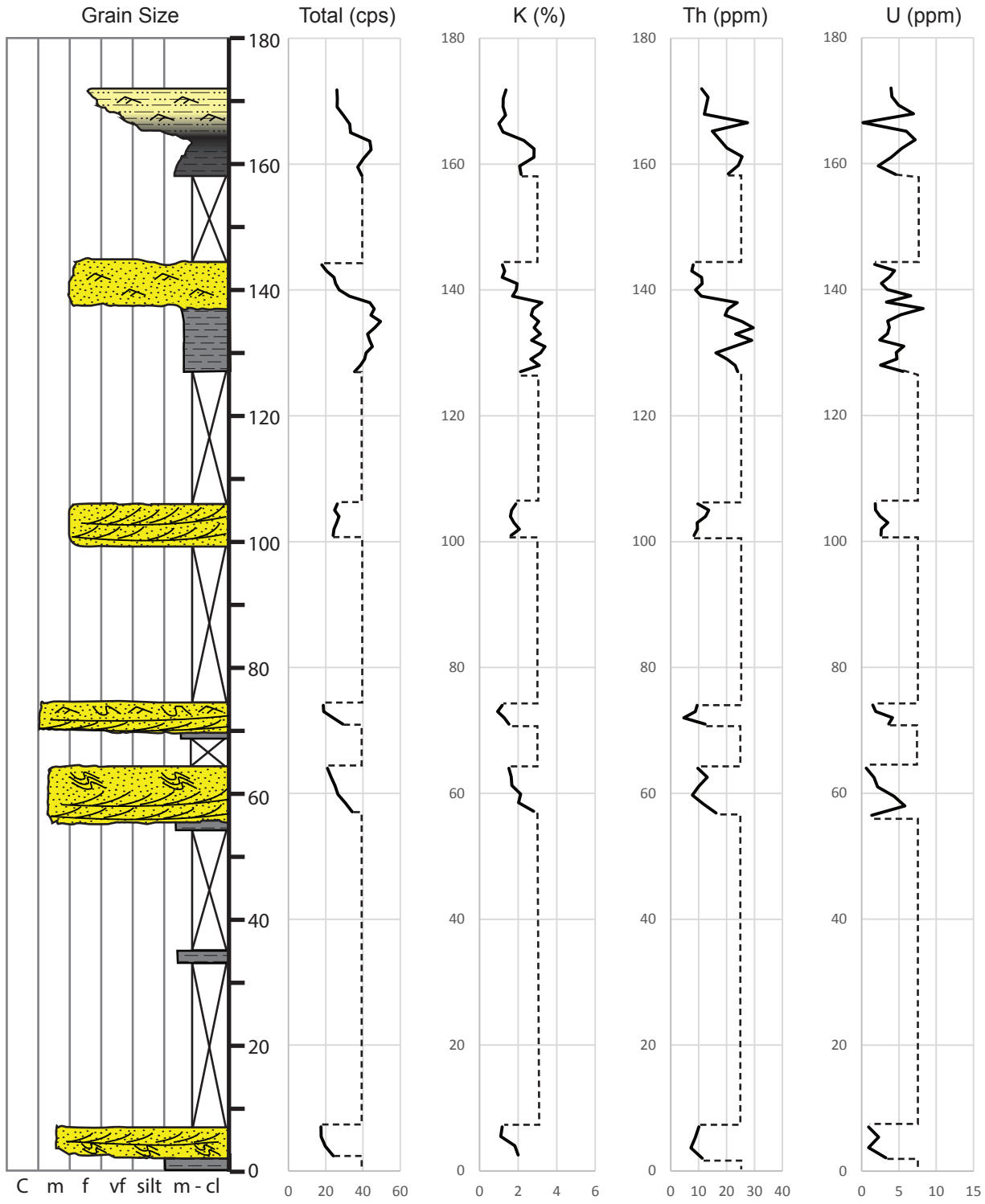

Measured Section - 01										
Unit	Unit 5 North		Unit 5 South		Unit 4 North		Unit 4 SE		Unit 3	
Interval (ft)	189-192'		188-192'		156-161'		156-161'		73-77'	
Type	App	Cor	App	Cor	App	Cor	App	Cor	App	Cor
Paleocurrent Measurements (degrees)	9	9.4	345	345.9	20	20	32	31.6	16	16.1
	18	18.1	336	337	12	12.3	9	9.4	45	44.2
	11	11.3	2	2.6	7	7.4	15	15.2	40	39.4
	337	338	7	7.4	8	8.4	25	24.8	13	13.2
	350	350.9	342	343	26	25.8	35	34.5		
	349	349.9	52	51.1	8	8.4	37	36.5		
	344	344.9	355	355.8	18	18.1	7	7.4		
	355	355.8	351	351.8	294	294.1	357	357.7		
	351	351.8	348	348.9	16	16.1	6	6.5		
	347	347.9	4	4.5	15	15.2	14	14.2		
	312	312.7	11	11.3	4	4.5	4	4.5		
	319	319.8	4	4.5	10	10.3	11	11.3		
	334	335	345	345.9						
			359	359.7						
			347	347.9						
			354	354.8						
			357	357.7						
			353	353.8						
			308	308.6						
			320	320.9						
			298	298.3						
N =	13		21		12		12		4	

App = apparent
Cor = corrected

Measured Section - 02								
Unit	Unit 4		Unit 5		Unit 5A		Unit 5B	
Interval (ft)	58-65'		80-84'		88-91'		95-99'	
Type	App	Cor	App	Cor	App	Cor	App	Cor
Paleocurrent Measurements (degrees)	2	1.6	350	349.9	290	290.6	302	302.6
	12	11.5	348	347.9	276	276.4	317	317.5
	6	5.6	11	10.5	2	1.6	312	312.6
	25	24.4	5	4.6	339	339.1	300	300.6
	14	13.5	110	110.6	298	298.6	318	318.5
	11	10.5	145	145.4	11	10.5	304	304.6
	14	13.5			324	324.4	295	295.6
	351	350.9			4	3.6		
	5	4.6			309	309.6		
	350	349.9			346	346		
	3	2.6			298	298.6		
	34	33.4						
	20	19.4						
	6	5.6						
	16	15.4						
	18	17.4						
N =	16		6		11		7	

App = apparent
Cor = corrected

Measured Section - 03						
Unit	"Base" sand		Unit 1-U		Unit 2	
Interval (ft)	0-11'		13-19'		47-53'	
Type	App	Cor	App	Cor	App	Cor
Paleocurrent Measurements (degrees)	6	5.9	6	5.9	315	315.5
	21	20.6	10	9.8		
	17	16.7	10	9.8		
	19	18.7	14	13.8		
	25	24.6	12	11.8		
	11	10.8				
	18	17.7				
	29	28.6				
	6	5.9				
	23	22.6				
	13	12.8				
	24	23.6				
	16	15.7				
	26	25.6				
	31	30.5				
	22	21.6				
	24	23.6				
	21	20.6				
	17	16.7				
	38	37.5				
N =	20		5		1	

App = apparent
Cor = corrected

Measured Section - 04						
Unit	Unit 4		Unit 5		Unit 5A	
Interval (ft)	137-144'		165-171'		171-172'	
Type	App	Cor	App	Cor	App	Cor
Paleocurrent Measurements (degrees)	14	13.5	29	28.4	116	116.6
	353	352.8	4	3.6	105	105.6
	12	11.5	8	7.5	130	130.6
	2	1.6			125	125.6
	32	31.4				
	20	19.4				
	13	12.5				
	39	38.4				
	15	14.4				
	25	24.4				
	32	31.4				
	29	28.4				
	9	8.5				
	29	28.4				
	4	3.6				
	34	33.4				
N =	16		3		4	

App = apparent
Cor = corrected

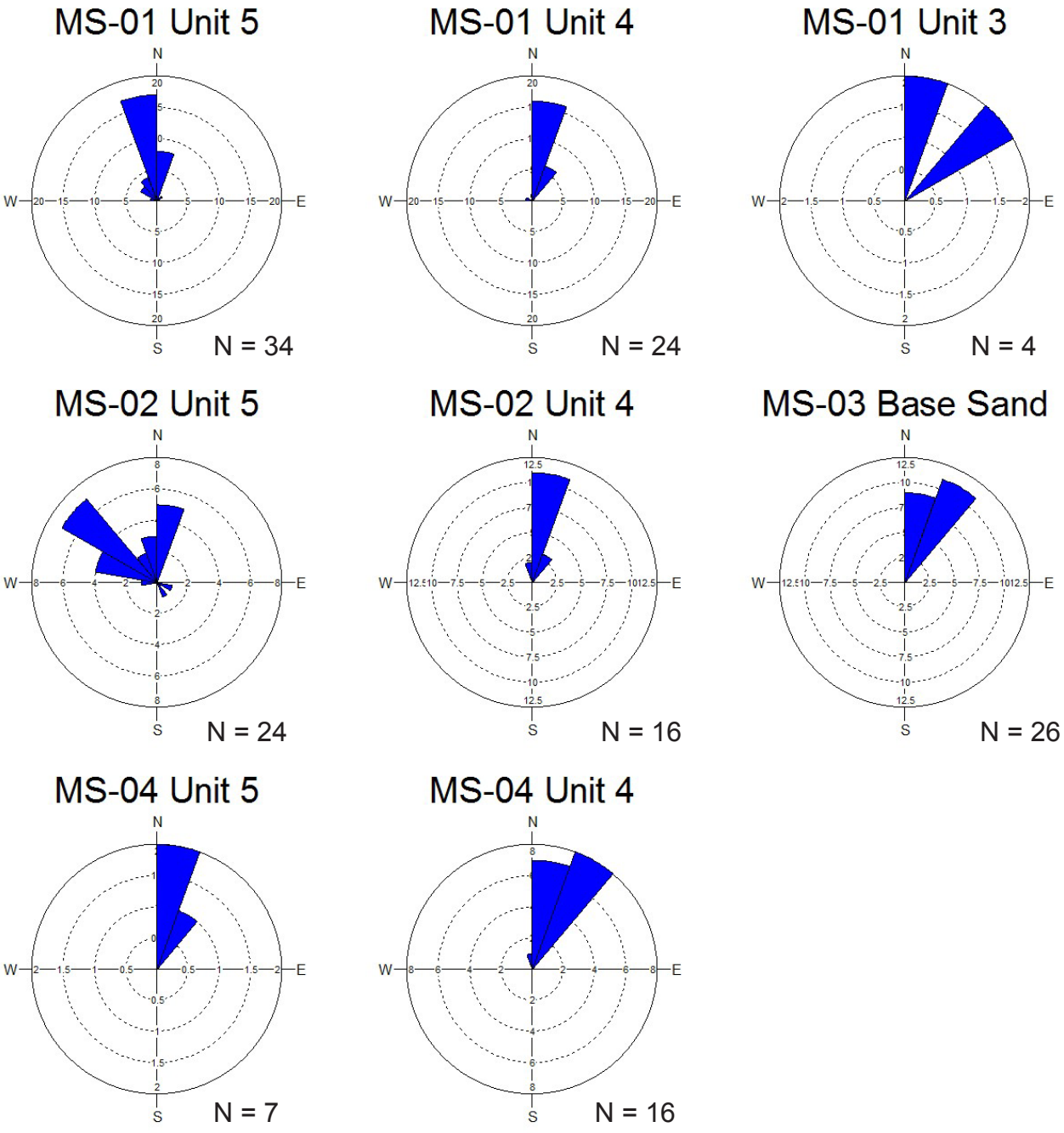

Rose diagrams of structurally uncorrected paleocurrent measurements obtained from ripple marks for each distinct unit in the measured sections. Plots made using Oriana 4 software.

Spectral Gamma Ray Data: Measured Section - 01						
ID	Footage (ft)	Total [cpm]	Total (cps)	K [%]	U [ppm]	Th [ppm]
Unit 1	3	1255.10	20.92	1.43	3.43	8.23
	4	1167.80	19.46	1.18	2.71	7.05
	5	1289.20	21.49	1.32	1.56	12.40
	6	1164.70	19.41	1.24	1.22	8.91
Unit 2	58	1976.50	32.94	1.91	1.92	18.92
	59	1880.20	31.34	1.82	4.71	11.15
	60	1729.00	28.82	1.72	2.67	13.59
	61	1456.20	24.27	1.18	3.10	15.18
Unit 3	75	1906.10	31.77	1.46	9.79	7.25
	76	1097.10	18.29	1.18	0.93	10.07
Unit 4	145	1762.10	29.37	1.98	1.45	18.38
	146	1664.80	27.75	1.54	5.28	8.14
	147	1603.70	26.73	1.76	5.58	9.34
	148	1441.10	24.02	1.18	5.11	8.07
	149	1455.60	24.26	1.07	0.57	17.30
	150	1199.30	19.99	0.87	3.44	9.85
	151	1421.00	23.68	1.58	0.33	15.61
	152	1786.80	29.78	1.87	2.98	16.48
	153	2610.40	43.51	2.90	6.77	20.60
	154	2679.50	44.66	3.11	4.70	16.71
	155	2665.90	44.43	2.48	7.64	20.45
	156	2362.70	39.38	2.23	6.06	14.66
	157	2113.40	35.22	2.02	2.39	19.50
	158	1806.70	30.11	1.82	3.95	7.71
	159	1981.70	33.03	2.22	3.16	14.50
	160	1845.00	30.75	2.36	5.75	11.79
	161	1106.60	18.44	1.13	1.40	10.62
Unit 5	172	1399.50	23.33	0.72	3.83	11.54
	173	1645.10	27.42	1.30	3.65	14.59
	174	2017.20	33.62	1.62	3.16	20.52
	175	1677.20	27.95	1.24	5.34	16.80
	176	1430.60	23.84	1.31	2.65	12.91
	177	1131.30	18.86	1.52	0.65	16.13
	178	1257.80	20.96	0.93	4.71	9.84
	179	1010.20	16.84	1.06	0.50	7.75
	180	1215.70	20.26	1.07	3.01	9.92
	181	2249.20	37.49	2.49	4.63	16.33
	182	2189.40	36.49	3.16	1.34	25.07
	183	2306.20	38.44	2.70	6.00	11.75
	184	2274.90	37.92	2.92	4.20	18.76
	185	2601.10	43.35	2.95	5.28	22.45
	186	2315.40	38.59	2.28	4.18	25.27
	187	2269.70	37.83	2.87	8.31	12.91
	188	2182.30	36.37	2.52	1.30	19.69
	189	1890.90	31.52	0.75	10.07	13.47
	190	2071.30	34.52	0.92	8.68	16.51
	191	2259.20	37.65	1.66	5.91	20.94
	192	1604.70	26.75	1.34	4.81	11.62
	3	2083.80	34.73	1.99	2.75	18.89
	4	1975.70	32.93	1.83	4.51	17.57
	5	2281.50	38.03	2.43	4.56	18.13

Unit 4, Trench 2	6	2604.70	43.41	2.72	6.08	21.77
	7	2076.20	34.60	2.49	1.06	21.44
	8	1868.90	31.15	2.01	2.06	18.35
	9	2022.30	33.71	1.88	5.07	16.96
	10	1668.20	27.80	1.21	4.51	15.50
	11	2141.30	35.69	2.32	4.25	15.49
	12	2508.10	41.80	3.15	3.28	21.46
	13	2525.80	42.10	3.40	6.51	14.33
	14	2314.60	38.58	2.67	6.07	15.35
	15	1695.90	28.27	1.62	5.14	11.08
	16	1510.40	25.17	1.35	3.70	8.78
	17	1318.60	21.98	1.07	2.15	11.72
Unit 5, Trench 2	29	1632.70	27.21	0.81	5.66	19.59
	30	2305.20	38.42	1.44	7.11	19.24
	31	2334.50	38.91	1.83	7.49	20.30
	32	1798.20	29.97	1.26	4.35	19.82
	33	1410.00	23.50	1.17	1.59	15.14
	34	2003.90	33.40	1.48	5.84	23.54
	35	2350.90	39.18	2.96	3.11	23.76
	36	2433.60	40.56	2.97	4.71	16.67
	37	2277.80	37.96	3.23	2.75	20.34
	38	2321.50	38.69	2.72	3.91	23.06
	39	2363.50	39.39	2.48	5.40	15.46
	40	2516.90	41.95	3.40	1.62	25.88
	41	2352.90	39.22	3.04	6.69	15.14
	42	2165.50	36.09	1.65	6.84	15.63
	43	1729.40	28.82	1.43	1.65	14.12
	44	1712.20	28.54	1.11	5.33	15.96
	45	1801.60	30.03	1.40	5.58	11.00
	46	1362.00	22.70	0.96	3.97	11.71

Spectral Gamma Ray Data: Measured Section - 02						
ID	Footage (ft)	Total [cpm]	Total (cps)	K [%]	U [ppm]	Th [ppm]
Unit 4	47	2569.20	42.82	2.32	2.69	27.13
	48	2735.40	45.59	2.78	4.38	23.64
	49	2841.10	47.35	2.07	1.44	41.72
	50	2846.50	47.44	3.22	5.43	24.26
	51	2799.20	46.65	2.55	4.05	26.07
	52	2790.10	46.50	2.82	3.63	32.77
	53	2620.20	43.67	2.34	6.26	24.81
	54	2520.60	42.01	2.36	1.72	23.71
	55	2392.90	39.88	2.44	4.40	21.72
	56	2340.00	39.00	1.66	7.46	18.65
	57	1961.60	32.69	1.74	6.49	13.35
	58	1859.50	30.99	1.93	3.47	19.50
	59	2097.50	34.96	1.55	5.01	18.06
	60	2159.90	36.00	1.40	5.55	19.16
	61	2118.90	35.32	2.05	5.58	18.14
	62	1713.50	28.56	1.46	2.60	14.70
	63	1578.80	26.31	1.47	3.96	15.77
	64	1322.50	22.04	1.38	2.19	8.30
Unit 5	71	2101.60	35.03	1.94	4.01	14.72
	72	2201.60	36.69	1.96	5.61	14.04
	73	2211.10	36.85	1.85	5.22	16.95
	74	2250.40	37.51	1.77	6.70	18.59
	75	2278.10	37.97	2.08	4.38	21.10
	76	2009.40	33.49	1.05	5.47	17.92
	77	2112.50	35.21	1.02	4.78	19.36
	78	1910.80	31.85	1.39	4.83	13.96
	79	1514.60	25.24	1.22	1.91	15.85
	80	1619.20	26.99	0.98	3.25	12.22
	81	1314.30	21.91	0.90	4.34	6.31
Unit 5A	82	2159.80	36.00	1.25	6.00	21.43
	83	2198.10	36.64	1.22	7.22	13.73
	84	2030.30	33.84	1.71	4.70	11.46
	85	2162.90	36.05	1.65	4.90	16.13
	86	1898.90	31.65	1.33	5.60	11.16
	87	1662.40	27.71	1.15	1.18	16.78
	88	1336.10	22.27	1.08	0.38	12.51
	89	1509.40	25.16	0.89	1.88	15.19
	90	1015.10	16.92	0.90	2.42	3.74
Unit 5B	91	1196.90	19.95	0.46	3.34	6.27
	92	1358.80	22.65	0.54	1.49	8.73
	93	1293.40	21.56	0.60	1.65	4.08
	94	1451.40	24.19	0.68	1.63	8.18
	95	1433.60	23.89	0.71	1.91	4.67
	96	1546.70	25.78	0.35	2.40	9.22
	97	1801.50	30.03	0.77	2.08	12.82
	98	2031.60	33.86	0.81	5.39	12.62
	99	1441.00	24.02	0.54	2.30	6.36

Spectral Gamma Ray Data: Measured Section - 03						
ID	Footage (ft)	Total [cpm]	Total (cps)	K [%]	U [ppm]	Th [ppm]
Unit 1	7	2081.40	34.69	2.33	2.96	17.20
	8	2334.40	38.91	2.54	6.94	23.99
	9	2185.40	36.42	1.82	9.46	8.52
	10	2143.30	35.72	1.74	4.93	19.97
	11	1946.60	32.44	1.58	5.34	15.13
	12	1735.20	28.92	1.15	5.59	15.01
	13	1976.70	32.95	1.79	3.63	17.04
	14	2212.20	36.87	1.81	5.10	19.29
	15	1707.60	28.46	1.17	3.46	16.40
	16	1671.10	27.85	1.28	2.50	16.72
	17	1782.00	29.70	1.73	3.47	17.30
	18	2792.10	46.54	1.21	7.62	29.65
Trench A	154	2300.80	38.35	1.09	7.28	23.64
	155	2273.50	37.89	2.02	1.79	28.28
	156	2141.20	35.69	1.94	3.28	20.01
	157	2107.00	35.12	1.84	6.07	14.48
	158	2089.20	34.82	1.87	2.99	24.35
	159	2054.60	34.24	2.27	3.88	15.97
	160	2426.00	40.43	2.48	6.64	15.14
	161	2072.50	34.54	1.51	5.95	19.15
	162	1836.80	30.61	0.99	6.94	13.73
	163	1815.00	30.25	1.75	3.27	17.63
Trench B	164	2019.00	33.65	1.96	3.91	15.89
	165	1854.40	30.91	1.30	5.14	19.15
	166	1532.20	25.54	0.67	3.22	11.56
	167	2297.20	38.29	2.65	3.44	22.50
	168	2118.20	35.30	1.74	3.93	15.85
	169	2018.80	33.65	1.83	3.96	14.61
	170	2270.20	37.84	2.43	3.59	19.53
	171	2140.70	35.68	1.74	5.95	18.51
	172	2325.40	38.76	2.64	6.67	9.79
Trench C	173	1805.30	30.09	1.28	6.39	8.26
	174	1453.60	24.23	1.51	2.26	10.08
	175	1258.30	20.97	0.50	5.15	11.98
	176	1296.60	21.61	1.11	2.50	11.13
	177	2064.60	34.41	2.40	3.45	20.68
	178	2161.60	36.03	2.16	5.18	20.81
	179	2321.90	38.70	2.04	4.23	19.48
	180	2214.90	36.92	2.53	2.96	19.59
	181	2125.90	35.43	1.92	5.43	17.57
	182	2291.50	38.19	2.52	6.49	15.69
	183	2238.60	37.31	1.70	7.61	15.03
	184	2440.90	40.68	2.60	4.95	16.57
	185	1825.10	30.42	1.61	3.70	15.65
Trench D	186	1053.90	17.57	0.16	1.97	0.47
	187	1198.90	19.98	0.09	2.98	2.13
	188	1133.60	18.89	0.00	4.17	1.44
	189	1335.20	22.25	0.10	5.11	2.58
	190	1354.00	22.57	0.13	3.54	1.53
	191	1341.60	22.36	0.43	2.63	1.07
	192	1307.30	21.79	0.00	4.89	0.23

	193	1386.10	23.10	0.23	3.59	2.13
	194	1370.60	22.84	0.40	3.61	3.55
	195	1392.40	23.21	0.40	1.94	4.60
	196	1677.40	27.96	0.32	2.87	5.77
	197	1613.20	26.89	0.36	3.56	6.23
	198	1191.00	19.85	0.27	2.03	7.47

Spectral Gamma Ray Data: Measured Section - 04						
ID	Footage (ft)	Total [cpm]	Total (cps)	K [%]	U [ppm]	Th [ppm]
Unit 1	4	1443.40	24.06	2.00	3.24	11.28
	5	1188.90	19.82	1.83	0.93	7.27
	6	1053.60	17.56	1.10	2.27	8.81
	7	1047.40	17.46	1.18	0.93	10.07
Unit 2A	59	2052.20	34.20	2.81	1.35	16.26
	60	1839.80	30.66	2.02	5.78	11.71
	61	1594.30	26.57	2.13	4.34	7.76
	62	1500.60	25.01	1.68	2.12	10.12
	63	1368.60	22.81	1.64	1.65	13.13
	64	1259.10	20.99	1.52	0.61	9.68
Unit 2B	71	1747.60	29.13	1.52	3.61	12.32
	72	1440.40	24.01	1.29	4.13	4.66
	73	1137.60	18.96	0.94	1.87	8.80
	74	1118.90	18.65	1.18	1.49	9.46
Unit 3	101	1440.80	24.01	1.63	2.58	8.33
	102	1464.50	24.41	2.07	2.65	9.60
	103	1550.70	25.85	1.79	3.51	9.48
	104	1630.80	27.18	1.60	2.43	12.50
	105	1488.40	24.81	1.67	1.85	13.63
	106	1570.90	26.18	1.88	1.81	9.75
Unit 4	127	2125.90	35.43	2.12	5.53	23.97
	128	2320.80	38.68	3.10	2.53	23.06
	129	2451.50	40.86	2.66	4.73	20.17
	130	2499.70	41.66	3.17	4.63	16.14
	131	2701.10	45.02	3.40	5.66	22.54
	132	2618.20	43.64	2.70	2.41	28.99
	133	2544.60	42.41	3.16	3.46	23.21
	134	2780.00	46.33	2.83	3.70	29.52
	135	2968.90	49.48	3.07	3.48	25.51
	136	2652.50	44.21	2.68	5.23	19.48
	137	2761.30	46.02	2.77	8.24	20.48
	138	2619.40	43.66	3.23	3.30	23.82
	139	1961.20	32.69	1.71	6.59	11.01
	140	1633.70	27.23	1.90	3.44	8.92
	141	1518.70	25.31	1.95	2.63	11.32
	142	1465.90	24.43	1.18	3.74	11.07
	143	1226.90	20.45	1.31	4.41	7.56
	144	1070.80	17.85	1.19	1.74	8.03
Unit 5	161	2364.60	39.41	2.16	4.56	20.57
	162	2229.30	37.16	2.08	2.22	24.19
	163	2426.70	40.45	2.82	3.97	25.60
	164	2662.30	44.37	2.83	5.36	20.14
	165	2623.50	43.73	2.30	7.17	17.52
	166	1998.70	33.31	1.22	5.98	14.88
	167	1969.80	32.83	1.00	0.17	27.55
	168	1776.60	29.61	1.35	6.94	12.06
	169	1565.30	26.09	1.22	4.94	12.74
	170	1571.70	26.20	1.23	4.05	13.39
	171	1560.10	26.00	1.37	3.92	11.10

Measured Section GPS Waypoints

WP #	Measured Section	Latitude (°)	Longitude (°)	Elevation (ft)	Description
22	MS-01	40.24944	-109.05189	5718	start of MS-01
24	MS-01	40.24987	-109.05233	5766	top of unit 2
25	MS-01	40.24990	-109.05308	5770	118.5 ft MS-01 path
26	MS-01	40.24991	-109.05344	5775	base unit 4
27	MS-01	40.24988	-109.05341	5794	top of unit 4 sand
28	MS-01	40.24993	-109.05359	5791	base unit 5, top unit 4; about 10 ft to north of trench
29	MS-01	40.24991	-109.05367	5801	contact between sand/shale in Unit 5, sharp
30	MS-01	40.24189	-109.05382	5800	top unit 5 sand; top MS-01
31	MS-01	40.24942	-109.05190	5729	base unit 1, MS-01
32	MS-01	40.24950	-109.05201	5735	first flag
33	MS-01	40.24960	-109.05209	5737	second flag
34	MS-01	40.24969	-109.05217		third flag
35	MS-01	40.24981	-109.05228	5754	4th flag; base of unit 2
36	MS-01	40.24985	-109.05231		5th flag, top unit 2
37	MS-01	40.24992	-109.05240	5777	6th flag & top of Unit 3
38	MS-01	40.24994	-109.05267	5770	7th flag, covered
39	MS-01	40.24989	-109.05293	5770	8th flag
40	MS-01	40.24986	-109.05314	5768	9th flag
41	MS-01	40.24982	-109.05343	5779	10th flag, base of Unit 4, base of trench (ant hill!)
42	MS-01	40.24991	-109.05363	5778	11th flag, top of Unit 4, base of Unit 5 shale, ~10 ft north of trench
43	MS-01	40.24987	-109.05370	5781	12th flag, contact w/ SS/SH in Unit 5
44	MS-01	40.24986	-109.05386	5785	13th, top of Unit 5 and top of MS-01
45	MS-01, Trench 2	40.25003	-109.05383	5782	Trench 2, Unit 5, TOP
46	MS-01, Trench 2	40.25008	-109.05370		Trench 2, Unit 5, BASE
47	MS-01, Trench 2	40.25024	-109.05388	5768	Trench 2, Unit 4, TOP
48	MS-01, Trench 2	40.25027	-109.05387	5756	Trench 2, Unit 4, BASE
49	MS-02	40.24812	-109.05144	5720	BASE MS-02
50	MS-02	40.24809	-109.05148	5807	MS02 path after 2nd eyeheight (EH)
51	MS-02	40.24870	-109.05166	5882	MS02 path after 7th EH

52	MS-02	40.24804	-109.05175	5836	MS02 path after 9th EH; traverse over to trench, base of unit 4
53	MS-02	40.24791	-109.05170	5832	traverse from last flag to base of trench U4
54	MS-02	40.24789	-109.05176	5860	top of Unit 4, on top of sand below trench
55	MS-02	40.24779	-109.51730	5870	top of Unit 4, traverse over to trench (consistent with dip direction)
56	MS-02	40.24779	-109.05193	5870	after 6th tally in unit 5
57	MS-02	40.24780	-109.05201	5889	top of MS-02; Unit 6
58	MS-03	40.25338	-109.05573	5680	BASE of MS-03, white sandstone
59	MS-03	40.25343	-109.05581	5695	top of white sand, unit 1
60	MS-03	40.25349	-109.05644	5681	MS03 path from covered to unit 2
61	MS-03	40.25420	-109.05659		traversed to base of U2
62	MS-03	40.25431	-109.05699	5669	MS03 path; flagging after 3rd EH
63	MS-03	40.25447	-109.05762	5673	MS03 path after 10th EH
64	MS-03	40.25462	-109.05811		MS03 path after 18th EH; end covered, start of trenches
65	MS-03	40.25463	-109.05854	5714	MS03 END; at top of Unit C "shale mound"
66	MS-03	40.25261	-109.05647	5689	drainage where Unit 2 better exposed
3	MS-04	40.24491	-109.04878	5783	base, 1st flag
4	MS-04	40.24473	-109.04897	5828	2nd flag
5	MS-04	40.24481	-109.04908	5836	3rd flag
6	MS-04	40.24471	-109.04922	5837	4th flag;
7	MS-04	40.24467	-109.04930	5847	5th flag
8	MS-04	40.24458	-109.04952	5886	6th flag
9	MS-04	40.24455	-109.04982	5860	7th flag
10	MS-04	40.24458	-109.04988	5867	Top MS-04
68	Castlegate Traverse	40.26505	-109.05457	5807	
69	Castlegate Traverse	40.26316	-109.05332	5824	
70	Castlegate Traverse	40.26213	-109.05268	5860	
71	Castlegate Traverse	40.26053	-109.05180	5815	
72	Castlegate Traverse	40.25949	-109.05098		
73	Castlegate Traverse	40.25788	-109.05003	5820	road up to hogback
74	Castlegate Traverse	40.25585	-109.04816	5873	
75	Castlegate Traverse	40.25372	-109.04609	5958	

Appendix C

MPS Training Images

Appendix C contains the results from 38 trial runs during search-mask testing to produce the multi-point facies pattern that best replicates the respective training image. Training images were systematically tested on unconditioned models, each time varying one of the following parameters: grid size, channel orientation, search-mask size (I, J, and K radius), number of multi-grids, maximum number of informed nodes, and trust fraction strength. Output models were visually inspected and compared to the respective training image with the goal of best reproducing the training images global architectural element proportions and object geometry, continuity, and dimensions. Table C2 has information for the 10 wells used in the MPS modeling in Petrel (Schlumberger). Figures C1 – C6 show the final training images used for each zone in the MPS process.

Trial	Grid Size	Channel Orientation	Search Mask		Multi-Grids	Informed Nodes	Trust Fraction Strength	Use Fractions from Pattern?	Facies Proportions	Description
			Shape	Size						
1	126 x 85 x 100	E-W	ellipsoid	12 x 10 x 2	2	64	0.5	N	Poor	smooth channel edges, but discontinuous
2	126 x 85 x 100	E-W	ellipsoid	5 x 5 x 5	2	64	0.5	N	Poor	patchy channels, highly discontinuous
3	126 x 85 x 100	E-W	ellipsoid	10 x 10 x 5	2	64	0.5	N	Poor	pixelated and patchy channels
4	126 x 85 x 100	E-W	ellipsoid	5 x 5 x 2	2	64	0.5	N	Poor	pixelated, discontinuous channels; poor vertical continuity
5	126 x 85 x 100	E-W	ellipsoid	20 x 20 x 20	2	64	0.5	N	Poor	thicker channels, better continuity but still choppy
6	126 x 85 x 100	E-W	ellipsoid	12 x 10 x 2	2	64	0.9	N	Poor	patch channels, one large crevasse splay
7	126 x 85 x 100	E-W	ellipsoid	12 x 10 x 2	4	64	0.9	N	Poor	better channel continuity, large crevasse splays, long run time
8	126 x 85 x 100	E-W	ellipsoid	12 x 10 x 2	4	64	0.5	Y	Poor	Poor channel continuity, very little crevasse splay
9	126 x 85 x 100	E-W	ellipsoid	12 x 10 x 2	4	64	0.9	Y	Moderate	discontinuous channels, fan like crevasse splays
10	126 x 85 x 100	E-W	ellipsoid	16 x 12 x 4	2	64	0.5	N	Poor	only one continuous channel
11	126 x 85 x 100	E-W	ellipsoid	10 x 10 x 2	2	64	0.5	N	Poor	thinner channels, does not replicate training image dimensions
12	126 x 85 x 100	E-W	ellipsoid	24 x 36 x 4	2	64	0.5	Y	Poor	thin moderately continuous channels
13	247 x 93 x 10	E-W	ellipsoid	10 x 12 x 2	2	64	0.5	N	Good	pixelated, moderately continuous chanenls, choppy splays
14	126 x 85 x 100	E-W	ellipsoid	10 x 12 x 2	2	64	0.5	Y	Good	much better facies reproduction on same grid size as Zone 1
15	126 x 85 x 100	E-W	ellipsoid	10 x 12 x 2	2	64	0.5	N	Good	better channel continuity, slightly pixelated
16	247 x 93 x 10	E-W	ellipsoid	12 x 10 x 2	2	16	0.5	N	Good	pixelated still, but better continuity
17	247 x 93 x 10	E-W	ellipsoid	20 x 24 x 4	2	16	0.5	N	Good	better channel continuity, splays fan shaped
18	247 x 93 x 10	E-W	ellipsoid	20 x 24 x 10	2	16	0.5	N	Good	best continuity so far

19	247 x 93 x 10	E-W	ellipsoid	20 x 24 x 4	2	64	0.5	N	Good	slightly pixelated, but overall good channel and crevasse splay reproduction
20	247 x 93 x 10	E-W	ellipsoid	20 x 24 x 4	4	16	0.5	N	Moderate	very pixelated, discontinous
21	247 x 93 x 10	E-W	ellipsoid	20 x 24 x 4	4	64	0.5	N	Moderate	more pixelated than previous simulation, patchy
22	126 x 85 x 100	E-W	ellipsoid	20 x 24 x 4	2	64	0.5	N	Good	discontinous channels, thin splays in the E-W direction
23	247 x 93 x 10	E-W	ellipsoid	24 x 36 x 10	2	64	0.5	N	Moderate	very good channel continuity
24	247 x 93 x 10	E-W	ellipsoid	36 x 24 x 10	2	64	0.5	N	Moderate	decent channel continuity, slighly pixelated
25	247 x 93 x 10	E-W	ellipsoid	24 x 36 x 4	2	64	0.5	N	Good	good channel continuity
26	247 x 93 x 10	E-W	ellipsoid	45 x 60 x 4	2	64	0.5	N	Moderate	Good channel continuity, slightly pixelated splays
27	247 x 93 x 10	E-W	ellipsoid	24 x 36 x 2	2	64	0.5	N	Moderate	discontiuous channels, patchy splays
28	247 x 93 x 10	E-W	ellipsoid	24 x 36 x 2	2	64	0.9	Y	Excellent	continuous channels, fan shaped splays - best so far
29	247 x 93 x 10	E-W	ellipsoid	24 x 30 x 4	2	64	0.9	Y	Excellent	patchier channels/splays than previous simulation
30	126 x 85 x 100	E-W	ellipsoid	24 x 30 x 4	2	64	0.9	Y	Excellent	best channel continuity so far, best splays
31	247 x 93 x 10	E-W	ellipsoid	24 x 30 x 4	2	64	0.9	Y	Good	slightly discontinuous, pixelated
32	247 x 93 x 10	E-W	ellipsoid	30 x 30 x 4	2	64	0.9	Y	Poor	poor facies proportion reproduction
33	247 x 93 x 10	E-W	ellipsoid	24 x 32 x 4	2	64	0.9	Y	Poor	poor facies proportion reproduction
34	247 x 93 x 10	E-W	ellipsoid	20 x 24 x 4	2	64	0.9	Y	Good	decent continuity, thinner channels, good proportion
35	157 x 177 x 30	N-S (22°)	ellipsoid	24 x 30 x 4	2	64	0.9	Y	Excellent	long run time, channels slightly discontinous
36	157 x 177 x 30	N-S (22°)	ellipsoid	30 x 24 x4	2	64	0.9	Y	Excellent	moderate channel continuity and proportion reproductions
37	157 x 177 x 30	N-S (22°)	ellipsoid	12 x 10 x4	2	64	0.9	Y	Good	patchy, poor continuity
38	**157 x 177 x 30**	**N-S (22°)**	**ellipsoid**	**40 x 30 x 8**	**2**	**64**	**0.9**	**Y**	**Excellent**	**longest run time, but best continuity and fan shaped splays**

Table C1. Results from 38 trial runs of search mask testing on training images. Parameters were varied and unconditioned models were visually inspected and compared to the respective training image.

MPS Modeling Wells									
API Number	**Well Name**	**Operator**	**Section**	**Township**	**Range**	**Latitude**	**Longitude**	**County**	**KB (ft)**
43047152750000	RW 32-26B	QEP ENERGY COMPANY	26	7S	23E	40.18230	-109.29148	Uintah	5553
43047152900000	RW 23-26B	QEP ENERGY COMPANY	26	7S	23E	40.17880	-109.29603	Uintah	5521
43047305210000	RW 33-26B	QEP ENERGY COMPANY	26	7S	23E	40.17873	-109.29132	Uintah	5547
43047522380000	RW 9C1-26B	QEP ENERGY COMPANY	26	7S	23E	40.17883	-109.28712	Uintah	5581
43047519030000	RW 12C3-25B	QEP ENERGY COMPANY	25	7S	23E	40.17739	-109.28360	Uintah	5624
43047519050000	RW 12D4-25B	QEP ENERGY COMPANY	25	7S	23E	40.17783	-109.28007	Uintah	5634
43047519040000	RW 12D1-25B	QEP ENERGY COMPANY	25	7S	23E	40.17874	-109.28007	Uintah	5637
43047305200000	RW 44-26B	QEP ENERGY COMPANY	26	7S	23E	40.17459	-109.28641	Uintah	5584
43047151480000	RW 34-26B	QEP ENERGY COMPANY	26	7S	23E	40.17538	-109.29140	Uintah	5559
43047305180000	RW 24-26B	QEP ENERGY COMPANY	26	7S	23E	40.17499	-109.29603	Uintah	5521

Table C2. Information for the 10 wells used in the MPS modeling process.

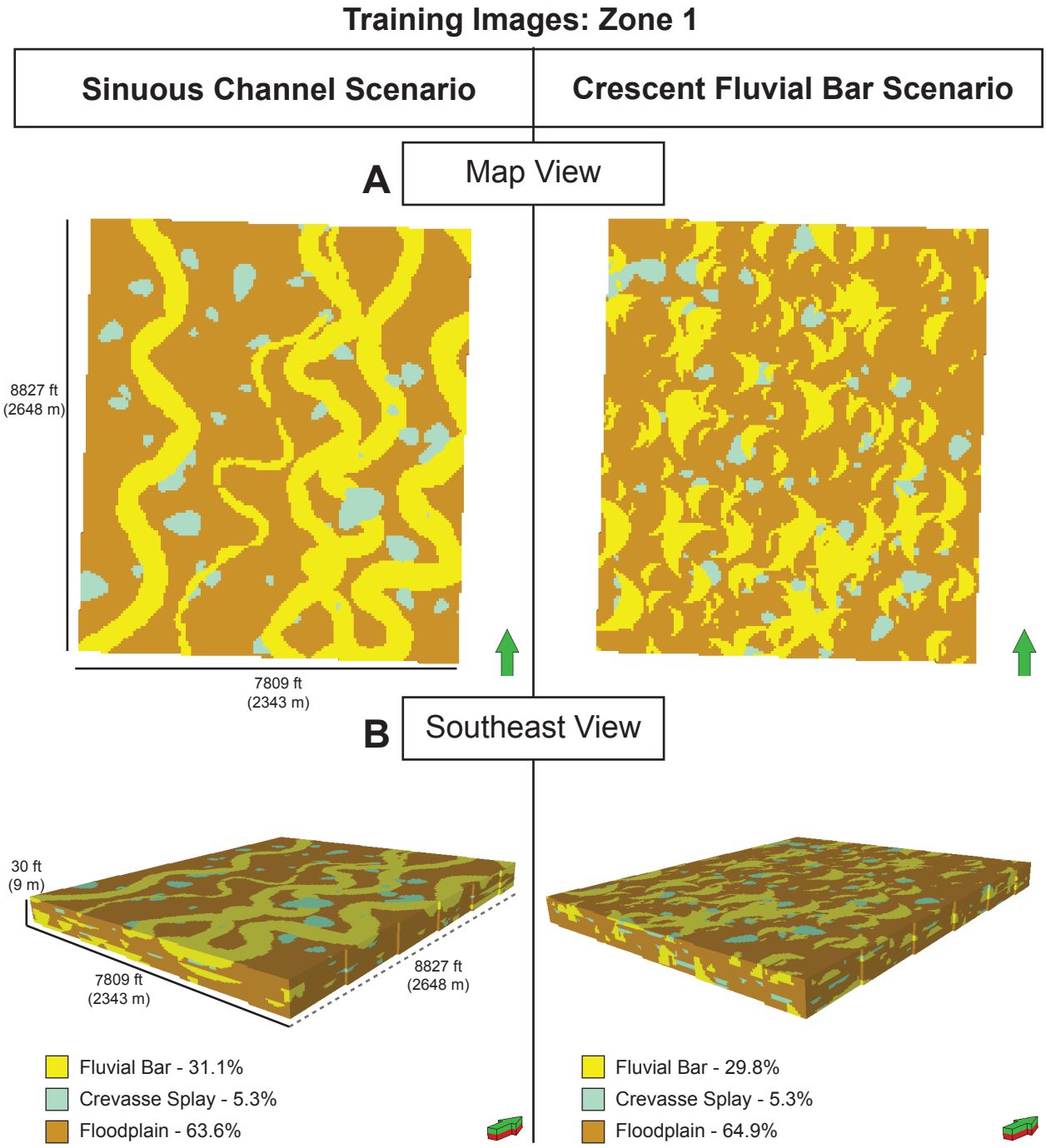

Figure C1. Training images generated by object-based modeling in (A) mapview and a view from the southeast (B) for Zone 1. The sinuous channel scenario used a channel shape to represent fluvial bars, while a crescent shape for fluvial bars was used for the other end member scenario. Each training image measured 7809 ft x 8827 ft x 30 ft (2343 m x 2648 m x 9 m) and each cell measured 50 ft x 50 ft x 1 ft (15 m x 15 m x 0.3 m). Zone 1 is strategraphically the highest within the interval.

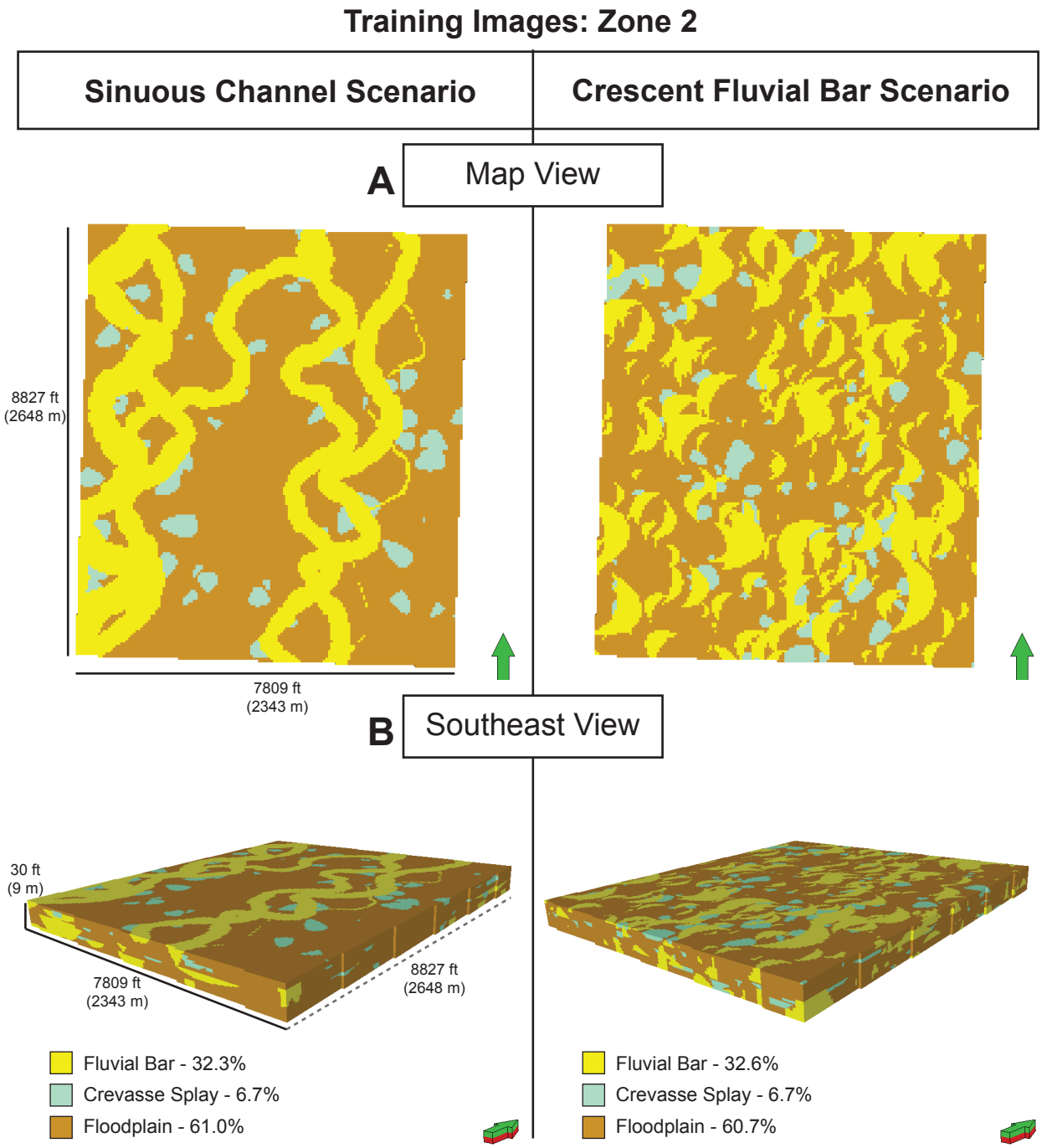

Figure C2. Training images generated by object-based modeling in (A) mapview and a view from the southeast (B) for Zone 2. The sinuous channel scenario used a channel shape to represent fluvial bars, while a crescent shape for fluvial bars was used for the other end member scenario. Each training image measured 7809 ft x 8827 ft x 30 ft (2343 m x 2648 m x 9 m) and each cell measured 50 ft x 50 ft x 1 ft (15 m x 15 m x 0.3 m).

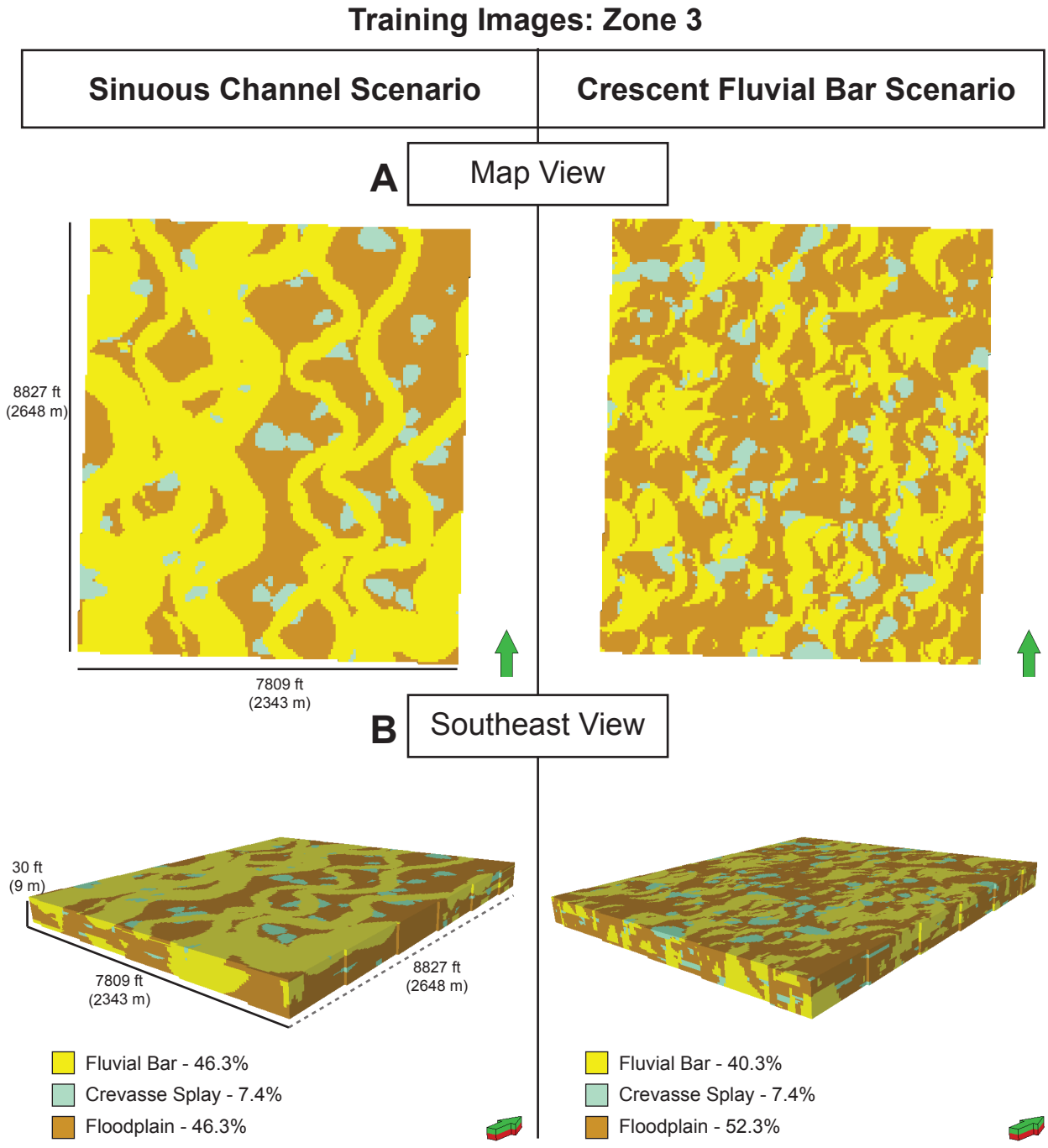

Figure C3. Training images generated by object-based modeling in (A) mapview and a view from the southeast (B) for Zone 3. The sinuous channel scenario used a channel shape to represent fluvial bars, while a crescent shape for fluvial bars was used for the other end member scenario. Each training image measured 7809 ft x 8827 ft x 30 ft (2343 m x 2648 m x 9 m) and each cell measured 50 ft x 50 ft x 1 ft (15 m x 15 m x 0.3 m).

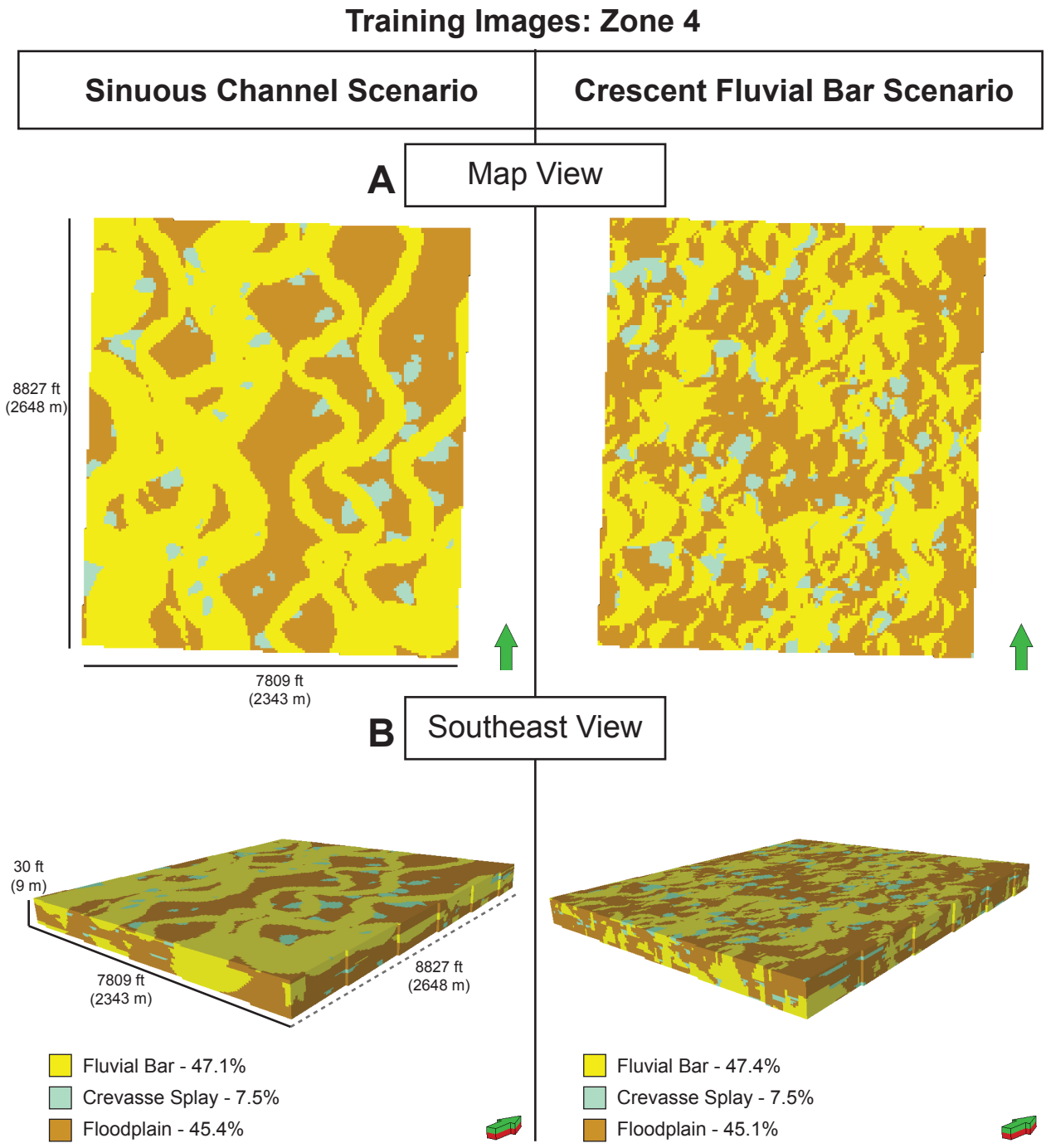

Figure C4. Training images generated by object-based modeling in (A) mapview and a view from the southeast (B) for Zone 4. The sinuous channel scenario used a channel shape to represent fluvial bars, while a crescent shape for fluvial bars was used for the other end member scenario. Each training image measured 7809 ft x 8827 ft x 30 ft (2343 m x 2648 m x 9 m) and each cell measured 50 ft x 50 ft x 1 ft (15 m x 15 m x 0.3 m).

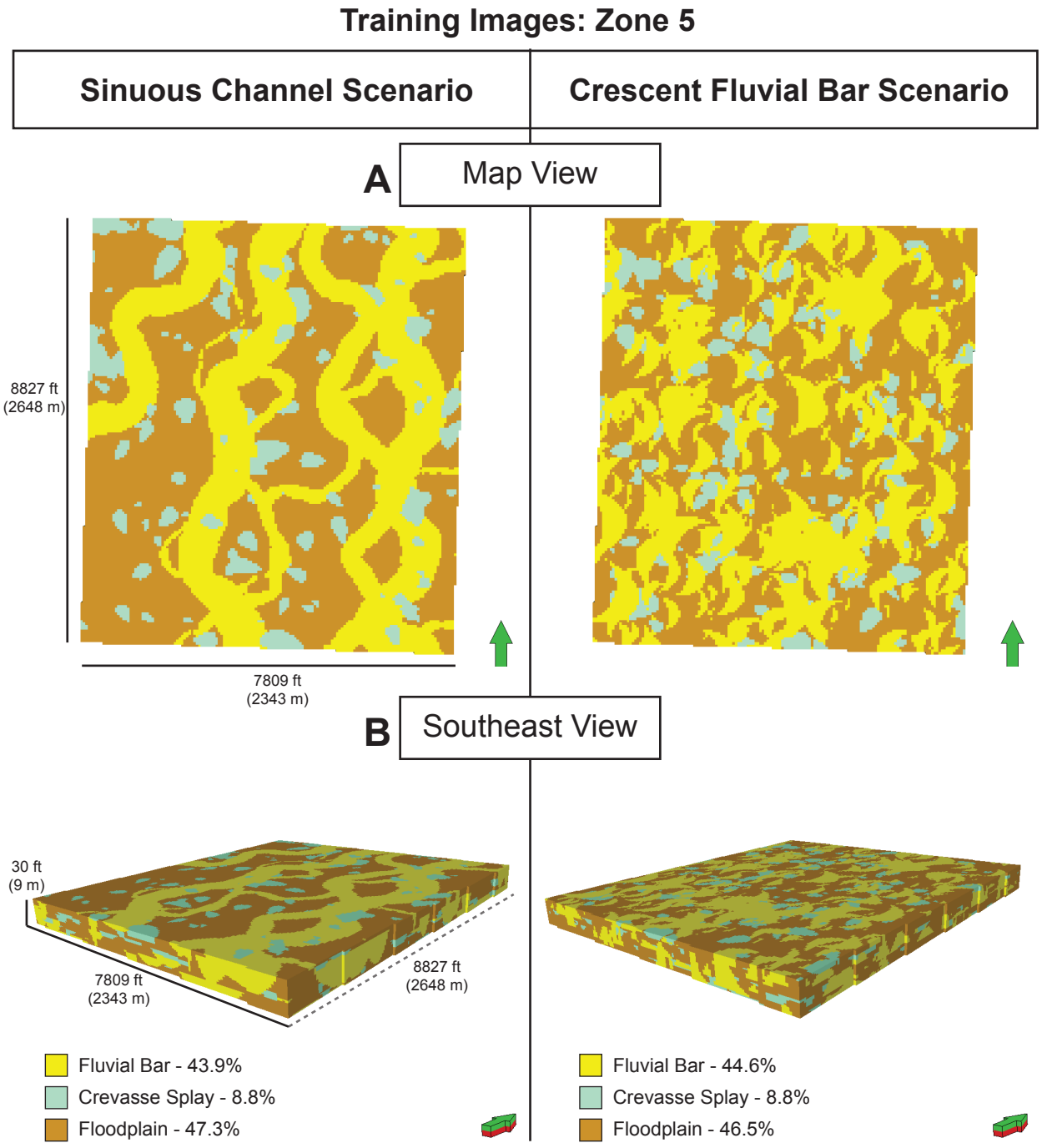

Figure C5. Training images generated by object-based modeling in (A) mapview and a view from the southeast (B) for Zone 5. The sinuous channel scenario used a channel shape to represent fluvial bars, while a crescent shape for fluvial bars was used for the other end member scenario. Each training image measured 7809 ft x 8827 ft x 30 ft (2343 m x 2648 m x 9 m) and each cell measured 50 ft x 50 ft x 1 ft (15 m x 15 m x 0.3 m).

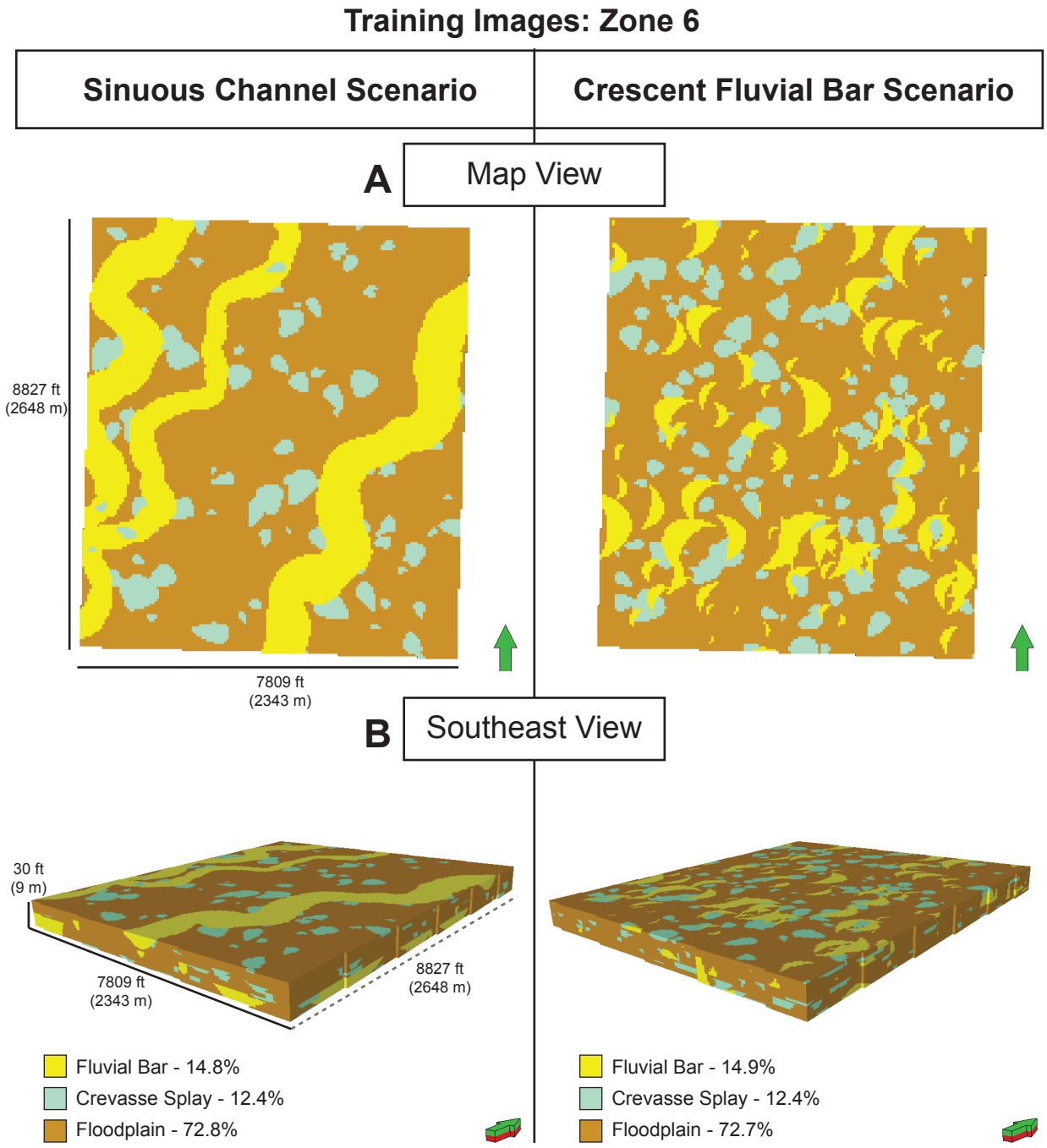

Figure C6. Training images generated by object-based modeling in (A) mapview and a view from the southeast (B) for Zone 6. The sinuous channel scenario used a channel shape to represent fluvial bars, while a crescent shape for fluvial bars was used for the other end member scenario. Each training image measured 7809 ft x 8827 ft x 30 ft (2343 m x 2648 m x 9 m) and each cell measured 50 ft x 50 ft x 1 ft (15 m x 15 m x 0.3 m). Zone 6 is strategraphi-

Appendix D

Static Connectivity Tables and Supplemental Material

Appendix D contains tables for well-based static connectivity for the two MPS models. Connected sandstone volumes were generated in Petrel 2010.2 (Schlumberger) using the current well spacing (approximately 40-ac spacing) and pseudo well spacing patterns at 160-ac, 40-ac, 10-ac, and 2.5-ac. Connectivity was then calculated by dividing the connected volume of "sandstone" grid cells by the total volume of "sandstone" grid cells in the model domain. Information on the petrophysical properties derived from core and the porosity modeling is also included in this appendix.

Well-Based Static Sandstone Connectivity: Entire Model Volume						
Scenario	Well Spacing	Number of Wells	Fluvial Bar Connectivity (%)		Sandstone Connectivity (%)- Fluvial Bars & Splays	
			Reservoir	Total	Reservoir	Total
Sinuous Channel (MPS)	Current	10	51.43	70.22	60.49	86.36
	160-ac	3	50.22	69.53	56.13	82.72
	40-ac	12	52.08	71.13	61.62	89.44
	10-ac	54	53.35	71.58	68.09	95.27
	2.5-ac	228	53.96	71.56	68.83	96.13
Crescent-Shaped Fluvial Bar (MPS)	Current	10	50.46	68.25	56.77	80.39
	160-ac	3	49.00	66.25	53.63	77.13
	40-ac	12	50.81	69.56	58.38	85.45
	10-ac	54	52.41	70.81	65.70	92.56
	2.5-ac	228	53.39	71.65	66.38	93.43

Table D1. Well-based static connectivity for both MPS models. Fluvial bar connectivity is defined as the connected sandstone volume attribute to exclusively fluvial bars, while sandstone connectivity includes both fluvial bars and crevasse splays as contributors to connectivity.

Well-Based Static Connectivity by Zone: Sinuous Channel Scenario (MPS)						
Zone	Well Spacing	Number of Wells	Fluvial Bar Connectivity (%)		Sandstone Connectivity (%)- Fluvial Bars & Splays	
			Reservoir	Total	Reservoir	Total
1	Current	10	60.88	70.90	64.59	80.31
	160-ac	3	55.60	70.70	59.79	77.97
	40-ac	12	65.24	71.36	73.55	84.78
	10-ac	54	69.29	71.93	86.30	93.76
	2.5-ac	228	71.25	72.23	93.06	79.59
2	Current	10	67.86	67.62	84.23	88.11
	160-ac	3	69.45	69.67	75.23	86.26
	40-ac	12	67.97	69.85	85.76	91.83
	10-ac	54	70.19	70.36	93.16	95.34
	2.5-ac	228	70.58	70.67	97.73	98.88
3	Current	10	75.23	75.66	92.04	92.83
	160-ac	3	75.22	75.65	85.41	86.07
	40-ac	12	74.31	75.68	90.62	92.22
	10-ac	54	75.35	75.77	96.23	96.90
	2.5-ac	228	76.00	75.99	98.82	98.97
4	Current	10	78.77	78.33	86.82	89.33
	160-ac	3	78.77	78.33	85.19	86.06
	40-ac	12	79.28	78.85	85.41	91.20
	10-ac	54	79.31	78.88	96.15	96.67
	2.5-ac	228	79.40	78.93	98.61	98.87
5	Current	10	75.62	75.78	87.52	90.05
	160-ac	3	75.62	75.78	87.13	88.50
	40-ac	12	75.65	75.78	88.23	90.80
	10-ac	54	76.68	75.89	94.08	96.75
	2.5-ac	228	77.18	76.26	96.75	98.67
6	Current	10	23.39	36.33	45.54	73.35
	160-ac	3	4.77	26.84	19.56	67.59
	40-ac	12	29.40	40.11	56.94	84.53
	10-ac	54	36.42	40.11	79.37	92.97
	2.5-ac	228	40.43	43.31	93.18	98.31

Table D2. Well-based static connectivity by zone for the sinuous channel MPS model.

Well-Based Static Connectivity by Zone: Crescent-Shaped Fluvial Bar Scenario (MPS)						
Zone	Well Spacing	Number of Wells	Fluvial Bar Connectivity (%)		Sandstone Connectivity (%)- Fluvial Bars & Splays	
			Reservoir	Total	Reservoir	Total
1	Current	10	58.52	68.96	62.39	75.82
	160-ac	3	50.31	68.97	53.69	74.95
	40-ac	12	57.89	69.02	64.66	82.54
	10-ac	54	64.68	70.47	82.00	92.18
	2.5-ac	228	68.85	71.80	90.45	96.70
2	Current	10	69.04	70.76	75.65	80.58
	160-ac	3	68.92	70.68	74.42	76.17
	40-ac	12	69.50	71.24	77.67	84.37
	10-ac	54	70.04	71.30	90.75	93.45
	2.5-ac	228	70.77	71.70	95.49	97.52
3	Current	10	74.76	75.00	84.60	84.81
	160-ac	3	74.71	74.96	84.36	84.58
	40-ac	12	74.74	74.98	86.94	87.26
	10-ac	54	75.44	75.70	92.94	93.18
	2.5-ac	228	76.01	76.27	97.65	97.86
4	Current	10	77.70	78.09	86.40	87.44
	160-ac	3	77.68	78.08	82.93	86.91
	40-ac	12	77.70	78.10	87.35	90.12
	10-ac	54	78.11	78.46	94.94	96.19
	2.5-ac	228	78.31	78.52	97.25	97.90
5	Current	10	72.00	73.75	81.21	84.16
	160-ac	3	72.00	73.75	78.65	81.34
	40-ac	12	72.12	73.76	78.50	83.92
	10-ac	54	72.36	74.57	89.68	93.64
	2.5-ac	228	75.21	75.75	95.38	97.50
6	Current	10	15.22	22.33	33.46	61.42
	160-ac	3	2.22	3.12	5.97	41.99
	40-ac	12	22.69	34.26	45.87	80.38
	10-ac	54	35.74	40.27	88.06	87.97
	2.5-ac	228	40.97	42.75	87.79	96.17

Table D3. Well-based static connectivity by zone for the crescent-shaped fluvial bar MPS model.

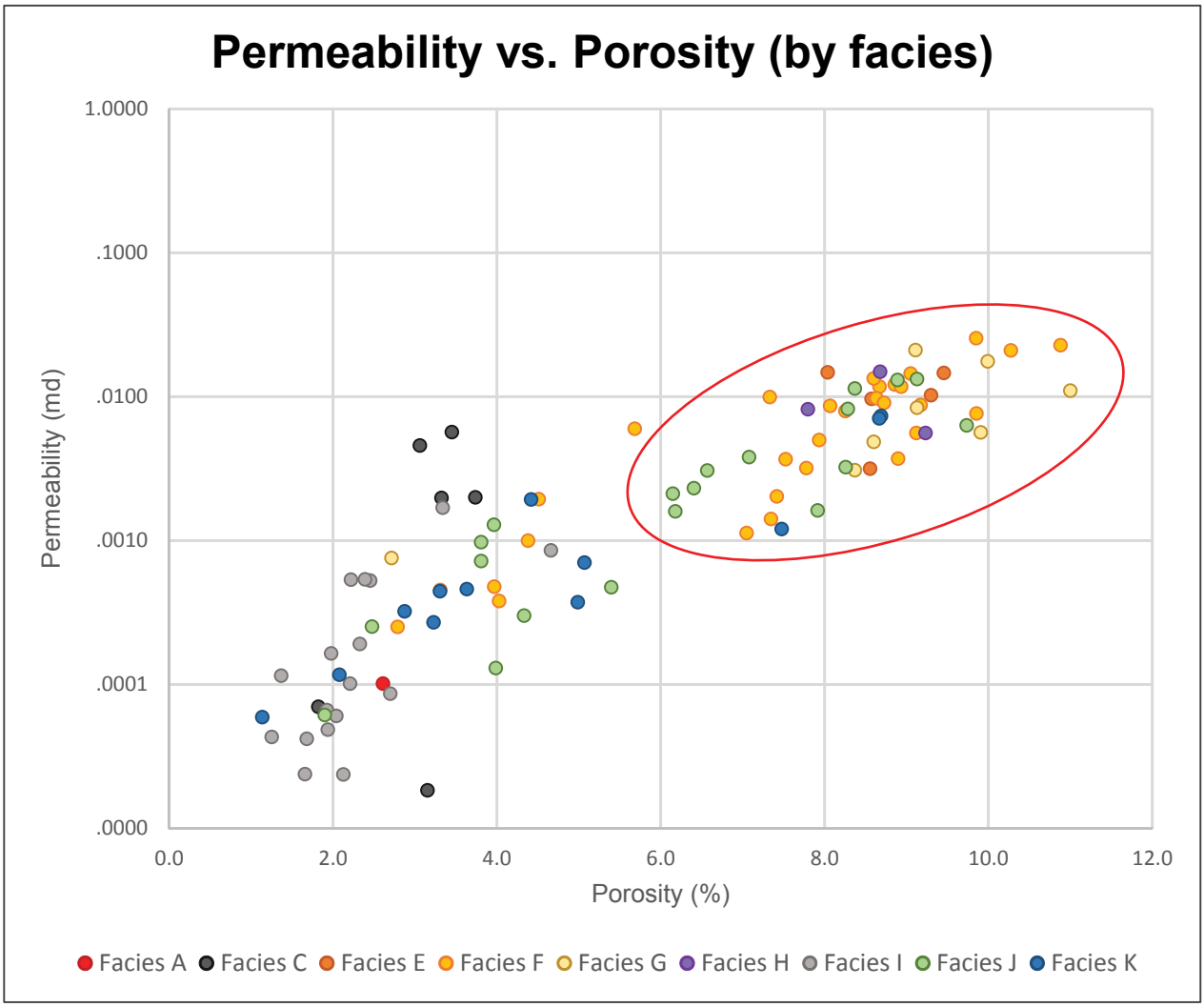

Figure D1. Confined porosity and permeability measurements from RW 12D4-25B core plugs cross-plotted by facies. Facies E, F, G, H, and J are the main facies that make up fluvial bars, which are the dominant reservoir type in Red Wash Field. Porosity-permeability values for these facies cluster above 0.001 millidarcies and 6.0% porosity, which was the basis for choosing the porosity cutoff defining "reservoir-quality" sandstone (between 6.0% and 15%). Samples that plot below 0.001 millidarcies are generally mud-rich floodplain deposits or cemented sandy facies.

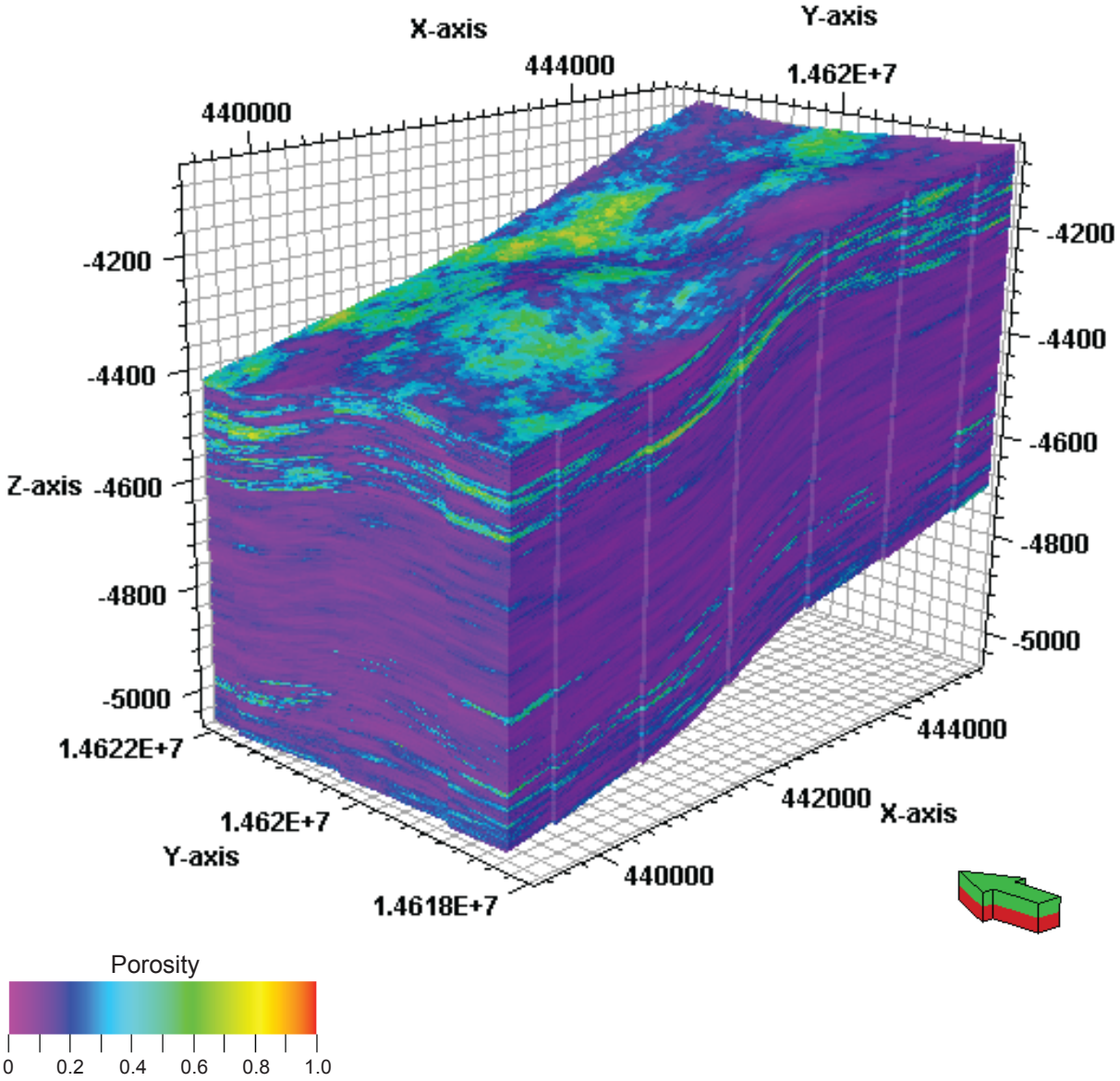

Figure D2. Total porosity (PHIT) model generated with sequential Gaussian simulation using a spherical variogram with a major direction of 2000 ft (600 m), minor direction of 2000 ft (600 m), a vertical scale of 4 ft (1.2 m), and an azimuth of 22 degrees. A porosity cutoff of 6.0% to 15% (derived from core-plug measurements) was applied to the MPS models to distinguish between connected "reservoir-quality" sandstone and total sandstone. No correction was made for coal intervals. Therefore, coal seams appear as highly porous in the model.

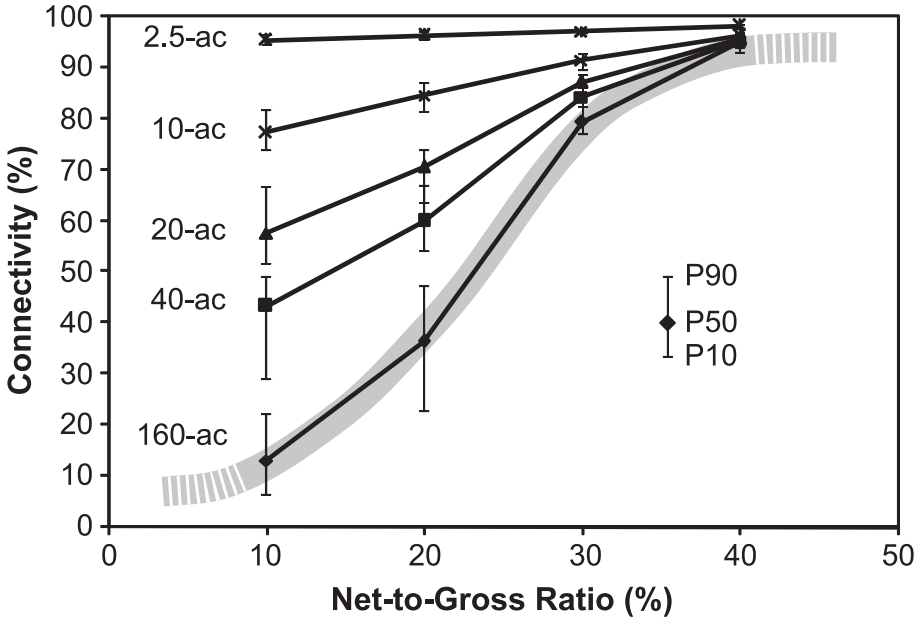

Figure D3. Plot of connectivity versus net-to-gross ratio for variable well-spacing scenarios. This graph displays the S-curve relationship between net-to-gross ratio and connectivity at low well densities. As the density increases, the relationship becomes more linear. Figure from Pranter and Sommer (2011).

Appendix E

Gamma-Ray Log Normalization: Well Groups

Appendix E contains a list of all wells in this study organized into their normalization groups. Well log normalization was done to remove systematic errors due to tool inaccuracies (Shier, 2004). Gamma-ray logs were normalized in PowerLog 3.3 (Fugro-Jason) using a two-point multi-well histogram method. Wells were organized in four groups and normalized to a reference well believed to best represent the regional geology.

Gamma-Ray Log Normalization: Well Groups								
Group	API	Well Name	Section	Township-Range	Latitude	Longitude	KB	TD
Central	**43047151530000***	**RW 23-22B**	**22**	**7S-23E**	**40.1932**	**-109.3156**	**5708**	**11180**
	43047151780000	RW 14-18B	18	7S-23E	40.2041	-109.3768	5479	11854
	43047151910000	RW 21-27B	27	7S-23E	40.1860	-109.3156	5608	11500
	43047152010000	RW 12-27B	27	7S-23E	40.1824	-109.3203	5591	11047
	43047152370000	RW 23-28B	28	7S-23E	40.1788	-109.3343	5585	11304
	43047152650000	RW 14-29B	29	7S-23E	40.1751	-109.3581	5446	11447
	43047152680000	RW 32-30B	30	7S-23E	40.1822	-109.3676	5542	11625
	43047152720000	RW 12-20B	20	7S-23E	40.1968	-109.3581	5352	11729
	43047152830000	RW 31-28B	28	7S-23E	40.1860	-109.3295	5638	11315
	43047164750000	RW 43-28B	28	7S-23E	40.1787	-109.3250	5596	11131
	43047314780000	RW 42-21B	21	7S-23E	40.1960	-109.3257	5638	11391
	43047517230000	RW 32-29B	29	7S-23E	40.1817	-109.3486	5606	11330
	43047517240000	RW 31-20B	20	7S-23E	40.1998	-109.3486	5593	11703
	43047519380000	RW 12A2-28B	28	7S-23E	40.1798	-109.3385	5616	11186
	43047522340000	RW 12B4-27B	27	7S-23E	40.1787	-109.3199	5557	11025
	43047522400000	RW 8C1-30B	30	7S-23E	40.1816	-109.3621	5581	11628
	43047151860000	RW 21-22B	22	7S-23E	40.2006	-109.3155	5412	11478
	43047152600000	RW 22-22B	22	7S-23E	40.1969	-109.3155	5409	11142
Northeast	**43047315760000***	**RW 42-23B**	**23**	**7S-23E**	**40.1968**	**-109.2871**	**5674**	**10798**
	43047151390000	RW 32-22B	22	7S-23E	40.1968	-109.3108	5720	11245
	43047151450000	RW 32-17C	17	7S-24E	40.2111	-109.2358	5713	10681
	43047151520000	RW 34-14B	14	7S-23E	40.2039	-109.2920	5745	11300
	43047151550000	RW 43-22B	22	7S-23E	40.1932	-109.3060	5650	11018
	43047151570000	RW 23-13B	13	7S-23E	40.2074	-109.2779	5802	10880
	43047151670000	RW 21-24B	24	7S-23E	40.2005	-109.2777	5702	10948
	43047151960000	RW 12-13B	13	7S-23E	40.2109	-109.2825	5516	11148
	43047152060000	RW 44-14B	14	7S-23E	40.2038	-109.2870	5789	10862
	43047152950000	RW 43-24B	24	7S-23E	40.1932	-109.2683	5625	
	43047152960000	RW 12-14B	14	7S-23E	40.2117	-109.3009	5475	11188
	43047164950000	RW 41-15B	15	7S-23E	40.2149	-109.3060	5307	11080
	43047164980000	RW 41-14B	14	7S-23E	40.2147	-109.2871	5408	10852
	43047314760000	RW 33-23B	23	7S-23E	40.1927	-109.2915	5619	10798
	43047316820000	RW 43-15B	15	7S-23E	40.2075	-109.3059	5519	11243
	43047522370000	RW 9C1-24B	24	7S-23E	40.1932	-109.2684	5631	10558

	43047522430000	RW 13B4-18C	18	7S-24E	40.2048	-109.2630	5693	10950
	43047523190000	RW 15B4-23B	23	7S-23E	40.1926	-109.2947	5684	10860
Southeast	**43047305180000***	**RW 24-26B**	**26**	**7S-23E**	**40.1749**	**-109.2966**	**5521**	**10638**
	43047151480000	RW 34-26B	26	7S-23E	40.1754	-109.2919	5559	10609
	43047151580000	RW 34-22B	22	7S-23E	40.1896	-109.3108	5604	11070
	43047151650000	RW 14-23B	23	7S-23E	40.1896	-109.3013	5583	10897
	43047152750000	RW 32-26B	26	7S-23E	40.1823	-109.2921	5553	10945
	43047152900000	RW 23-26B	26	7S-23E	40.1787	-109.2967	5521	10585
	43047305200000	RW 44-26B	26	7S-23E	40.1746	-109.2867	5584	10512
	43047305210000	RW 33-26B	26	7S-23E	40.1787	-109.2919	5547	10540
	43047310510000	RW 42-27B	27	7S-23E	40.1824	-109.3056	5566	10754
	43047310530000	RW 44-27B	27	7S-23E	40.1754	-109.3057	5483	10700
	43047336630000	KENNEDY WASH 3-1	3	8S-23E	40.1497	-109.3109	5480	10814
	43047517200000	RW 34-24B	24	7S-23E	40.1892	-109.2735	5665	10522
	43047519030000	RW 12C3-25B	25	7S-23E	40.1774	-109.2836	5624	10571
	43047519040000	RW 12D1-25B	25	7S-23E	40.1787	-109.2801	5637	10475
	43047519050000	RW 12D4-25B	25	7S-23E	40.1778	-109.2801	5634	10508
	43047522380000	RW 9C1-26B	26	7S-23E	40.1788	-109.2871	5581	10580
	43047522420000	RW 5D2-26B	26	7S-23E	40.1820	-109.3016	5545	10787
West	**43047519390000***	**RW 13D2-24A**	**24**	**7S-22E**	**40.1907**	**-109.3947**	**5441**	**11910**
	43047151760000	RW 14-23A	23	7S-22E	40.1916	-109.4139	5346	11968
	43047151660000	RW 14-24A	24	7S-22E	40.1915	-109.3951	5429	11820
	43047152050000	RW 41-27A	27	7S-22E	40.1879	-109.4190	5406	11915
	43047152300000	RW 32-28A	28	7S-22E	40.1843	-109.4426	5417	12024
	43047152360000	RW 43-29A	29	7S-22E	40.1806	-109.4567	5404	12375
	43047343840000	WV 14M-30-7-22	30	7S-22E	40.1770	-109.4854	5330	13800
	43047348370000	SU BW 6M-7-7-22	7	7S-22E	40.2278	-109.4852	5063	14250
	43047350730000	SG 6ML-11-8-22	11	8S-22E	40.1388	-109.4094	4979	11192
	43047361360000	SUBW 14M-7-7-22	7	7S-22E	40.2209	-109.4859	5114	14220
	43047363510000	RW 34-34 AD	34	7S-22E	40.1631	-109.4235	5225	17227
	43047394450000	RW 34-27ADR	27	7S-22E	40.1774	-109.4243	5450	12800
	43047403450000	GB 3D-4-8-22R	4	8S-22E	40.1570	-109.4478	5232	17311
	43047511790000	BW 15-18-7-22	18	7S-22E	40.2059	-109.4799	5165	12643
	43047519400000	RW 14D3-24A	24	7S-22E	40.1908	-109.3894	5435	11815

* = reference wells

Appendix F

Stratigraphic Zonation

Appendix F contains descriptions of each stratigraphic zone used in the MPS 3-D modeling, as well as a subsurface cross-section showing the 6 zones. Zone definitions are based on variations in net-to-gross ratio, coal occurrence, and facies changes.

Stratigraphic Zone Definitions

Zone 1 is made up of 57.6% floodplain, 30.0% fluvial bars, 5.3% crevasse splays, and 7.1% coal, with an approximate net-to-gross ratio of 35.3%. Zone 1 ranges in thickness from 142 – 188 ft (42.6 – 56.4 m). This zone is characterized as having the highest proportion of coals in the stratigraphic study interval. Due to the presence of coals, the neutron porosity (NPHI) and density porosity (DPHI) are highly variable, while the gamma-ray log displays a highly serrated character as the interval alternates between thin sandstones and coals.

Zone 2 is made up of 60.2% floodplain, 32.8% fluvial bars, 6.7% crevasse splays, and 0.3% coal, with an approximate net-to-gross ratio of 39.5%. Zone 2 ranges in thickness from 67 – 155 ft (20.1 – 46.5 m). Fluvial bars in this zone occur as blocky, isolated sandstone bodies with thick floodplain facies in between. Coals are uncommon, but can occur in association with crevasse splays.

Zone 3 is made up of 51.9% floodplain, 40.7% fluvial bars, 7.4% crevasse splays, and 0% coal, with an approximate net-to-gross ratio of 48.1%. Zone 3 ranges in thickness from 104 – 147 ft (31.2 – 44.1 m). Fluvial bars in this zone are thinner, but display complex vertical stacking patterns that result in amalgamated sandstone packages.

Zone 4 is made up of 44.7% floodplain, 47.8% fluvial bars, 7.5% crevasse splays, and 0% coal, with an approximate net-to-gross ratio of 55.3%. Zone 4 ranges in thickness from 87 – 147 ft (26.1 – 44.1 m). This zone is characterized by the highest net-to-gross ratio in the stratigraphic study interval. Fluvial bars are thick, vertically stacked, and display a blocky gamma-ray signature. Zone 4 thins toward the west.

Zone 5 is made up of 38.7% floodplain, 45.4% fluvial bars, 8.8% crevasse splays, and 7.0% coal, with an approximate net-to-gross ratio of 54.2%. Zone 5 ranges in thickness from 34 – 62 ft (10.2 – 18.6 m). The upper boundary in Zone 5 is defined by a laterally continuous coal bed that is persistent across most of the subsurface. Carbonate cemented mudstones are also present in this zone. The lower boundary is placed where the interval transitions into higher net-to-gross packages from the low net-to-gross packages below.

Zone 6 is made up of 71.3% floodplain, 15.2% fluvial bars, 12.4% crevasse splays, and 1.0% coal, with an approximate net-to-gross ratio of 27.7%. Zone 6 ranges in thickness from 62 – 114 ft (18.6 – 34.2 m). This zone is characterized by the lowest net-to-gross ratio within the stratigraphic study interval. Crevasse splays are the most common sandstone architectural element, while fluvial bars are sparse. The gamma-ray log character is serrated due to the interbedded shaley sandstones and thick mudrock successions. The lower boundary is defined by the top of the Sego Sandstone. This zone is interpreted as the brackish-water transition from estuarine and tidal-fluvial facies into the dominantly fluvial facies of Zone 5 above.

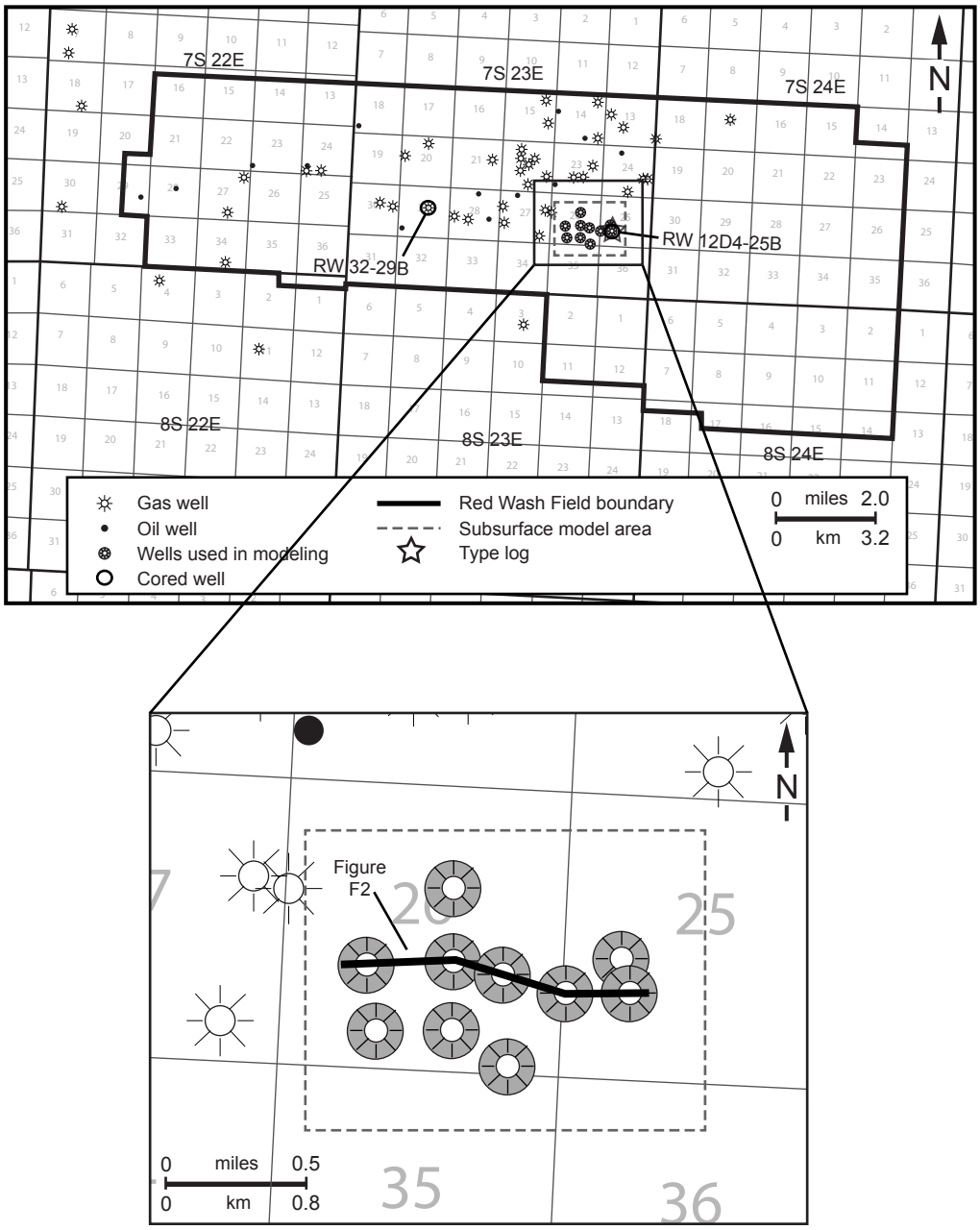

Figure F1. Base map of Red Wash Field with inset showing cross-section in Figure F2.

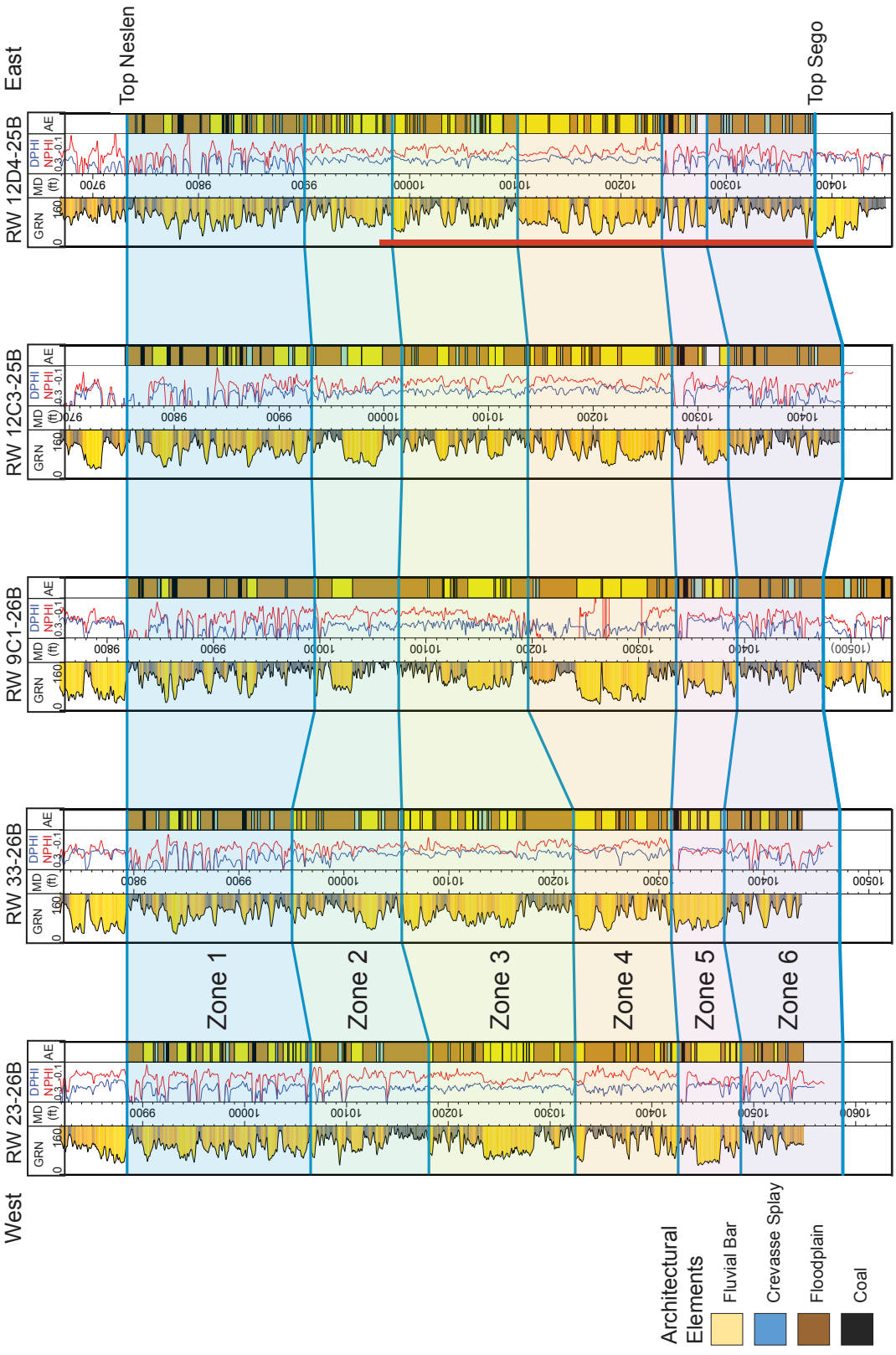

Figure F2. Cross-section of five wells in the modeling area of Red Wash Field displaying stratigraphic zonation (see location from Figure F1). The red bar in RW 12D4-25B shows the cored interval. Shown for each well is normalized gamma ray (GRN), density and neutron porosity (DPHI/NPHI), and interpretted architectural elements (AE).